

# Faults architecture and their scaling relationships: Insights into fault core thickness and fault displacement

Donald T. Seifried

Thesis for Master degree

In Structural Geology/ Petroleum Geology



Department of Earth Science

&

Centre for Integrated Petroleum Research

University of Bergen

2012

# Abstract

---

The purpose of this study is to investigate the statistical characteristics of fault core thickness and fault displacement, and to state the relationship between these two fault attributes. Field work was carried out At Tidwell Draw, in the San Rafael region of Utah, USA; and along the Moab Fault adjacent to the entrance to Arches National Park. Data from these sites were statistically analyzed, and exceedence frequency plots of fault core thickness and fault throw were drawn. These exceedence frequency plots were then redrawn on several scales, and graphical analyses were conducted to determine the frequency distribution of fault core thickness and fault throw. Following that, the data was then plotted together on a bivariate scatter plot, and analyzed for linear correlation in graphs of different scales.

The data from the Moab Fault site was augmented with data gathered from photographs. Analysis suggests that results of data gathered from photographs can produce similar results and can be an acceptable method to obtain data from difficult locations.

Results of these analyses reveal that fault throw at these locations is distributed following a power law distribution pattern, and that fault thickness tends to follow a log-normal distribution.

Analysis of a global data base involving data from selected previously published works reveal that for many data sets, exceedence frequency plots of displacement reveal that frequency distribution tends to follow log-normal trends, rather than power law trends. The similar results display log-normal distribution for fault thickness as well. Emphasis is placed on the importance of analyzing EF plot in all scales in order to form the most accurate interpretation of data distribution

Bivariate analysis of fault displacement and fault core thickness for the global data set exhibited a power law relationship with an exponent of 0,728 with a global goodness of fit regression of 74,2%. Although the data from Tidwell Draw displayed a regression of 52,0% for a power law relation with exponent value of 0,683, the data plotted consistent with the global plot. The data from the Moab Fault site also plotted consistent with the global plot. Although the Moab Fault data showed a weak regression for the power law relationship with exponent equal to 0,497, when the data was combined with another data set covering the upper ranges of the Moab Fault attributes, the combined Moab Fault data set showed a power law relationship with an exponent of 0,715 with a goodness of fit regression of 88,0%, exceeding the regression of both of the Moab Fault data sets and the global data set. This result indicates that 1) A large data set covering a broader range of displacement and fault core thickness will produce better results, and 2) data sets having most in common will produce better results when combined than data having least in common. This confirms a statement Evans, 1990 that for best results, data sets to be compared should be as similar as possible to avoid poor analysis.

# Acknowledgements

---

This Master's thesis has been conducted with the involvement of The Center for Integrated Petroleum Research (CIPR) and the Department of Earth Sciences at the University of Bergen. As part of the IMPACT project, the research that went into this thesis was funded with the help of STATOIL and the Research Council of Norway, CLIMIT Program.

I'd like to express my sincere gratitude to my supervisor, Anita Torabi, for her patience and guidance during the time that I worked on this project. Anita's support, both professional and personal, helped motivate me during a very difficult period. I would also like to thank my co-supervisor, Alvar Braathen, for his contributions, and for his company during those long trips in Finnmark.

I would also like to thank Haakon Fossen for sharing his photographs with me. I would like to thank Wojtek Nemeč for his patience and time it took to explain many questions I had about statistics. I would also like to thank Walter Wheeler for giving advice and direction in writing the thesis, and for volunteering to send me some articles. I would like to thank Eivind Bastesen for his input on fault architecture and for sharing some of his data with me.

I'd like to thank Dmytriy Kolyukhin for his help with analyzing the data from ANP utilizing the Bayesian Information Criterion.

I am deeply indebted to Katrine Olsen Grindhaug for her support as my field assistant in May, 2011. Her knowledge, skill and initiative kept this research from ruin on several occasions. Although my camera failed me, Katrine's photographs contributed to several figures I might have otherwise done without. I would especially like to thank her for her role as confidant when I really needed to talk things out.

I would also like to give thanks to Karen Cecilie Johannessen, Svein Martin Hatleseth, Eivind Susort, Espen and Jenny Eidsvåg, and Kari Sekkingstad for their support and contributions, under way.

I would like to thank my wife, Sølvi Seifried, for her patience, hard work, and for putting up with me these last six years that have led to this thesis. She has worked as hard as I have, maybe harder.

This thesis is dedicated to Sofie, Arnie, and Michael. They are the reasons for my making it this far.

Donald T. Seifried  
Bergen, 1. October 2012

# Table of contents

---

<b>1. Introduction</b>	<b>1</b>
1.1 Aim of this assignment	1
1.2. Definitions and explanations	1
1.2.1 The damage zone	1
1.2.2 The fault core	2
1.2.3. Displacement, offset, throw, slip (D)	6
1.2.4. Deformation Bands	7
1.3. State of the art	8
1.3.1 Displacement versus thickness: $T=yD^n$	8
1.3.2 Distributions of fault core thickness and fault displacement	9
1.4. Methods used	10
1.4.1. Field data gathering	10
1.4.2. Bias related to measurements	10
1.4.3. Statistical treatment of data	14
<b>2. Geological setting</b>	<b>21</b>
2.1. The Colorado Plateau and the Paradox Basin	21
2.1.1 The Moab Fault	23
2.1.2 San Rafael Swell	28
<b>3. Results</b>	<b>31</b>
3.1 Moab fault at Arches National Park entrance (ANP)	31
3.1.1 Structural characteristics at ANP	31
3.1.2. Results of statistical analysis from ANP	32
3.2. San Rafael Swell at Tidwell Draw	41
3.2.1. Structural Characteristics at Tidwell Draw	41
3.2.2. Results of statistical analysis of Tidwell Draw data	42
3.3. Combined results for thickness to throw relationships	45
<b>4. Discussion</b>	<b>47</b>
4.1. Interpretation of the results	47
4.2. Comparison with previously published results	48
4.2.1. Univariate statistics	48
4.2.2. Fault core thickness versus fault displacement	57
4.2.3. Comparison of ANP results with Foxford et al., 1998	60
4.3. Implications for fault architecture	61
<b>5. Conclusion and further research</b>	<b>63</b>
5.1. Conclusion	63
5.2. Further research	64
<b>References</b>	<b>66</b>
Appendix 1: Readings from the scan line at ANP	71
Appendix 2: Readings from scan lines at Tidwell Draw.	75
Appendix 3: Fault data from the Moab Fault scan line at ANP.	77
Appendix 4: Thickness and displacement data from Moab Fault, including photo estimations.	78
Appendix 5: Data for displacement and thickness of faults observed at Tidwell Draw.	79



# List of figures

---

1-1	Asymmetry of the damage zone	2
1-2	Components of a typical fault system	3
1-3	Damage zone components of major faults in siliciclastic rock	5
1-4	Strike separation and dip separation	7
1-5	Image of the road cut south of Arches National Park (ANP)	10
1-6	Devices for precision measuring of fault thickness	11
1-7	Plots comparing data collected in the field to data gathered from photographs	12
1-8	Mean and standard deviation	14
1-9	EF plot diagnostic chart	17
2-1	Maps of the area	22
2-2	The outcrop of the Moab Fault as viewed from Arches National Park Visitors Center.	24
2-3	The stratigraphy of the Honaker Trail Formation at the Moab Fault site	26
2-4	Lithostratigraphic column of the outcrop studied at Tidwell Draw	28
2-5	The outcrop that was studied at Tidwell Draw in San Rafael Swell	30
3-1	Moab Fault fractures (red) and faults (blue)	31
3-2	Fault core thickness fluctuates	32
3-3	EF plots for the Moab Fault fault throw (A-F) and thickness (G-L) scan line observations	36
3-4	EF plots of the data at ANP, which includes photographic estimations	38
3-5	Plots of thickness versus displacement for the faults at ANP	39
3-6	The Bayesian Information Criterion	40
3-7	The Schmidt Net and Rose diagram for Tidwell Draw faults and fractures	41
3-8	EF plots for throw (A-F) and EF plots for core thickness (G-L) for the Tidwell Draw area	43
3-9	The plot of thickness to throw for faults at Tidwell Draw in San Rafael Swell.	46
3-10	A plot of the data combined from the site at ANP and the site at Tidwell Draw	46
4-1	Top- Log displacement, log EF plot of faults from previously published articles	50
4-2	Probability scale EF/ log scale displacement plot for published data.	51
4-3	EF plot of thickness for selected published data	52
4-4	log scale EF to linear scale fault core thickness for some of the previously published data.	54
4-5	Probability scale EF to log thickness values for published fault core thickness data	56
4-6	Plot of fault core thickness to fault displacement for selected previously published articles	58
4-7	Comparison of studied results to published results	59
4-8	Combined Foxford et al., 1998 and ANP observations, 2011	60

# 1. Introduction

---

## 1.1 Aim of this assignment

The aim of this study is to take fault displacement measurements and corresponding fault core thickness measurements and determine through statistical analysis, if any relationship exists between the thickness of the fault core and the displacement of faults in siliciclastic rocks in extensional settings. Additionally, the frequency distribution of these parameters will be examined by comparing the results of this study with some of the previously published data, to develop a better understanding of the distribution of these attributes. A critical examination of the concept of power law distribution in these fault attributes is offered for consideration.

The thickness-displacement relationship of faults in the study areas, as a part of the description of the fault architecture, may be compared with the thicknesses and displacements of similar faults elsewhere. The information gained may increase our understanding of fault behavior, and perhaps lead to a better understanding of the factors that affect the relationship between thickness and displacement. This understanding may be applied to similar faults elsewhere (Shipton et al., 2006, Wibberley et al., 2008). Understanding the relationship between fault core thickness and displacement could aid in optimum population of faults in reservoir models, and better reservoir characterization and well-planning. Furthermore an understanding of the relationship and distribution patterns of fault core thicknesses and displacements may provide fundamental knowledge on fault architecture underground, which would benefit the CO<sub>2</sub> sequestration management when choosing the best candidate reservoirs to safely store CO<sub>2</sub> underground. This study is part of an umbrella project called Impact, being carried out by the Centre for Integrated Petroleum Research (Uni-CIPR), to increase our knowledge and understanding of CO<sub>2</sub> injection and storage in reservoir rocks under the earth's surface.

The field work for this project took place in May 2011 at two locations within the Colorado Plateau; The Moab Fault at the entrance to Arches National Park (ANP), Moab, in southeastern Utah, USA; and at Tidwell Draw within the San Rafael Swell, 20 kilometers east of Green River, in central Utah, USA.

## 1.2. Definitions and explanations

### 1.2.1 The damage zone

The damage zone is the volume of rock surrounding the fault core (Figure 1-2). The damage may contain ductile smearing structures, fractures, minor faults, and physically and chemically altered rock (e.g. Wibberley et al., 2008, Caine et al., 1996). The damage zone is determined by the structures that formed as a result of the faulting process. The fault related structures tend to be

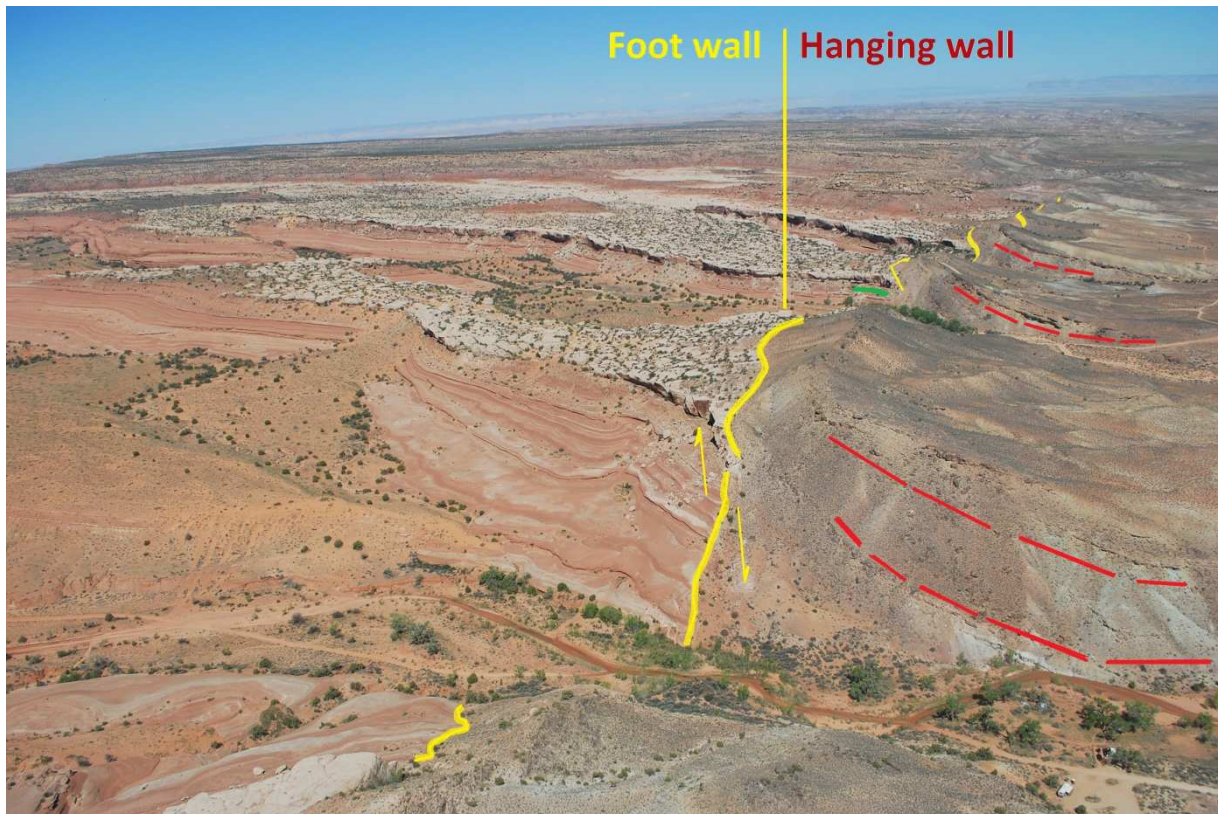


**Figure 1-1: Asymmetry of the damage zone** can be seen in this image. The footwall (left side of fault) has a relatively narrow damage zone (approximately 50 meters), which can be determined by measuring the density of deformation bands. The hanging wall damage zone forms a ductile drag fold (see red dashed lines) and extends several hundred meters to the right. Note the camper in the parking lot at the lower right corner for scale. *Photograph of Bartlett Fault by Haakon Fossen, 2011. Used by permission.*

most densely located nearest the fault core, and the density of these structures diminishes outward from the fault core (Berg & Skar, 2005). The damage zone extends outward from the fault core to a point where structure density approximately equals background density (Agosta & Aydin, 2006, Torabi & Berg, 2011). Damage zone distribution around a fault is often asymmetrical. At the Moab Fault, the hanging-wall damage zone tends to be much larger than the footwall damage zone (Berg & Skar, 2005) and shows extensive fault drag (Figure 1-1).

### 1.2.2 The fault core

The fault core (Shipton et al, 2006; Torabi and Berg, 2011; Agosta, F., & Aydin, A., 2006; Bastesen et al., (in print); Braathen et al., 2009; Childs et al., 2008) is the portion of rock affected by a fault that accommodates most of the displacement of the fault. As a result, the fault core contains fault rock that is deformed and generally does not contain the original fabric of the host rock. Some material that is found within the fault core includes fault gouge, cataclasites, breccia, clay smear and

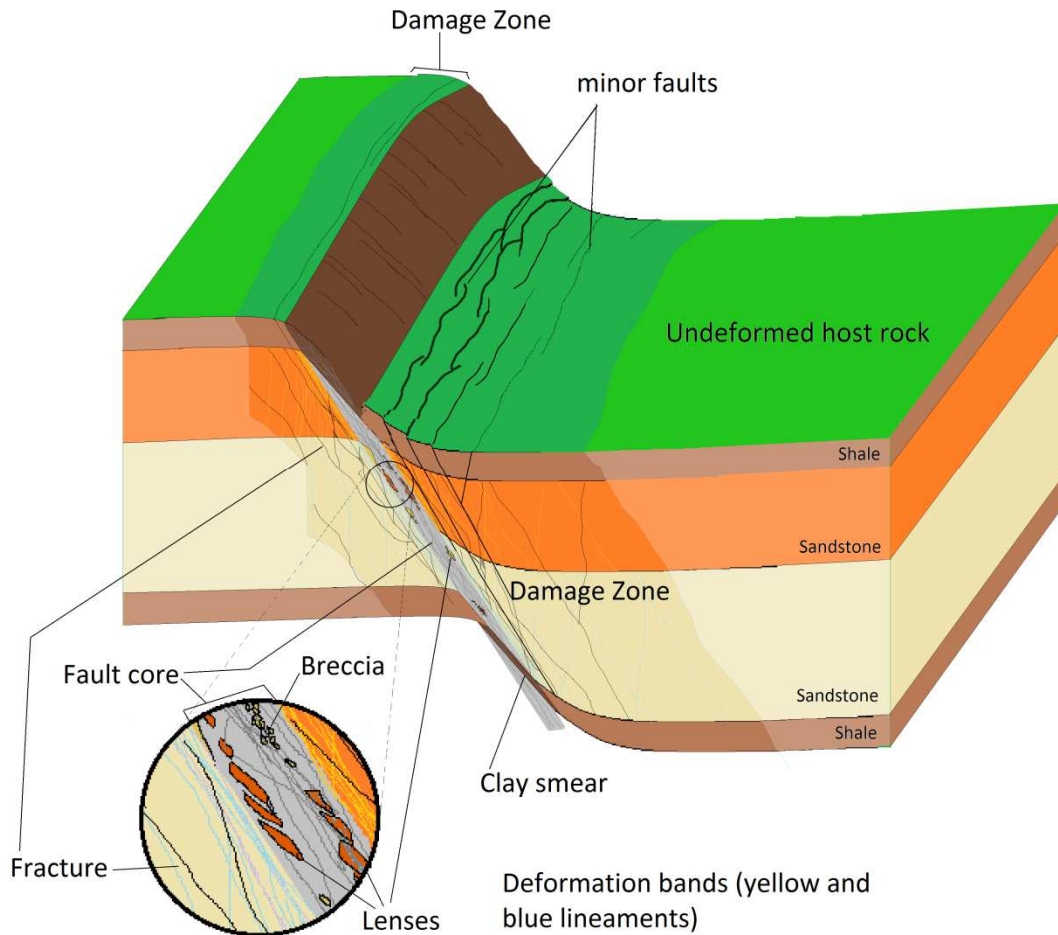


**Figure 1-2: Components of a typical fault system.** Note how damage intensity and structure density increases toward the fault core (gray lineament in the center). The inset represents a closer view of the fault core, showing how various components may look. The blue lines in the white sandstone represent deformation bands, as do the yellow lines drawn into the orange sandstone. Gray lines in the core have no specific meaning except to show possible cracks and drag within the core. Definitions and component descriptions are in the text.

lenses (e.g. Bastesen et al., 2012; Childs et al., 2008), Figure 1-2. These are collectively referred to as fault rock and acquire their texture and altered state at least in part because of shearing processes of the fault (Sibson, 1977, Peacock et al., 2000). Fault gouge is the clay rich fine grained substance formed from total comminution of shaley sandstone entrained into the fault (Fredman et al., 2008). Cataclasite is generally the product of purer sandstone faults in which most of the grains are crushed relative to the original sandstone host rock. The crushed grains create smaller pore spaces and pore throats than those found in the original sandstone, reducing permeability (Figure 1-3D). Clay smear is material entrained into the fault from shaley layers (Figure 1-3 B). The membrane formed by a clay smear can create a barrier to cross fault fluid flow for a displacement that is as much as four times the thickness of the shale layer (SSF=4) (Færseth et al., 2007). Breccia consists of clasts of rock fragments (Figure 1-3C). There is no set definition to determine the upper size limit of breccia clasts (Childs et al., 2009). However, lenses, lozenge shaped masses of wall rock may preserve the fabric within the fault core to varying degrees (Foxford et al., 1998).



Lenses are an example of the type of rock that can be found within the fault core. If lenses are detached from the wall rock (Bastesen et al., 2012 (in print); Wiberley et al., 2008) and enclosed in fault rock material such as fault gouge (Wibberley et al., 2008; Foxford et al., 1998), then they are included in the thickness measurements of this research project. While the mechanical and chemical properties of a lens may be intact or modified from the original host rock (Torabi and Berg, 2011; Foxford et al., 1998) the lens may also undergo deformation and chemical alteration such that it doesn't resemble the host rock (Wibberley et al., 2008).

Fault rock tends to present a barrier to fluid flow across the fault due to reduced pore space and lowered permeability values than the surrounding host damage zone or host rock (Wibberley et al., 2008; Færseth et al., 2007).

It is important to define the element that is being measured. Fault thickness measurements are often misleading because the thickness being measured is not clearly defined (Torabi & Berg, 2011; Childs et al., 2009). Shipton et al. (2006) emphasized the importance of defining clearly what to be measured in order to remove questions or doubt regarding thickness measurements. There are several definitions involving the thickness component characteristic of fault cores. These will be discussed here.

*Fault core thickness* (T) is the thickness of the fault rock found within the fault core. There is considerable discussion about the value of the fault core thickness in scaling relations. There is currently no definition of the boundaries of the fault core that is acceptable to all, and measurements have been subjective (Torabi and Berg, 2011; Shipton et al., 2006; Childs et al., 2009; Evans, 1990). The boundary is ambiguous and not all elements that define the fault core are found in all faults. Furthermore, at any point along a fault, the thickness can vary by a full order of magnitude (Shipton et al., 2006). Further confusing the issue is that there is an inconsistent use of terminology. What some authors describe as the fault core (e.g. Bastesen et al., 2012 (in print); Shipton et al., 2006; Caine et al., 1996; Davatzes & Aydin, 2005; among others), other authors (e.g. Wibberley et al., 2008; Foxford et al., 1998) call the fault zone. This term is confusing since several articles refer to the fault zone as containing both, a fault core and a damage zone (e.g. Agosta & Aydin, 2006; Caine et al., 1996; Bastesen et al., (in print)). "Core zone" (Rawlings et al., 2001), "fault width" and "fault thickness" (Peacock et al., 2000) are other terms synonymous with fault core thickness.

*Fault thickness* is defined in Peacock et al., 2000 as "the extent of deformation and grain size reduction in a fault zone, usually measured perpendicular to the fault." A similar but slightly different term from the same source is *gouge thickness*, which is the measure of the thickness of the comminuted material between slip surfaces (Byerlee & Summers, 1976; Peacock et al., 2000). For this project, the definition of gouge thickness has been modified to include the thickness of lenses found between slip surfaces. This definition was used in the field.

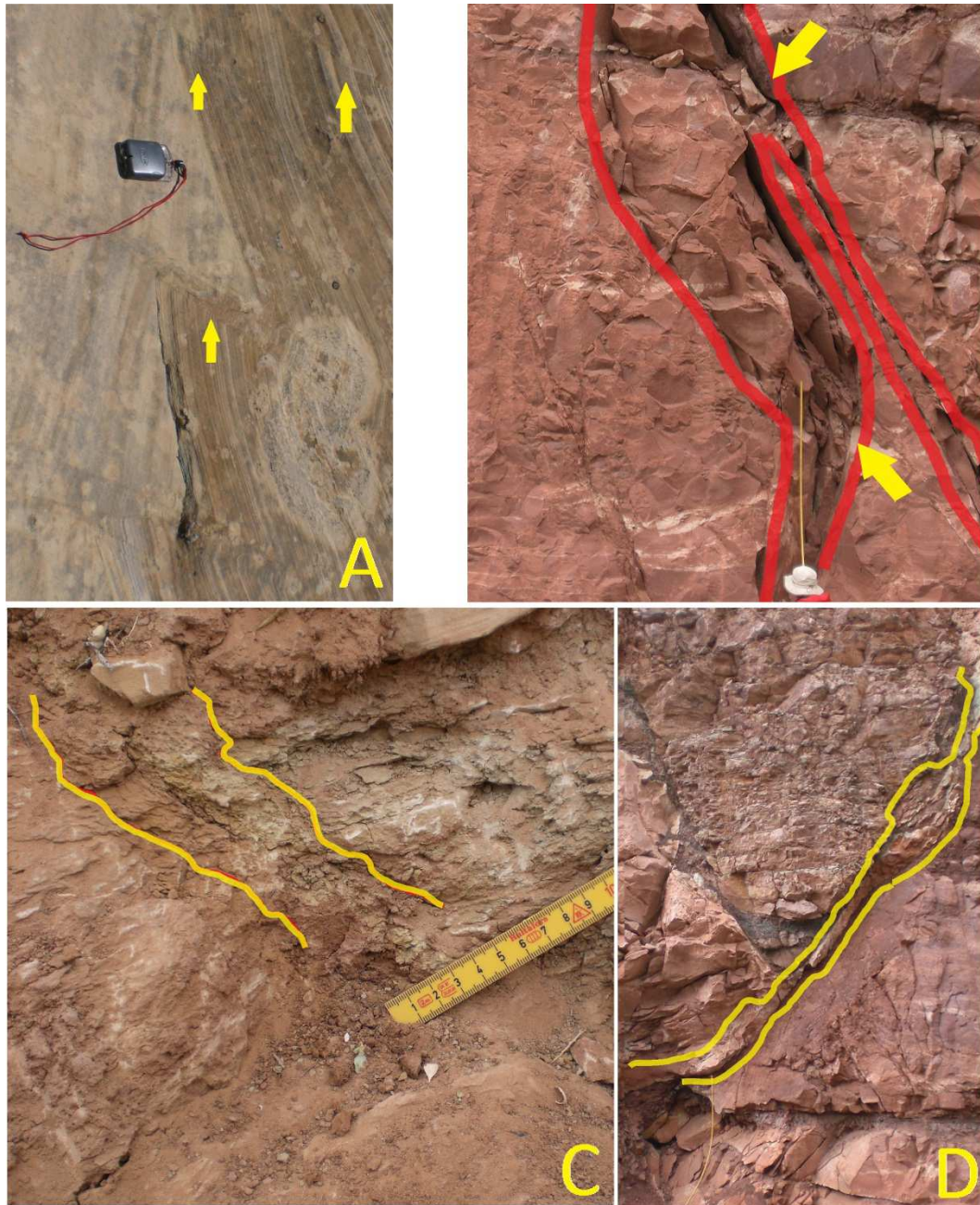


**Figure 1-3: Damage zone components of major faults in siliciclastic rock.** A) Deformation bands- these are cataclastic bands in the Navajo Formation, San Rafael Swell. B) Arrows point to breccia that formed where two faults meet. Note that the width of the fault increases dramatically where two faults intersect- Arches National Park. C) Clay smearing in a fault core through shale, San Rafael Swell. The fault core is approximately 4cm across, bounded in the image by yellow lineament. D) Image of a fault core that is filled with cataclasite. Thickness varies between 8 and 12 cm. Note the 2m long meter stick in the lower left corner for scale. *All photographs were taken by Katrine Olsen Grindhaug.*

Faults in this project are minor faults located in the damage zone of major faults. No distinction was made between principle fault slip surfaces and other slip surfaces. The approach in this project is to define all discontinuity surfaces showing separation and displacement on either side relative to the other as a general fault. The two discontinuity surfaces were considered to be one slip surface pair with no other detectable slip surface within or between the discontinuity surfaces. Gouge thickness as defined by Peacock et al., 2000, modified to include the thickness of any lens was

used as the definition of the thickness to be measured for each of the faults encountered along the scan line, each fault having only one pair of slip surfaces.

### 1.2.3 Displacement, offset, throw, slip (D)

Displacement has several synonymous definitions and terms. As a general rule, displacement is a vector which points from one point along one of the slip surfaces to the point on the opposite slip surface that was positioned adjacent to the first point prior to faulting (Van der Pluum & Marshak, 2004; Peacock et al., 2000; Fossen, 2010). The direction of the vector describes the direction of relative movement of one side of the fault with regard to the other, while the magnitude of the vector gives the total distance of offset between the two walls. The displacement can be further divided into strike separation, the horizontal displacement as measured along the strike of the fault, and dip separation, as measured along the dip direction of the fault. The dip separation can be broken down into a horizontal component, or heave, which is the horizontal distance normal to the fault strike, and the vertical component, also called throw (see Figure 1-4). Offset is the apparent displacement of a common marker, such as a layer or a horizon (Peacock, 2000). In a purely dip-slip extensional fault, offset will equal the dip separation. Stratigraphic throw is the height of the section of the stratigraphic column that separates two stratigraphic markers (beds, boundaries) that are brought together by the fault (Davis and Reynolds, 1996).

For many of the faults observed, true displacement as measured by the magnitude of displacement along a displacement vector could not be established. To establish the true displacement, markers such as veins or distinctive boulders/ fossils need to be present and visible on both, the footwall and the hanging wall. Barring that, slickensides or slickenlines must be present to establish direction of slip. Because extensional faults were studied in this project, the faults with horizontal slickensides were noted, but not included with the data for displacement and thickness measurements for analysis. It wasn't possible to measure how far into the rock displacement took place for these faults. In this project, measured thicknesses have been compared with the throw of each fault.

Because the outcrop at Arches National Park approaches a cliff, and because photographs are two dimensional representations, vertical offset (throw) was measured between beds. Vertical observations give distinct points of reference that are observable and verifiable. Displacement was not measured along the fault trace because it is uncertain and unlikely that the faults followed this path of displacement. Often, displacement, offset and throw are synonymous, even though each term has its own technical meaning. In this study, these terms are used interchangeably.

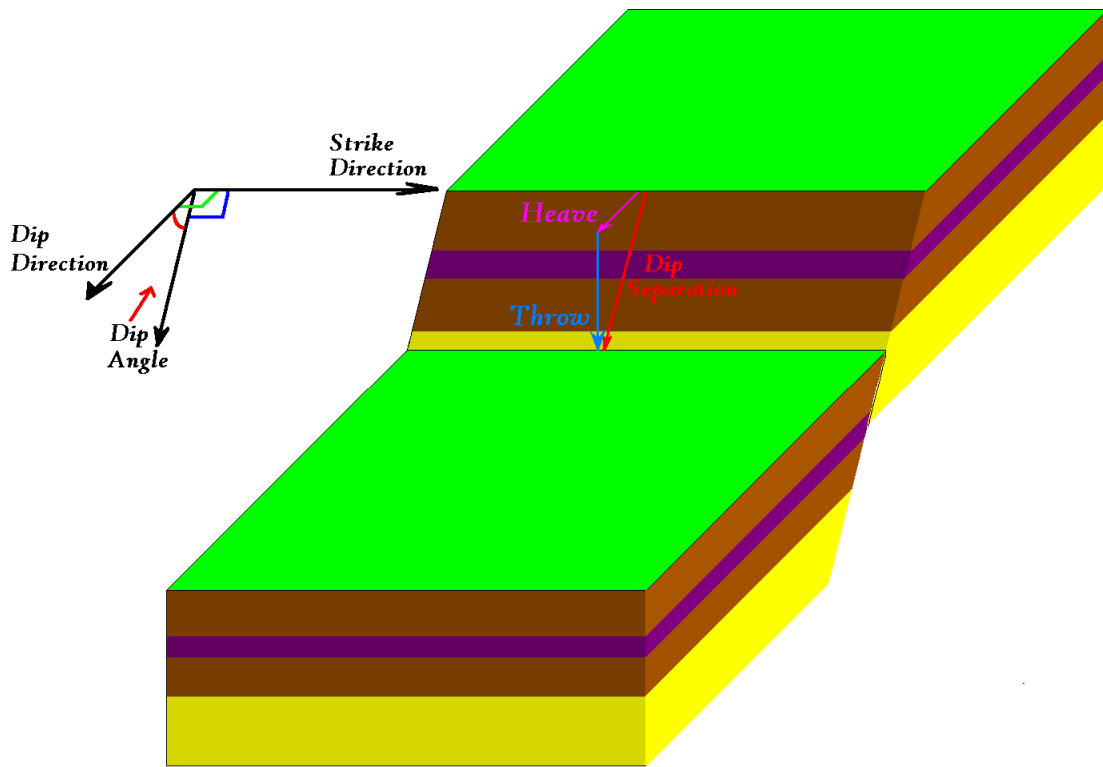


**Figure 1-4: Strike separation and dip separation.** For a dip slip fault, such as the normal fault seen above, the dip separation is also the net displacement. Heave is the horizontal component and throw is the vertical component of dip separation. No strike separation is viewed in this example because strike separation is found in strike slip faults and oblique faults.

Slip has also been used to describe displacement, however, slip is generally used to describe one seismic event (e.g. Shipton et al., 2006; Ferrill et al., 2008), whereas displacement refers to the total fault history or a specific interval.

#### 1.2.4 Deformation Bands

Deformation bands have been observed at the outcrop at Arches National Park (ANP). A deformation band is a discontinuity structure that shows displacement in the range of some millimeters to several centimeters (Figure 1-3A). They form in pure sandstones with high porosity and can also be observed in sandstones containing some clay. Deformation bands in the outcrop at ANP tend to appear isolated or occasionally running parallel to one another and spaced 10 cm apart in groups of two to four bands. Literature describes deformation bands as forming in clusters in porous sandstones, often parallel to and straddling slip surfaces (Shipton et al., 2005; Fossen et al., 2007). While deformation band clusters were observed at other outcrops in the Colorado Plateau (e.g. Cache Valley, Bartlett Fault, and Courthouse Rock, among others), this type of dense clustering was not observed at the outcrop at ANP.

Deformation bands display discontinuity across them similar to faults and have been classified as faults or fractures in some of the literature (e.g. Berg & Skar, 2005; Aydin & Johnson, 1983; Sorkhobi & Hasagawa, 2005). Unlike ordinary fractures, opposite sides of a deformation band do not lose cohesion. Permeability of sandstone is reduced within most deformation bands, contrary to fractures. Furthermore, deformation bands tend to exhibit strength hardening, as opposed to



fractures (Fossen et al, 2007; Aydin & Johnson, 1983). For these reasons, deformation bands were not regarded or analyzed as faults in this project.

### 1.3 State-of-the-art

The study of scaling relationships between the various fault attributes (displacement, fault length, fault width, fault height, and fault core thickness) have been discussed for several decades. For instance, the article by Cowie and Scholz (1992) asserted a unity power law relationship between maximum displacement and fault length, which was statistically verified by the research of Clark & Cox (1996). The relationship between fault height (the length of a faulted surface when measured in a direction parallel to the dip of the fault plane) and maximum displacement was investigated by Gross et al., (1997). The finding of their research was that in a solid medium, a unity power law relationship existed between displacement and fault height. However, in interbedded lithostratigraphic layers with starkly contrasting competencies, Gross et al., (1997) found that height was independent of displacement, implying that the competency of a bed affects the behavior of fault propagation.

#### 1.3.1 Displacement versus thickness: $T=yD^n$

As faults propagate, host rock is deformed, creating damage zones in the vicinity of faults. Each wall block will have a damage zone, which contains progressively more complex structures as the fault evolves (Wibberley et al., 2008; Bastesen et al., in press). Damage zone widths increase with continued fault growth (Wibberley et al. 2008).

Positive correlation of D/T has also been observed (Shipton et al., 2006), although thickness can vary within a fault, both along strike and dip, by several orders of magnitude (Evans, 1990; Foxford et al., 1998; Childs et al., 2009). Correlation of fault core thickness to displacement can give ambiguous, subjective results because it is often difficult to distinguish the fault core boundaries (Childs et al., 2009; Torabi & Berg, 2011). Some studies have not distinguished between fault core and damage zone thickness or have not been consistent in their definitions (Torabi & Berg, 2011).

Evans (1990) observed that there is at least two orders of magnitude of scatter along a log-log scale of displacement to thickness. On linear plots, the scatter was so great that no useful statistical relationship between fault core thickness and displacement could be established. Knott et al., 1996 observed that for some outcrops, fault core thickness and fault displacement exhibited a power-law relationship ( $T=yD^b$ ), and suggested that this relationship may be the effect of layer thicknesses and siliciclastic grain sizes. Sperrevik et al, (2002) showed that the lithology of the footwall and the hanging wall affect the thickness of the fault. Their research demonstrated for a given value of displacement, sandstone juxtaposed against sandstone will give a greater thickness than sandstone juxtaposed against shale. This finding confirmed the report by Knott et al, (1996),

that lithology affects the displacement to thickness ratio. [Shipton et al, 2006](#) found a weak positive correlation over seven orders of magnitude of displacement, but pointed out that there was over three orders of magnitude of thickness scatter for any one value of displacement. Their report suggested that there may not be a significant correlation between fault core thickness and displacement. [Shipton et al., 2006](#) also stressed the need to define thickness as it applies to fault attribute studies, pointing out that damage zone width and fault core thickness were two different attributes. [Bastesen et al., \(in print\)](#) suggests that there is no linear correlation between displacement and thickness, but that the trend of thickness with increased displacement follows a power law relationship ([Torabi & Berg, 2011, Shipton et al., 2006](#)); with the exponent (n) equal to 0,5. [Torabi and Berg \(2011\)](#) suggest that over the evolution of a fault, several different scales may apply. At the scale below 1m displacement faults grow as isolated entities. As faults grow beyond this range, their growth influences the stress field of nearby faults, thereby creating the tendency of faults to form links with nearby faults. The linkage of faults with one-another reduces the rate of faults thickening for a given increase in displacement. However, [Torabi & Berg \(2011\)](#) suggested that further research needs to be performed to verify this change in the behaviour of fault growth during fault link-ups.

Using a statistical approach called the Bayesian Information Criterion (BIC), [Kolyukhin & Torabi \(2012\)](#) have analyzed fault core thicknesses, damage zone widths, and fault lengths versus displacement for many data sets (listed in table 1 in [Kolyuchin & Torabi, \(2012\)](#)). The statistical analysis provided them with evidence that the T/D relationships are scale dependent, and that one power law equation is not adequate to treat the entire range of displacements. The article suggested a changing point between scales at approximately 10 centimeters displacement, at which point the T/D value increases in slope (i.e. increases in power law exponent value).

Currently discussion continues as to whether the relationship between fault core thickness and displacement is linear ([Foxford et al., 1998; Childs et al., 2009; Wibberley et al., 2008; Sperrevik et al., 2002](#)), follows a power law relationship ([Kolykhyun & Torabi, 2012; Knott et al., 1996; Bastesen et al., \(in print\)](#)) and what the exponent of that relationship may be, or whether there is any correlation whatsoever between fault core thickness and displacement ([Shipton et al., 2006; Zee et al., 2008; Evans, 1990](#)).

### **1.3.2 Distributions of fault core thickness and fault displacement**

There tends to be a consensus that frequency distribution of fault displacement tends to follow a power law model ([Ackermann et al., 2001; Soliva & Schultz, 2008; Torabi & Berg, 2011](#)). However, an argument can be made for a log-normal frequency distribution, based on graphical evidence from EF plots in this study. This paper will describe possible thickness frequency

distribution patterns. Because no other paper was found to give commentary directly dealing with frequency distribution of fault core thickness, it is suggested that this thesis may be the first to explicitly describe the frequency distribution of fault core thicknesses.

## 1.4 Methods used

### 1.4.1 Field data gathering

A scan line across the base of the outcrop was utilized at Arches National Park ( ANP) entrance. Two workers moved down the scan line. One worker took measurements and reported them to the second person, who recorded the data in a log. The data recorded was orientation of fractures, deformation bands and faults. In addition to strike and dip data, fault displacement and thickness measurements were carried out along the scan line. The scan line was conducted from the tip of an outcrop and along the wall for 200 meters, with data recorded in the sequence it was received along the scan line. This data can be found in Appendix 1, in the appendix. The scan line data for Tidwell Draw can be found in Appendix 2, in the appendix.

Photographs were taken along the scan line at ANP and were used to verify measurements. Using Adobe Illustrator illustration editing tool, these photographs were merged together to make a composite illustration of the outcrop at ANP where the scan line was taken (Figure 1-5).

### 1.4.2 Bias related to measurements

Thicknesses of faults can vary along the fault by a full order of magnitude within a 10 meter stretch (Foxford, 1998), therefore it was important to obtain reliable measurements. Because the



**Figure 1-5** Image of the road cut south of Arches National Park (ANP) along highway 163 in southeastern Utah. The image is viewed from the north. The red lines indicate small faults in the hanging wall damage zone of Moab Fault, (not pictured, to the left of the top image). *This image is a composite of photographs taken by Anita Torabi.*

outcrops were steep, data gathering at the outcrop was limited to the two lowermost meters of the outcrop. The device used to measure fault core thickness and displacement was a carpenter's two meter long folding ruler with a metric scale. The finest increment on the ruler is one millimeter (0,001m), therefore measurements which included any fraction of a millimeter could not reliably be made. Thickness measurements were made by placing the corner of the ruler against the side of fault that protruded furthest out and holding the ruler normal to the fault. Readings were rounded to the nearest millimeter. The smallest measurements taken were 0,001m, though there may have been faults that were thinner. More precise measurements could not be made with the ruler, leading to measurements that potentially erred by up to 50% (under 1mm), diminishing to 10% at five millimeters and 5% with measurements of 10mm. Thickness readings were not calibrated or corrected for this discrepancy, since the error can have been greater than or less than the rounded value. More precise measurements could have been made utilizing a calipers (Figure 1-6A) for thicknesses greater than 1mm, which would have improved the precision of the readings to 0,0001m (0,1mm)  $\pm$ 0,00005m (0,005mm). For thicknesses less than 0,001m, a feeler gauge (Figure1-6B) for core thicknesses could have improved precision to 0,02mm ( $2,0 \cdot 10^{-5}$ m). Feeler gauges with a tolerance of +0,005mm and -0,003mm are available.

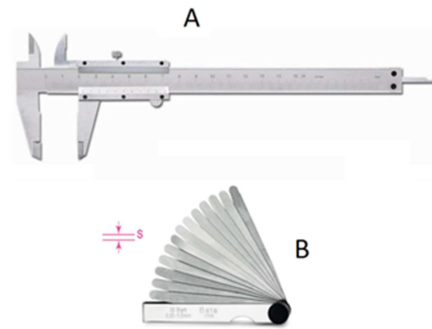


Figure 1-6: Devices for precision measuring of fault thickness. A) Calipers, B) feeler gauge

Photographs were relied upon to augment data for faults with greater than two meters throw, and for obtaining fault core throws and thicknesses in areas higher than two meters. Mapping an outcrop by photo mosaic is not an unprecedented procedure. [Agosta & Aydin, \(2006\)](#) utilized a ground photographic mosaic in their detailed description of the Venere Fault footwall, in eastern central Italy (see figure 5 in [Agosta et al., 2006](#)).

Data from field measurements are the most direct and accurate data obtained. Estimates obtained from photographs may contain errors due to measurements being indirect. Some of the causes of those errors are explained in the following paragraphs.

Electronic cameras use pixels of color to form images. For any given camera, increased distance from the outcrop increases the area a pixel covers in the photograph, with the result that resolution is reduced. A pixel from a digital photograph at 5m with wide angle lens adjustment might cover 1mm<sup>2</sup> of area. That means that anything less than 1mm in width may not be resolved

and precision measurements less than several millimeters are unlikely. If the distance is increased, the pixel covers a greater area of the image, with the result that the size of the smallest objects to be resolved also increases. Measurements of fault thicknesses less than 0,020m from photographs may be erroneous.

The best results for measuring fault dimensions are obtained from photographs parallel to the strike of the fault, with the measured dimensions as close to the center of the photograph as possible. Images near the edge of a photograph suffer from indirect angle. A three dimensional reality is converted to a two dimensional image with the result that the further from the center an object appears in any photograph, the less accurate the apparent size of the object will be in the photograph. The apparent size of objects in photographs tend to decrease outward from the center, and objects are distorted such that they appear to bend away from the center with increasing intensity towards the edges of the photograph. This problem is reduced by decreasing the angle of the field, either by zooming in or by increasing the distance between the camera and the object being photographed. Zooming in gives the best precision but reduces the field of view. Increasing the distance includes more in the photograph, but resolution is reduced, as described in the previous paragraph. Because the distance between objects and the camera are not consistent for every photograph, this problem of distortion of sizes and angles cannot be resolved, rendering measurements taken from photographs to be estimations.

Nineteen of the faults measured from out in the field were also measured from photographs for comparison and to calibrate photograph measurements (Table 1-1). The calibrated results of faults not measured in the field were added to the data set containing the field measurements, for analysis in this project. For displacement, two formulas with high best of fit values were obtained for the subset of faults that were both, measured in the field and measured from photos. The best fit is a linear curve with the formula  $y=0,727x +0,277m$ . This linear formula gave a best of fit  $R^2$  value of 0,966. Using this formula to calibrate the faults not measured in the field would result in negative values of displacement for the smallest faults and was only used for the largest fault not measured in the field. For the rest of the displacement values, a power law relation was used for displacement calibration. The formula gave a regression  $R^2$  value of 0,840 for the relationship,  $y=1,019x^{0,742}$ . Fault scaling data not obtained from the field, but estimated from photographs have calibrated using the formula:

$$D_{cal} = \sqrt[0,742]{\frac{D_{photo}}{1,019}} \quad \text{Formula 1.1}$$

where  $D_{cal}$ = the calibrated value of throw, and  $D_{photo}$  = the value of throw estimated from the photographs.

Calibration of photo estimated thicknesses was not as straight forward. Because of the small distances, accuracy of photo estimated thicknesses was not as reliable as the field measurements. However, a power law relationship ( $y=0,514x^{0,725}$ , see Figure 1-7, right diagram) had a goodness of fit regression value of 0,784. The following formula was used to calibrate photographic values of thickness:

$$T_{cal} = \sqrt[0,725]{\frac{T_{photo}}{0,514}} \quad \text{Formula 1.2}$$

where  $T_{cal}$  = the calibrated value of thicknesses from photographs and  $T_{photo}$  is the value of thickness derived directly from the photographs.

**Table 1-1:** Displacement (D) and thickness (T) measurements for the Moab set of faults that were measured both, in the field and from photographs, for comparison and calibration of faults only measured from photographs. All measurements are in meters.

Scan line position	Field D	Field T	PhotoD	PhotoT
1730	0,4	0,02	0,39	0,021
2150	0,6	0,02	0,75	0,04
4000	2	0,0525	2	0,0575
4500	0,05	0,002	0,15	0,00267
4740	0,22	0,005	0,3	0,02
5040	0,748	0,03	1,5	0,03
5040	0,434	0,003	0,26	0,005
5040	0,135	0,002	0,18	0,005
5040	0,049	0,002	0,2	0,005
5550	0,3	0,02	0,5	0,0126
6460	11,2	0,12	8,15	0,098
7230	1,5	0,03	1,5	0,035
7290	0,45	0,0025	0,34	0,02
8400	2,8	0,08	2,95	0,265
9200	1,2	0,016	1,44	0,042
9470	0,5	0,18	0,62	0,14
11000	2	0,015	2	0,036
11800	1,1	0,0625	0,32	0,04
13960	3	0,04	2,58	0,04

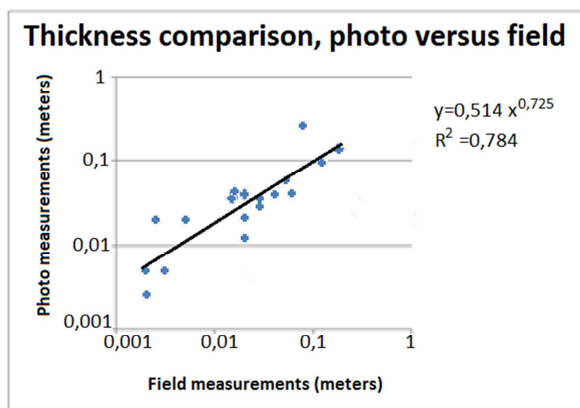
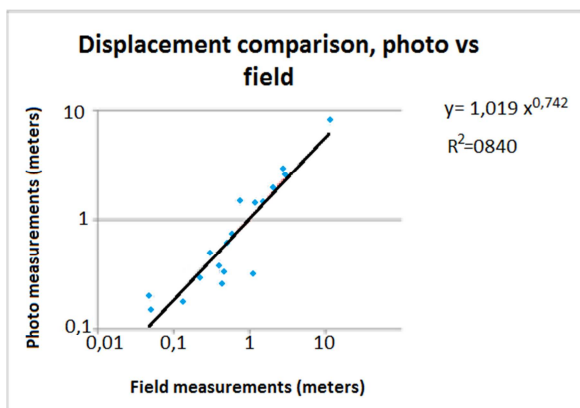


**Figure 1-7:** Plots comparing data collected in the field to data gathered from photographs for the same faults. The regression found with the relationships indicates positive correlation between data gathered in the field and data obtained from photographs.



### 1.4.3 Statistical treatment of data

#### *One variable (Univariate statistics)*

Statistics is the study of collecting, organizing, and interpreting data in a way that helps develop understanding about the relationship of a set of variables to its environment (Moore & McCabe, 2006). The distribution of data often reveals patterns in nature and the behavior of phenomena under a range of conditions represented by the data. However, data without the understanding of where the data came from, or what the data represent, are meaningless (Davis, 2002, Moore & McCabe, 2006). In univariate statistics, one variable is analyzed to determine how it is distributed (i.e. how often an attribute occurs relative to the entire population). The variable may be for example, fault displacement for a population of faults in a valley or region.

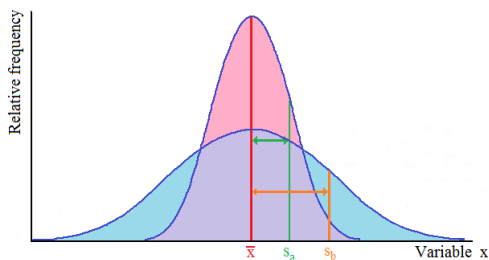


**Figure 1-8: Mean and standard deviation.** Normal distribution curves can often be described by their mean and standard deviation. Two curves representing the same amount of data are shown above. Curve A, with pink area, is narrow and has a small standard of deviation ( $s_a$ ), indicating that variable  $x$  is clustered about the mean value. Curve B, with blue area is shorter and has a higher value of the standard of deviation ( $s_b > s_a$ ), indicating a wider degree of scatter. Modified from Moore & McCabe, 2006.

population. In a sample, the sample mean ( $\bar{x}$ ) is the sum of all of the values of the variable measured in the sample divided by the number of data. Variance ( $s_x^2$ ) is a description of the amount that the data deviates from the mean. Specifically, variance is the mean value of the square of deviation from the mean, for all data in a sample. The standard deviation ( $s_x$ ) is the square root of the variance (Moore & McCabe, 2006). A low value for the standard deviation indicates that most values are clustered around the mean, whereas a large standard deviation indicates that the data is widely scattered (Davis, 2002) (See Figure 1-8).

When a sample of faults is taken, the fault data will display a distribution of values for displacement. If readings are taken randomly and cover every aspect of the outcrop or region, then the sample is said to be unbiased and a proper representation of the faults within that outcrop. Often, however, geologists are limited to the surface of the outcrop or to cores from wells, when

In order to understand how statistics works, some basic terminology needs to be explained. A datum is a numerical fact. The maximum displacement of one fault is one datum. If the maximum displacement of several faults is measured, then the collection of displacement readings is called data, and the collection itself is a data set, or a sample. An outcrop or a region will have a population of faults, the number of faults the outcrop contains. A sample contains a fraction of the population, intended to represent the entire population for statistical analysis. The mean value ( $\mu$ ) is the sum of all data values in a population, divided by the number of examples in that

sampling (Torabi & Berg, 2011, Davis, 2002). Large volumes of the interior of the outcrop may not be sampled because of the expense and impracticalities of investigating the interior of an outcrop. Wells are often drilled at specific, deliberately selected sites, and not randomly spaced. The geologist cannot take a true random sample, and must persevere with data and observations that are available (Davis, 2002).

A confidence interval ('c') is an interval into which there is a statistical probability that a random measurement from the population will fall. The probability is equal to the confidence level specified for that interval. For example, if a confidence interval of 90% for core thickness gives a value of 2,1 cm, this tells us that 90% of all faults measured in the population should fall within  $\pm 2,1$ cm from the mean value of the sample. If the confidence level is to be increased, then the interval must be widened to include the data points up to the new confidence. This increases the sample margin of error (m), the margin by which the population mean may differ from the sample mean; the accuracy of the sample mean, based on the sample variation. Reducing the margin of error necessarily reduces how confident one can realistically be that the population mean sits within the margin of error. There is one way to increase the confidence without necessarily increasing the margin of error and that is to increase the number of data in the sample population (Moore & McCabe, 2006).

$$m = z^* \frac{s}{\sqrt{n}} \quad (\text{Formula 1.3})$$

where m is the margin of error, n is the amount of data in the sample, and  $z^*$  is the amount of standard deviations from the mean value that defines the width of the margin of error.  $Z^*$  is found in table D of Moore and McCabe (2006), determined by the degrees of freedom and the desired confidence level. Although the accuracy of the confidence level and the margin of error rely heavily on the assumption of Gaussian distribution, these values may give a general idea of how many faults a sample should contain to represent the outcrop or region.

$$n_{opt} = \left( \frac{s_0 z^*}{C_\alpha} \right)^2 \quad (\text{Formula 1.4})$$

Where  $n_{opt}$  is the minimum number of samples required,  $s_0$  is the standard deviation of the preliminary population,  $\alpha$  is the limit determined by the researcher.  $C_\alpha$  is the t-value at a desired confidence for a preliminary sample population.  $t_{1/2\alpha}$  is equal to  $z^*$ , in case a source table other than Table D of Moore & McCabe, 2006 is used. With regards to faults, however, thicknesses can vary by several orders of magnitude over short distances within a single fault, rendering the concept of an optimal number of samples difficult to apply.

There are several ways to display distribution of an attribute, or characteristic. The probability-density curve is a histogram, in which the data is divided into smaller but equal sized ranges, or bins (Moore & McCabe, 2006, Davis, 2002, Clauset et al., 2007, Sornette, 2007). One



problem with histograms is determining the bin size. Bins that are too small will not have enough data to give meaning, and the curve may fluctuate too much to show a trend (Sornette, 2007). Bins that are too large will show a broad outline and poor resolution (Torabi & Berg, 2011). An additional problem with binning is that higher values in a range are represented with equal distribution frequency as with lower values in the same bin, even if there is a rapid rise, such as at an inflection point of a distribution curve, where the curve gradient is the steepest. Cumulative density plots and exceedence frequency plots can be used to avoid problems with binning. Cumulative frequency plots and exceedence frequency plots are similar, however, with exceedence frequency plots, the additional step of dividing the rank by the total number of data in the set converts the rank to a percentage, and all values can be plotted between 0 and 100%. The following formula was used to find the exceedence frequency:

$$EF_{xi} = \frac{n-n_i}{n} \quad (\text{Formula 1.5})$$

where EF is the exceedence frequency for a given value of the x axis, in this case, fault displacement, n is the total number of data used (for example, there are 54 faults at ANP; n=54), and  $n_i$  is the rank assigned to the x value (displacement or thickness) after the data was sorted. The  $EF*100\%$  gives the percent of data with a greater x value than the value ranked  $n_i$ . (see Formula 1-5).

EF plots are used as a guide to help determine whether data may be treated with parametric statistical analysis. By identifying a pattern, the EF plots also aid in choosing a distribution type. The most common types of parametric distribution types are normal distribution (also referred to as Gaussian), exponential distribution (sometimes referred to as Poissonian distribution), logarithmic distribution, and power law distribution, in which the distribution takes on a linear shape in linear x and y scales. Exponential distribution ( $f(x) = a * \exp(x)$ ) tends to be associated with data being controlled by one dimension, such as time elapsed or distance traveled. The exponential ( $b$ ) curve is only dependent upon the product of the number of samples tested and the rate of occurrences within the sample. This product is the occurrence rate and can be understood by considering an example of the concentration of a radioactive material in a sample and the frequency of the material's atomic decay. As the concentration increases, time between decays is reduced, and vice versa, giving a constant decay rate that is independent of other factors (Davis, 2002). Characteristics for exponential distribution include a straight plot of data in log-EF to X and a clearly concave down plot of probability scale of EF to log-X (see Figure 1-9). In Poissonian distribution, the mean ( $\bar{x}$ ) and the variance ( $s_x^2$ ) are equal.

In lognormal distribution ( $f(x) = a * \log_a(x)$ ), Y will be normally distributed regardless of the value of the base used (Gulliksen, 2006). Characteristics of this distribution include a slightly

## Characteristic EF plots for various X-scale/ y-scale relationships

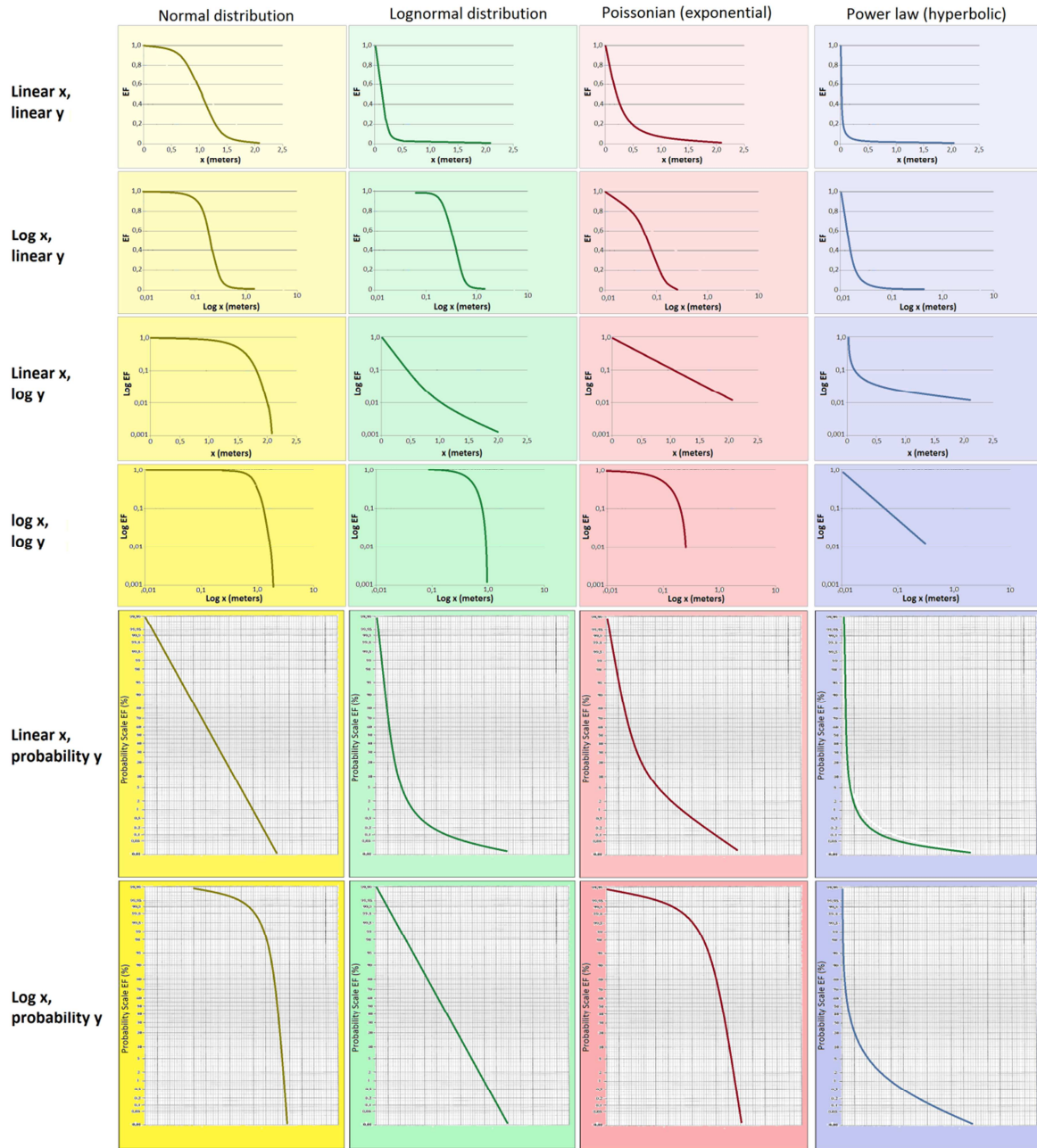


**Figure 1-9 EF plot diagnostic chart** used as a guide in analyzing EF plots to determine the distribution characteristics of data. Generally speaking, data that follows a trend may be analyzed using parametric treatment. Note that there is a concave down curve in every normal (Gaussian) plot except the linear x-probability scale y plot, which is a straight line. Note also, that every plot indicating the typical power law trend is concave up, with the exception of the log-y/log-x plot, which forms a straight line. *This diagram is based on the diagram in Nemeč, 2011.*

concave up curve in a log-EF to X plot, a concave down curve in log-EF to log-X plot, and a straight plot of probability scale EF to log-X.

Power law distributions ( $f(x) = ax^b$ ) can be distinguished by the element of self-similarity, the property of an object in that it retains its ratio of dimensions at any scale (Sornette, 2007). Any

geometric object that behaves self-similarly is called a fractal, and the power law that best describes the fractal forms a hyperbolic curve in a normal EF- plot.

Note in figure 1-9 that the different distributions have different characteristics that behave differently when the axes of EF plots change scales. On some scales, several trends look similar, but by changing the scale of the axes, the different distributions can often be distinguished. Each type of distribution forms a straight line on one unique axial scale combination. For example, when a EF plot has a log scale x axis, and a probability scale y axis, a log-normal distribution forms a straight line. When both axes are represented with a log scale, a power law distribution forms a straight line. In nature, however, trends don't follow textbook examples perfectly, therefore EF plots need to be interpreted (Davis, 2002)

Exceedence frequency plots (EF plots) were made using the fault thickness and displacement data from for each set of data analyzed (Appendix 3 for ANP data from the scan line only, Appendix 4 for data from ANP that includes the estimations from photographs, and Table Appendix 5 for fault data from Tidwell Draw). These plots are used to determine graphically what type of distribution the data displays. The type of distribution determines how the data should be analyzed. The data for displacement are sorted and ranked from lowest value to highest value. Repeated values are treated as equal and their rank is the mean of all ranking values of the tie (for example, if 1 and 2 values have the same thickness, then both will be ranked 1.5, and the next rank to follow would be 3, assuming the third rank isn't tied). There were 54 thickness observations made along the scan-line at ANP. Once the EF values for displacement were calculated (table 2-4a), six EF plots were produced representing the same data in different formats. Those plots are EF relationship to displacement, log EF to displacement, EF to log displacement, log EF to log displacement, EF to displacement on a probability scale, and EF to log displacement in probability scale.

Variance of the x and y values are found using the following equation, where x is either D or log D, and Y is either T or log T, as indicated in the respective plot.

$$S_x^2 = \frac{[n(\sum_i^n x^2) - (\sum_i^n x)^2]}{n(n-1)}; \quad S_y^2 = \frac{[n(\sum_i^n y^2) - (\sum_i^n y)^2]}{n(n-1)} \quad (\text{Formula 1.6}),$$

where n is the number of data pairs in the set,  $S_x^2$  is the variance of the x values, and  $S_y^2$  is the variance of the y values (Davis, 2002).

### ***Bivariate statistics***

Bivariate statistics involves combining two variables into one analysis to find a relationship between the two variables. In this analysis, it is possible to determine if relationship between the two variables exist, and if so, how they are related. Usually, one variable is dependent (y value) on the other variable (x value).

Covariance, the tendency of y to follow the trend of x, is determined using the following equation:

$$S_{xy} = \overline{xy} - (\bar{x} * \bar{y}) \quad (\text{Formula 1.7})$$

Where  $S_{xy}$  is covariance,  $\overline{xy}$  is the mean value of the product of x and y in a data pair,  $\bar{x}$  is the mean value of x, and  $\bar{y}$  is the mean value of y (Davis, 2002).

Correlation, the dependence of y on x, is a value between -1,0 and 1,0. Negative values represent a relationship where, as x increases, y decreases, and positive values suggest a direct relationship. 0 means there is absolutely no correlation (random spread), whereas a correlation value of 1,0 (-1,0) show a physical law. The formula used for correlation is:

$$r_{xy} = \frac{\Sigma[(x-\bar{x})(y-\bar{y})]}{\sqrt{\Sigma(x-\bar{x})^2 \Sigma(y-\bar{y})^2}} = \frac{S_{xy}}{s_x * s_y} \quad (\text{Formula 1.8})$$

where  $r_{xy}$  represents the Pearson's correlation coefficient,  $\bar{x}$  is the mean value of all values of x, and  $\bar{y}$  is the mean value of the y values (interpreted from Davis, 2002; Moore & McCabe, 2006). The correlation is tested for the confidence level using the Fisher test for the significance of linear correlation. Two assumptions are made, and then one is proven wrong with a set level of confidence determined by values found on Table D in Moore & McCabe, 2006. Those assumptions are:  $H_0$  states that the correlation is either equal to 0 or is the opposite sign to that found using formula 2.6.  $H_1$  states that the correlation is the same sign as that found in formula 2.4. The test function (t) is found using formula 2.7.

$$t = r_{xy} \sqrt{\frac{n-2}{1-r_{xy}^2}} \quad (\text{Formula 1.9})$$

If t is greater than  $t^*$  read from Table D in Moore & McCabe, 2006 for a given confidence level and the degrees of freedom (n-2), then  $H_1$  is accepted and  $H_0$  is rejected with that level of confidence indicated on the table.

The regression line takes the form  $y=bx+c$ . Coefficient (b) is found using the formula,

$$b = r_{xy} * \frac{s_y}{s_x} \quad (\text{Formula 1.10})$$

and the "nugget" value (c) is determined by using the mean values,

$$c = \bar{y} - b\bar{x}. \quad (\text{Formula 1.11})$$

These regression formulae are from Moore & McCabe, 2006. The coefficient of regression is tested using the Fisher test for the significance of regression. As with the Fisher Test for correlation, two assumptions are made then one is proven wrong. These assumptions are as follows.  $H_0$ : the coefficient of regression is either opposite in sign to that found using formula 2.8 or equal to 0.  $H_1$  assumes that the regression will have the same sign as that found in formula 2.8, and is not equal to 0. A test function is used to calculate a value based on the properties of the distribution of the data:

$$t = \frac{b \sqrt{\sum_i^n x_i^2 - n \bar{x}^2}}{\sqrt{s_y^2(1-r_{xy}^2)}} \quad (\text{Formula 1.12})$$

If the test function is greater than or equal to the  $t_\alpha$  function ( $t^*$ ) for a determined confidence level and the degrees of freedom ( $n-2$ ), then  $H_0$  can be rejected with the confidence determined.

The  $t_\alpha$  values can be found in Table D of [Moore & McCabe, 2006](#).

The regression line's goodness of fit ( $R^2$ ) describes the scatter associated with the plot, and is found by squaring the correlation coefficient. Higher values describe plots with less scatter from the predicted regression pattern ([Davis, 2002](#)). The range is between 0,0 (random scatter) and 1,0 (the y dimension value is completely determined by the x dimension value).

$$R^2 = r_{xy}^2 \quad (\text{Formula 1.13})$$

### ***Bias related to statistics***

When the distribution of the data is analyzed, certain trends may be difficult to recognize. Truncation is an effect caused by resolution limitations that result in the under-estimation of distribution frequencies. Causes of truncation may include sample size resolution, variations in fault densities, and finite size of the sample area ([Torabi& Berg, 2011](#)). Truncation may cause the data to veer away from a power law trend, masking the power law relationship.

Outlying observations can strongly affect statistical values such as sample mean, variance, and correlation ([Moore & McCabe, 2006](#)). The effects of an outlier on a sample depend on the distance of the outlier from the sample mean.

## 2 Geological setting

---

### 2.1 The Colorado Plateau and the Paradox Basin

My field sites for this project are located in the Colorado Plateau, a unit of lithosphere that occupies the southeast third of Utah, the western third of Colorado, the northwest quarter of New Mexico, and the northern third of Arizona (Figure 2-1B). The approximately 360,000 km<sup>2</sup> block is bounded to the west by the Great Basin, to the east by the Rocky Mountains. To the North, the Colorado Plateau is bounded by the Uinta Mountains, by the Rio Grande Rift Valley in the southeast, and to the south by the Mogollon Rim. The Colorado Plateau region is characterized by an arid climate resulting in sparse vegetation. The high altitude of the region and the fact that the Colorado platform sits in the rain shadow of the Sierra Nevada Mountains contributes to an average annual rainfall of approximately 25cm. The elevated platform is much higher than the base level in the Basin and Range province to the west. The result is a high rate of erosion and stream cutting, which leads to deep canyons, mesas and buttes cut by the Colorado River and its tributaries, the Green River and the San Juan River (Stokes, 1986; Foos, 1999; Marshak, 2005).

One unique feature of the Colorado Plateau is that it is bounded by intensely deformed rock, via mountains or rifting, yet overall and as a unit, the interior of the platform shows level, untilted and unfolded layering of sedimentary rocks (Foos, 1999). The Colorado Plateau sat at or near sea level by the end of the Cretaceous Period, as evidenced by the deposition of the Mancos Shale and other sediments, but now these surfaces lie at a mean elevation of 1936 meters above sea level. Approximately 3 kilometers of sediment were deposited on the Colorado Plateau during the Paleozoic and the Mesozoic eras. The types of sediments and depositional environments suggest a paleo-elevation at or near sea level. (Pederson et al, 2002).

Although the Colorado Plateau behaves as one bulk mass, some deformation did occur within the Colorado Plateau. Laccoliths such as the La Sal Mountains and uplifted areas such as the San Rafael Swell and the Uncompaghre Ridge are scattered across the platform. Basins have formed due to buckling of the platform in areas such as the Paradox Basin and the Uinta Basin. During the Paleozoic era, the western coast of North America (Laurentia, as it is referred to prior to the formation of the Atlantic Ocean) crossed through Utah. During the early Ordovician the shore line was approximately where the Wasatch Front lies today. After a brief regression, the ocean levels rose so that by late Ordovician, the area of the Colorado Plateau became an island (Stokes, 1986).

During the Late Carboniferous period, the formation of approximately 20 mountain ranges, collectively referred to as the Ancestral Rockies, occurred between Montana and Texas (Barbeau, 2003) in response to the collision between Laurentia and Gondwanaland (Trudgill, 2011).



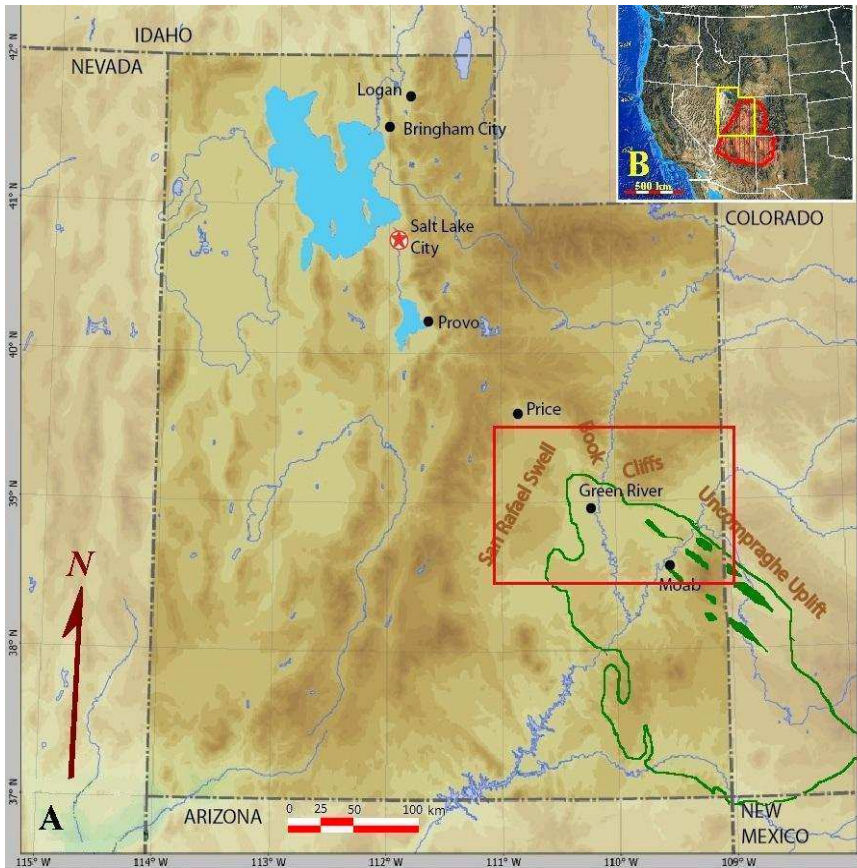
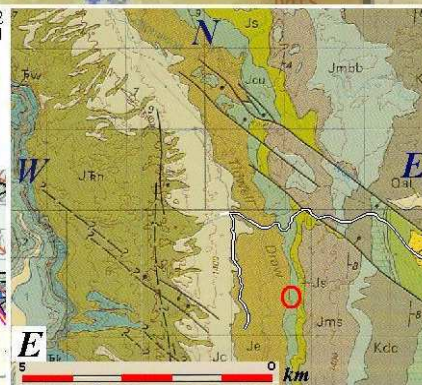
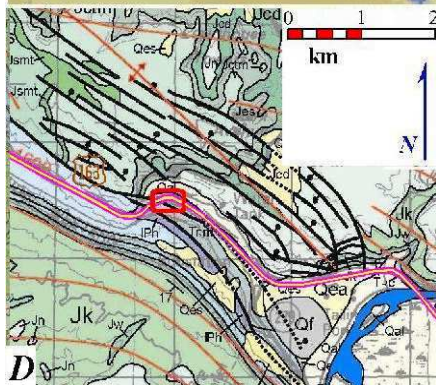
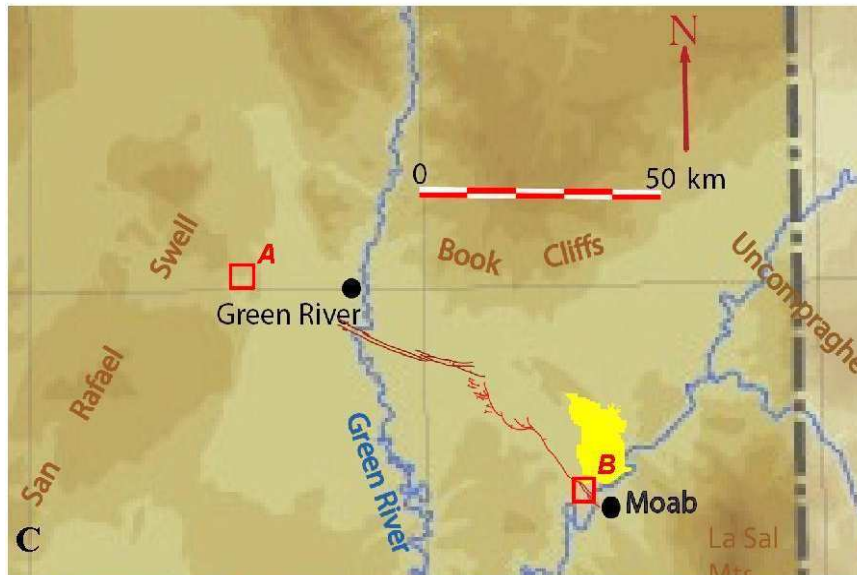


**Figure 2-1: Maps of the area.** **A)** A map of Utah. Encircled in green is the limit of salt extent of the Paradox Basin. The green areas trending NW-SE are approximate locations of salt anticlines that have formed from migration of salt. The red box shows the location of the map in figure 3C.

**B)** The western US. The Colorado Plateau is highlighted in red, and Utah is outlined in yellow. **C)** The northern Paradox Basin showing the locations where the research was carried out. The light red lineament is the map trace of Moab Fault. The dark red lineament northwest of Moab Fault is Ten Mile Graben. The yellow area in the southeast corner is Arches National Park. Box A is the site of Tidwell Draw, in San Rafael. The box is enlarged in E, below. Box B is the location of the entrance to Arches National Park (ANP), and is enlarged in D, below.

Work sites in **D** and **E** encircled in red. *A and C source: World Atlas Sites (sitesatlas.com) with fault traces source: Berg & Skar, 2005*  
*B source: Unavco (jules.unavco.org)*  
*D source: Utah Geological Survey Map 180, UGS and USGS*  
*E source: Witkind, 1988*



The continental collision, combined with subduction at the western boundary of Laurentia (Trudgill, 2011) led to the formation of the Uncompahgre uplift, a northwest trending, thick skinned ridge that formed in the northeast corner of the Colorado plateau. At the southwest edge of the Uncompahgre uplift, the Paradox Basin formed along Precambrian faults as a flexural foreland basin (Trudgill, 2011; Barbeau, 2003). Because of the highlands to the north and east, and barriers to the west and south, the Paradox Basin was an isolated basin in a restricted marine environment (Stokes, 1986; Doelling, 1988). During the latter half of the Carboniferous, Laurentia was positioned with the Colorado plateau near the equator. From approximately 310Ma to 305Ma, rapid subsidence and fluctuating eustatic sea level changes, combined with a high evaporation rate, led to a nearly 3km thick accumulation of cyclic dolomite, black shale and evaporites, forming the Paradox formation (Trudgill, 2011; Barbeau, 2003). During the upper Paleozoic and lower Mesozoic, differential loading, perhaps caused by alluvial fan deposition, led to the migration of salt into northwest trending, salt-cored anticlines in the Paradox basin. The Moab salt intruded anticline was fully formed by the early Tertiary (Baars and Doelling, 1987)

Later, during the Laramide Orogeny (80-40Ma), several monoclines developed within the Colorado Plateau. These uplifted regions formed from the same tectonic stresses that formed the Rocky Mountains, but on a reduced scale (Stokes, 1986; Bump & Davis, 2002; Maerten et al., 2001). Lacoliths, intrusive igneous rock that seeps between sedimentary layers, lifting the overburden to form mountainous blisters in the crust, formed in several places including the Henry Mountains and the La Sal Mountains of southeastern Utah.

There is much debate as to how and when the Colorado Plateau was uplifted (Pederson et al., 2002). Mechanisms suggested include the subduction of a theoretical section of crust, called the Farallon slab (Pederson et al., 2002), and eastward flow of overheated and over-pressurized crustal roots of the Sevier Mountains (McQuarrie & Chase, 2000). Suggested times range from the Laramide Orogeny (80-49Ma) (Stokes, 1986) to 5Ma (Foos, 1999) to a plateau wide uplift occurring in several stages (Pederson, 2002).

### **2.1.1 The Moab Fault**

The Moab Fault (Figure 2-1C and 2-1D) is located in southeast Utah and is a normal fault with approximately 950 meters of throw, juxtaposing Carboniferous Honaker Trail Formation of the Hermosa group (Trudgill, 2011) on the foot wall with the Jurassic Slick Rock member of the Entrada Formation on the hanging wall (Olig et al, 1996). Moab Fault (light red in figure 2-1C) is at least 45 kilometers long, stretching from Moab in the southeast to near Ten Mile Graben (dark red lineament in figure 2-1C). It has been suggested that the two may link up (Foxford et al, 1996). The Southern section of Moab Fault is one central trace that splays out into two branches north of the Colorado



River (Foxford et al, 1996). The fault continues southeastward across the Colorado River and into the Spanish valley (Foxford et al., 1996, Olig et al., 1996). Other faults that are not connected in fault trace may also be splays (Olig et al., 1996). The northern portion of the fault (north of Corthouse Rock) splays out into a series of parallel SE-NW trending faults that are hard-linked in what might be described as a “fault train” (Foxford et al., 1996, Olig et al., 1996). Subsequent faults curve eastward toward and terminate against the previous faults of the sequence, forming hard links.

The development of Moab Fault is controversial (Olig et al., 1996). In the late Carboniferous Period, the Paradox Basin became an enclosed bay in a restricted marine environment (Stokes, 1986; Barbeau, 2003). The location of the Colorado Plateau at the time meant that the Paradox Basin experienced high evaporation rates, leading to a thick deposition of evaporates with some cyclical carbonates and shale, referred to as the Paradox Formation. Along the Northeastern portion of the basin the Paradox Formation was at least 1,8 km thick (Foxford et al., 1996). The extent of the evaporites in the basin is shown by the green outline in Figure 2-1A. The deepest portion of the basin, and the area with the thickest evaporite deposits is the northeast section parallel with the Uncompahgre Uplift. Because of ductile and low density nature of evaporates, as differential loading of sediments occurred over the Paradox Basin, the salts flowed and collected to form bulging salt anticlines over the portion of the basin with the thickest deposits of evaporites. It has been suggested that the salt anticlines formed over the deepest areas of the basin, areas that sit over basement faults that were periodically active from the Proterozoic up through the time of the

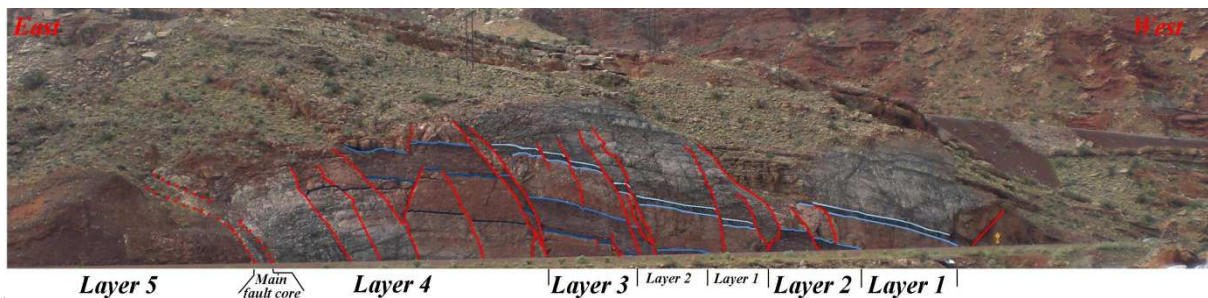


**Figure 2-2: The outcrop of the Moab Fault as viewed from Arches National Park Visitors Center.** The red lines indicate faults, whereas the blue lines indicate stratigraphic boundaries. Note that the lighter shades of blue represent strata that is higher up on the stratigraphic column than darker shades, and that by tracing a shade laterally, one can follow the stratigraphic boundary across faults. View is approximately 200m across. Note the street sign under the rightmost fault for scale. The layer description at the bottom refers to bedding described in Figure 2-3 *Photograph by Katrine Olsen Grindhaug.*

Laramide Orogeny, in the early Tertiary period (Foxford et al., 1996). These zones were areas of least confining pressure (Baars & Doelling, 1987) which developed into salt anticlines trending SE-NW (wide green lineaments on the northeastern side of the Paradox Basin in Figure 2-1A) parallel with the Uncompahgre Uplift. It has been suggested that Moab Fault was initiated by the motion of the

salt during the formation of these anticlines and that the fault was active during two episodes. The first episode lasted from the beginning of the Triassic through to the middle of the Jurassic. Observations suggest that there was no fault activity in the latter half of the Jurassic or through most of the Cretaceous, but activity was renewed at the end of the Cretaceous with the onset of the Laramide Orogeny, when faults were reactivated (Foxford, 1996; Davatzes & Aydin, 2005; Solum et al., 2010). Baars & Doelling (1987) suggest that if the Moab Fault is truly a normal fault, then there must have been some extension associated with the relaxation of the Laramide compressive stresses following the orogeny.

Another suggested mechanism for fault growth is dissolution of salts by groundwater (Olig et al., 1996; Berg et al., 2005; Oviatt, 1988), however, Olig et al., (1996) point out geological evidence to suggest that neither salt diapirism nor salt dissolution have contributed to the displacement of Moab Fault. First, the greatest displacement occurs 5km to the north of the Colorado River, although the river is the greatest source of water to the region. Olig et al., (1996) make an argument that there should be greater displacement closer to the river if dissolution of salts caused fault movement. Second, if diapirism is the cause of displacement along Moab Fault, the maximum displacement should have been in Moab Valley, 5km south of the Colorado River, where the salt diapir appears thickest. Displacement at that location is only 300m. Furthermore, Olig et al., (1996) report that the oldest deposits to bury the trace of Moab Fault are Pleistocene alluvial gravels, the youngest deposits deformed by the fault are Cretaceous in age, and most of the deformation post-dates Mesozoic Diapirism. This conclusion agrees with the dates of 63 to 40Ma reported by Davatzes & Aydin (2005). Olig et al., (1996) suggest that the fault was caused by Cenozoic thin-skinned extension over the Moab salt anticline, satisfying the requirements for the Moab Fault as a normal fault as asserted by Baars and Doelling (1987).

#### *Lithostratigraphy at the Moab Fault site (ANP)*

The site of the study at Moab Fault is located at a road-cut along highway 163 within site of the visitor's center at Arches National Park (ANP), north of Moab, Utah. The outcrop exposes late Carboniferous Honaker Trail sedimentary rocks of several types. Unlike the Paradox formation salts that were deposited prior to the Honaker Trail Formation, these sediments represented a more open marine environment (Trudgill, 2011), with cyclic deposition of primarily carbonates, shale and sandstone (Nuccio & Condon, 1996). Although the sediments of the Honaker Trail Formation are dominated by carbonates throughout the Paradox Basin (Barbeau, 2003; Trudgill, 2011), the proximal northeastern area of the basin contains significant accumulations of eolian and fluvial sedimentary rock (Nuccio & Condon, 1996), as can be observed at the study site (Figure 2-2, layers 1 and 3). The

following is a description of the rock encountered at the Moab Fault location (Figure 2-3)(Layers in Figure 1-5 correspond to the respective layers in Figure 2-2).

Layer 4 is a massive limestone that has ten meters of exposure at the outcrop. Fossils of crinoids (represented by a star in figure 2-3, layer 4) and brachiopods (represented by a triangle in figure 2-3, layer 4) (Barbeau, 2003) have been observed at this site. In some areas vuggy porosity has been observed in fractures and fault cores. The limestone is well cemented and not friable.

Layer 3 is a clean, well sorted, massive, brown-orange, fine grained sandstone that is 6,40 meters thick. Both of the boundaries to layer 3 are sharp boundaries. No fossil has been observed. The pattern formed from bleached areas in isolated patches tend to resemble trough cross-bedding, although no other primary structural fabric is visible. This bed is not friable

Layer 2 has been divided into four sub-layers based on fabric which indicate different depositional environments. Layer 2d is a coarse-grained sandstone with sub-angular grains, showing parallel lamination. The lower boundary of layer 2d is a sharp boundary that is flat. Lenses of gravely conglomerate with clasts up to 5cm in diameter can be distinguished within layer 2d. The layer is light blue-gray and contains secondary mica. Grains of white and stained quartz and red feldspar are also present. A layer of darker, finer grained material lies near the top of this bed. This bed is very friable and can be crushed by hand.

2c resembles 2d in color and in mineral composition. The main difference is that 2c shows planar cross-bedding, not parallel lamination. Gravel lenses parallel to the cross-bedding are thinner and contain grains up to 5mm in diameter. A clear boundary separates parallel laminated 2d layer from the cross laminated 2c layer. This sandstone is also very friable.

Layer 2b is a medium to coarse grained, parallel laminated sandstone with mica and clay matrix. The layer is approximately 1,50 cm thick. Mica may be observed in this layer, but not in the same granular form that was observed in 2c and 2d. A sharp, planar boundary

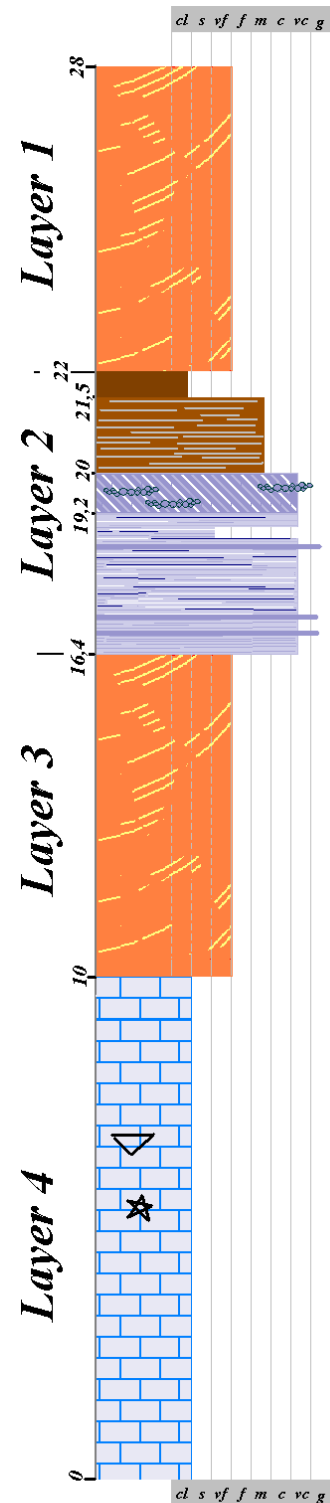


**Figure 2-3 The stratigraphy of the Honaker Trail Formation at the Moab Fault site, showing the beds intersected by the scan line.**

separates 2c from 2b. The sandstone in this layer is not very friable, but grains can be removed by hard rubbing.

Layer 2a is a brown shale with a small amount of mica. No laminations were observed in the outcrop, but a hand sample does show foliation/ cleavage parallel to bedding. A sharp, planar boundary separates layer 2a from layer 2b. Layer 2a is 50 centimeters thick. As with most shales, this bed is friable.

Layer 1 (furthest right in figure 2-2) is a clean, beige/ orange, massive, well sorted very fine sandstone with well-rounded grains. No fossil or trace fossil was observed in the sandstone layer. Isolated patches of the rock face display bleached patterns revealing a fabric resembling low angle-tangential cross-bedding, dipping eastward. The sandstone is well cemented and not friable. The layer is 6,05 meters thick, with a sharp planar boundary.

The stratigraphy and literature written about the Honaker Trail Formation suggest that during the duration that the sediments in this scan line were deposited, the area was likely first a shallow marine environment , maybe a bay. The environment was not so restricted that evaporites could form (Nuccio & Condon, 1996). A reef may have formed here. Winds from the west picked up sand and deposited it at this site, creating the eastward dipping trough cross beds that can be seen in the bleached pattern of the third layer. Sometime later, a river channel probably ran through this area. Although the cross bedding in 2c dip westward, a meandering stream can produce cross beds in any direction it meanders, regardless of the direction of the source, as can be observed along the nearby Colorado River today. Sometime later, clay was deposited, perhaps in a lacustrine environment. It is interesting to note that there are no coal deposits or rootlets in these sediments. It is possible that a coal layer may have formed, but was eroded away from this location. It is also possible that the area was arid, as it is today, so that no coal was produced. The fluvial/lacustrine (?) sediments were buried by more sand blown in from the west, forming the sandstone that is layer 1.

Although it wasn't closely examined, the next bed above the first sandstone layer resembles fluvial deposits similar to those found in layer 2. This bed was approximately 50 cm thick. Immediately above this bed sits another pink and green limestone bed, as observed in layer 4. This bed is several meters thick. If these beds are similar layers, this would indicate the cyclicity of sediments during the deposition of the Honaker Trail Formation described by Trudgill (2011), Barbeau (2003) and Nuccio & Condon (1996).

The Moab Fault is located on the southwest edge of the Salt Wash Anticline (Foxford et al., 1996) and the Moab Anticline (Olig et al., 1996), collapsed anticlines formed by salt diapirism during the Triassic, Early Jurassic periods, then resumed in the late Cretaceous- early Tertiary periods. The collapse of the anticlines was caused by the dissolution of salt subsequent to the formation of the anticline, leading to the formation of valleys in the region such as the Moab Valley (Baars & Doelling,

1988). The geometry of the fault structure at Arches National Park is that of a faulted anticline (Foxford et al., 1996).

### 2.1.2 San Rafael Swell

The San Rafael Swell is an uplifted region that lies to the northwest of and borders the Paradox Basin at the northwest corner of the Colorado Plateau in central Utah (Figure 2-1A) (Nuccio and Condon, 1996; Bump and Davis, 2002). The formation of San Rafael Swell has been associated with the late Cretaceous/ early Tertiary Laramide Orogeny (Stokes, 1986). San Rafael Swell formed similar to other orogenic mountain ranges in the region, but the deformation was on a much smaller scale (Stokes, 1986; Bump & Davis, 2002). During the time of the Laramide Orogeny, a thrust fault developed under San Rafael Swell, forming an upraised region with an east verging fold. The western limb dips gently and the eastern limb dips steeply to form a monocline stipulated with flat-irons. The approximately kidney shaped uplift (Maerten et al., 2001) stretches north to south for 120km and east to west for 50 km (Johnson and Johnson, 2000). The formation of the San Rafael Swell led to some flexural slip (layer parallel slip, (Johnson and Johnson, 2000)). The blister in the crust caused the surface area to expand. The expansion of the surface should have led to the development of thin skinned extensional faults as the surface was stretched to accommodate the uplift.

The area described in this research is in Tidwell Draw, an area of the eastern portion of San Rafael Swell north of interstate I-70 and west of US Highway 6. Locally, the area is known as Smith's Cabin. To the west are outcrops of eolian Navajo sandstone which form flat iron outcrops. To the east are outcrops of shale and fine sandstone which belong to the Curtis Formation (Witkind, 1988). The climate is arid and the ground is only partially covered by vegetation in the form of grasses and low growing shrubs, giving outcrops good visual exposure. Parts of the outcrop presented in this research form a steep slope of loose shale, causing difficulties when taking measurements. Many parts of the outcrop were covered in scree.

The base of the outcrop consists of thin interbedded laminae of

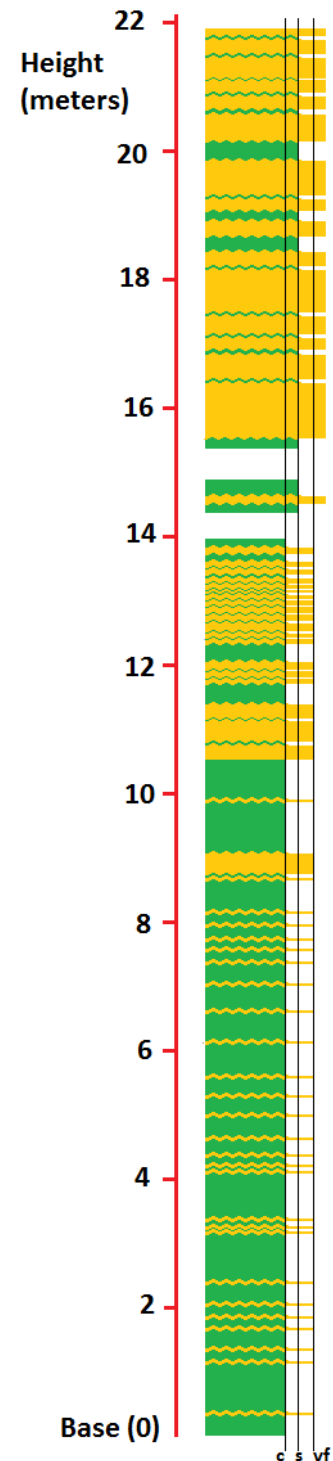


Figure 2-4: Lithostratigraphic column of the outcrop studied at Tidwell Draw in central Utah. The two facies were shale /siltstone interbedded laminae (green), and very fine sandstone (yellow). The thicker sandstone layers displayed hummocky cross bedding. All layer boundaries displayed symmetrical ripples.

shale and silt. (See Figure2-4) There are a few layers of very fine sandstone exhibiting symmetrical ripples spaced approximately five centimeters from one another. These sandstone beds are between one and three centimeters thick, and have been used as marker beds. Some of these beds were observed to pinch out. The base of the outcrop tends to be very friable, and loose scree covers some of the larger faults, burying them. The scree consists of small shaley flakes, and larger, platy clasts of thin sandstones displaying symmetrical ripples on both sides. Higher up the side of the outcrop the scree also includes thicker blocks of sandstone. Traveling up the face of the outcrop, the sandstone beds appear more frequent, and increase in thickness between three and ten centimeters. Near the top of the nearly 22 meter high outcrop, thicker sandstone beds, between 0,30m and 0,80m, display hummocky crossbedding. These thicker beds are separated from one another by thinner beds of shale or siltstone, some as thin as 0,01m. No fossils were observed.

The outcrop description fits the description of an offshore transition zone, somewhere near the lower shoreface. Storm waves, which are larger than mean wave base, provided energy to deliver the sand and stir up the finer sediment, depositing the sand layers and lenses. Between storms, the water below the mean wave base doesn't have the energy to sweep the larger sand grains. The water between storms is generally calm enough below the mean wave base that silt and clay settle on top of the hummocky sand layers. Thin interbedded laminae of clay, silt and very fine sand may have been deposited by processes associated with tides. This description fits well with Curtis formation deposits, which are exposed in outcrop in the Tidwell Draw area. (Witkin, 1988; Kreisa & Moiola, 1986). symmetrical ripples indicate wave motion in a north-south heading. A few of the sandstone layers show asymmetrical ripples, indicating a paleo- current flow in one direction. All of the layers on this outcrop have a 14 degree dip towards a heading of 65 degrees.

Unlike the Moab Fault site at ANC, this location is remote, 11 kilometers from the nearest paved road. Due to time constraints, commitments, a flat tire and occasional bad weather, less data was recorded at San Rafael Swell than was desired.





**Figure 2-5: The outcrop that was studied at Tidwell Draw in San Rafael Swell.** Note the field researcher over the arrow for scale. The center of the photograph points towards east. Several of the larger faults can be seen in the valleys within the shaley base, as well as where the massive sandstone shows discontinuity. *Photograph by Katrine Olsen Grindhaug*

# 3 Results

## 3.1 Moab fault at Arches National Park entrance (ANP)

### 3.1.1 Structural characteristics at ANP

The faults and the fractures observed at the ANP site are a part of the footwall damage zone of the Moab Fault. From the scan line, 54 normal faults, 8 strike slip faults and 139 fractures were logged and measured. The strike, dip, displacement and gouge thickness data are presented in Appendix 1, in the Appendix. There is scatter in the distribution of fracture orientation but most of the fractures observed at the Moab Fault site have a NW-SE trend, parallel with the Moab Fault (see figure 3-1). Faults measured in the same area also showed a trend of NW-SE, running roughly parallel with the orientation of the salt anticlines in the area and with the Moab Fault itself. There appears to be a small N-S component and an E-W component that hasn't been satisfactorily explained. The NW-SE alignment of the fault and fracture orientation geometries at ANP strongly suggests that they are controlled, either directly or indirectly, by the geometry of the surrounding geological structures.

Travelling eastward from the start of the outcrop towards the fault, it is clear that the bedding planes have been rotated a few degrees with each fault, from an apparent bedding dip of 10 degrees westward in the western end of the outcrop to perhaps 5 degrees eastward adjacent to the main fault. Seven faults with slickensides indicating horizontal displacement perpendicular to the strike direction of the Moab fault were found within a 20 meter length along the scan line. These horizontal faults were observed in the center of the outcrop approximately where layer 3 and layer 4 meet (see Figure 1-4). In the carbonate layer (layer 4 in Figures 1-4 and 1-5), fracture density increases with a decrease in distance to the main fault. The most proximal six meters of the footwall to the main fault core are so gnarled that the thickness of any fault here can not accurately be established, marker horizons cannot be accurately

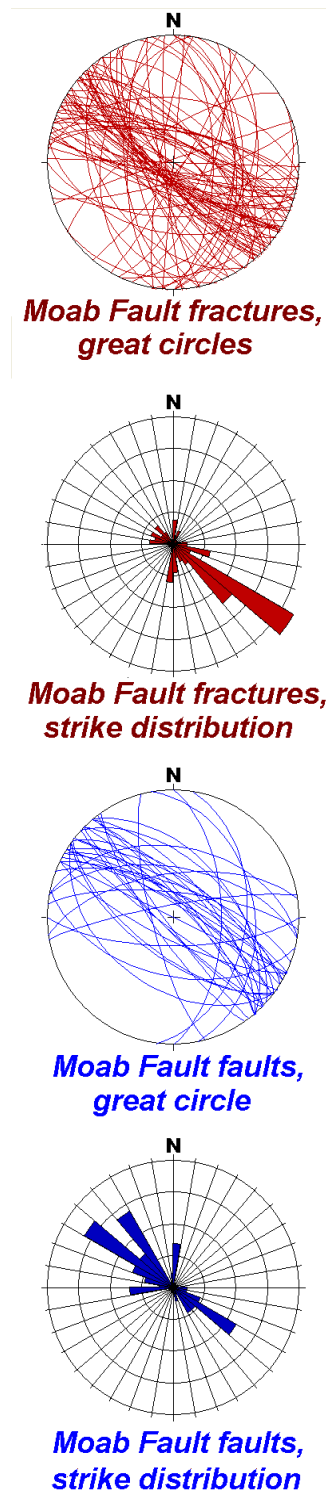


Figure 3-1: Moab Fault fractures (red) and faults (blue) generally have a NW-SE trend, parallel with the main fault and salt anticlines of the region, indicating the direction and concentration of shear stresses in this area of the Colorado Plateau. Each ring in the rose diagram represents 6.25% of all samples measured. Each wedge represents 10 degrees.



traced, and faults with small displacements cannot be readily identified (see the left side of figure 1-4, adjacent to and east of the main fault).

For the smaller faults at ANP, there was some variation in fault thickness along the fault plane, especially in the vicinity of fault junctions, and along the faults with greater displacement (Foxford et al., 1998). The fault with the largest displacement at ANP (11,2m) averaged 10 cm in thickness. The thickness of this fault increased abruptly to 1,90m near the bottom of the outcrop, indicating the rapid change in thickness that can take place over a short distance (Foxford et al., 1998) (Figure 3-2).

### 3.1.2 Results of statistical analysis from ANP

#### *Univariate analysis and EF plots*

The thickness and throw readings for the faults at ANP can be found in Table 3-1 A. The plots of the exceedence frequency (EF) to throw for the ANP site, excluding data the data obtained through photo estimations, are displayed in Figure 3-3. The linear plot of EF to linear throw data (Figure 3-3A) shows a relatively smooth concave up pattern similar to a hyperbolic or logarithmic distribution. In the plot of EF to logarithmic values of throw (Figure 3-3B) the data forms a curve that is almost linear and slightly concave upward. For the diagram showing logarithmic values of EF for linear values of throw (figure 3-3C), the curve appears concave up, except for the trailing pattern formed by the 3 points with the lowest EF values. For the log EF-log throw plot (figure 3-3D), the inner 48 data points (out of 54) form a rather straight segment of the curve, and deviates from the straight pattern in the first two points and the last three points. On the probability scale of EF to throw (figure 3-1E) the curve remains close to the y-axis until forming a concave up curve. In the Probability scale EF to logarithmic representation of throw (figure 3-3F) the curve is almost a straight line, showing a slightly concave upward shape.

The trend between EF and throw (D) for the faults at ANP were analyzed for comparison of a logarithmic distribution and a power law distribution. A normal distribution has been ruled out because the graphical representations of the plot do not support a normal profile. Normal



**Figure 3-2: Fault core thickness fluctuates.** Faults may vary in width by a factor of 19 over very short distances at ANP, as seen in this illustration. Cataclasite fills a fault core that is 10cm across at the top of the image (bounded in red lines). Approximately 3,5m from the base of the outcrop, the fault core widens to 190cm across within a two-meter stretch down the dip of the fault plane. Note the yellow, 2m long measuring stick for scale. *Photograph by Katrine Olsen Grinhaug.*

profiles are characterized by a linear trend in the probability scale EF to linear scale throw, and concave down trends in the log EF- throw plot and the log EF-log throw plot. The exponential trend can also be ruled out graphically because of the clearly non-linear trend in the log EF to throw plot. Furthermore, the concave up trend in the probability scale EF to log throw plot is not characteristic of an exponential distribution.

A straight line in the log EF-log throw plot is characteristic of a power law relationship. This plot has a long, nearly straight segment consisting of 90% of the points plotted. Only the high end members and the low end members of the plot are not included in this straight segment. Power law distributions tend to involve fluctuations at the tail members that make the distribution difficult to detect (Torabi & Berg, 2011), however, in the distribution of throw measurements at ANP, the middle 90 percent of throw measurements form a nearly straight line in the log-log plot where a logarithmic distribution is expected to bend in a concave down pattern.

When the data acquired from photographs are included (Figure 3-4,A-F), the trends of EF to throw are consistent with the EF plots not containing the photographic estimations (Figure 3-3). There can be two reasons for this result. The first is that the corrections to the data may produce favorable results that bias the curve. The corrections were meant to compensate for errors in the photographic estimations. This compensation may act as a bias to draw the points closer to the expected curve. Any action that draws the points away from the state in which they were observed removes them from the natural randomness from which they were derived. While this effect was not intended, it is true that the photographic estimations are biased from the true nature for which they were observed. This bias must be considered when analyzing the results which include the photographic estimations. However, there were eight estimations, which is less than 20% of the total number of data without the photo estimations. The relative scarcity of the photo acquired data may be the second reason the EF plots in figure 3-4 are similar to their respective EF plots excluding photo acquired data in Figure 3-3.

The plots of EF-fault thicknesses for the ANP data without photos are displayed in Figure 3-3 (G-L), the data when plotted can be divided into two segments that are joined at a change-point in the plot, where an apparent discontinuous change in the curvature of the plot occurs. Points with thickness values less than or equal to 0,015m are highlighted in green, while >0,015m are highlighted in orange. In the EF- thickness plot (Figure 3-3G), the overall plot forms a concave up trend, as do each of the subsets. In the EF- log thickness plot (Figure 3-3H) the top left of the plot appears to be straight and sloping downward at approximately 45 degrees. Where the plot reaches 0,015m thickness, the plot bends downward to approximately 60 degrees, forming a concave-up curve where the plot approaches no slope along the right side of the plot. The overall shape of the plot approaches a left facing sigma or “s” shape. The section  $T \leq 0,015m$  appears straight and

downward sloping. The subset  $T > 0,015\text{m}$  forms a concave up curve that levels out on the right side of the plot. On the log EF- thickness plot (Figure 3-3I), the overall trend of the curve tends to be roughly linear to slightly concave up. The subset  $T \leq 0,015\text{m}$  is slightly concave up. The plot of the subset  $T > 0,015\text{m}$  has a slightly more pronounced concave up trend. The plot of log EF- log thickness (Figure 3-3J) shows two straight segments of different slopes joining at  $T=0,015\text{m}$ . The subset  $T \leq 0,015\text{m}$  slopes downward at approximately 20 degrees, whereas the subset  $T > 0,015\text{m}$  slopes downward at approximately 60 degrees. The probability scale EF- thickness plot (Figure 3-3K) shows an overall concave up trend, the left side being nearly vertical, and the angle of the slope gradually declining as the end travels to the right. The subset  $T \leq 0,015\text{m}$  falls steeply, but shows a concave up trend. The left side of the subset  $T > 0,015\text{m}$  slopes steeply, then gradually decreases in slope as the trend moves to the right. Where the two subsets meet is not as pronounced on the probability scale EF- thickness curves as it is on figure 3-3J, but it is noticeable. On the plot of probability scale EF-log thickness (figure 3-3L), the overall trend of the plot appears as a slightly concave down, almost straight trend. This trend is formed by the joining of the two subset trends, each being slightly concave up in shape.

As with the throw data, the overall EF trend appears to follow a logarithmic relationship. The difference is that in the log-log graph (Figure 3-3D and Figure 3-3J), there are two straight sections, indicating two power-law trends that intersect at  $T=0,015\text{m}$ , and  $EF=49\%$ . Two distinct straight segments suggest that there is a power law distribution for each segment. This distribution arrangement, where overall distribution is log-normal, yet sections within the curve display power law distribution characteristics, is not a new observation. In describing the distribution of turbidite beds in Italy, Felletti & Bersezio (2009) also observed overall logarithmic trends formed by two power law segments that met at a change-point. The distribution trend for faults less than 15 millimeters is not the same as the power law trend for faults with thickness greater than 15 millimeters at ANP.

When the data acquired from photographs (shaded data in table 3-1A) are included in the EF plots (Figure 3-4), the results are very similar to the data that doesn't include the estimations from photos. Although the EF plots in Figure 3-4 describes a data set that contains 15 percent more data than the scan-line data at ANP, the descriptions for the EF plots without the photograph estimations are valid also for the EF plots which included the data from photographic estimations. This consistency in the frequency distribution trends indicate that data estimated from photographs can be an acceptable approach to data gathering where direct measuring methods prove difficult or unsafe to perform.

**Table 3-1:** Fault data from this project. Shaded values were obtained from photographs. D= fault throw, T= fault core thickness.

A: Moab Fault at ANP				B: Tidwell Draw			
D	T	log(D)	log(T)	D	T	log(D)	log(T)
0,00500	0,001	-2,301	-3	0,02	0,002	-1,699	-2,69897
0,01500	0,005	-1,8239	-2,301	0,02	0,002	-1,699	-2,69897
0,02000	0,005	-1,699	-2,301	0,02	0,001	-1,699	-3
0,02000	0,02	-1,699	-1,699	0,025	0,001	-1,6021	-3
0,03000	0,015	-1,5229	-1,8239	0,03	0,006	-1,5229	-2,22185
0,03000	0,008	-1,5229	-2,0969	0,04	0,02	-1,3979	-1,69897
0,04000	0,005	-1,3979	-2,301	0,04	0,001	-1,3979	-3
0,04000	0,003	-1,3979	-2,5229	0,05	0,002	-1,301	-2,69897
0,04000	0,009	-1,3979	-2,0458	0,05	0,001	-1,301	-3
0,04900	0,002	-1,3098	-2,699	0,05	0,005	-1,301	-2,30103
0,05000	0,002	-1,301	-2,699	0,06	0,002	-1,2218	-2,69897
0,05000	0,004	-1,301	-2,3979	0,07	0,003	-1,1549	-2,52288
0,05000	0,001	-1,301	-3	0,07	0,005	-1,1549	-2,30103
0,05000	0,023	-1,301	-1,6383	0,12	0,05	-0,9208	-1,30103
0,05000	0,0155	-1,301	-1,8097	0,165	0,02	-0,7825	-1,69897
<b>0,05942</b>	<b>0,001439</b>	<b>-1,2261</b>	<b>-2,842</b>	0,6	0,022	-0,2218	-1,65758
0,06000	0,0115	-1,2218	-1,9393	1,02	0,02	0,0086	-1,69897
0,06000	0,00355	-1,2218	-2,4498	1,66	0,09	0,2201	-1,04576
<b>0,07263</b>	<b>0,001439</b>	<b>-1,1389</b>	<b>-2,842</b>	1,95	0,01	0,29	-2
0,075	0,002	-1,1249	-2,699				
0,08	0,02	-1,0969	-1,699				
0,085	0,0088	-1,0706	-2,0555				
0,1	0,02	-1	-1,699				
0,1	0,02	-1	-1,699				
0,1	0,0185	-1	-1,7328				
0,11	0,002	-0,9586	-2,699				
0,12	0,016	-0,9208	-1,7959				
0,12	0,01	-0,9208	-2				
0,135	0,002	-0,8697	-2,699				
<b>0,14653</b>	<b>0,003237</b>	<b>-0,8341</b>	<b>-2,4899</b>				
0,15	0,001	-0,8239	-3				
<b>0,15453</b>	<b>0,003237</b>	<b>-0,811</b>	<b>-2,4899</b>				
0,17	0,02	-0,7696	-1,699				
0,2	0,0105	-0,699	-1,9788				
0,22	0,005	-0,6576	-2,301				
<b>0,23062</b>	<b>0,036004</b>	<b>-0,6371</b>	<b>-1,4436</b>				
0,24	0,02	-0,6198	-1,699				
0,3	0,02	-0,5229	-1,699				
0,3	0,0165	-0,5229	-1,7825				
0,34	0,0035	-0,4685	-2,4559				
0,4	0,02	-0,3979	-1,699				
0,434	0,003	-0,3625	-2,5229				
0,45	0,0025	-0,3468	-2,6021				
<b>0,47425</b>	<b>0,006835</b>	<b>-0,324</b>	<b>-2,1653</b>				
0,5	0,18	-0,301	-0,7447				
<b>0,59055</b>	<b>0,03189</b>	<b>-0,2287</b>	<b>-1,4963</b>				
0,6	0,02	-0,2218	-1,699				
0,748	0,03	-0,1261	-1,5229				
0,8	0,015	-0,0969	-1,8239				
0,8	0,04	-0,0969	-1,3979				
1,1	0,0625	0,04139	-1,2041				
1,2	0,016	0,07918	-1,7959				
1,5	0,03	0,17609	-1,5229				
1,73	0,03	0,23805	-1,5229				
2	0,0525	0,30103	-1,2798				
2	0,015	0,30103	-1,8239				
2	0,03	0,30103	-1,5229				
2	0,03	0,30103	-1,5229				
<b>2,3169</b>	<b>0,077823</b>	<b>0,36491</b>	<b>-1,1089</b>				
2,8	0,08	0,44716	-1,0969				
3	0,04	0,47712	-1,3979				
11,2	0,12	1,04922	-0,9208				

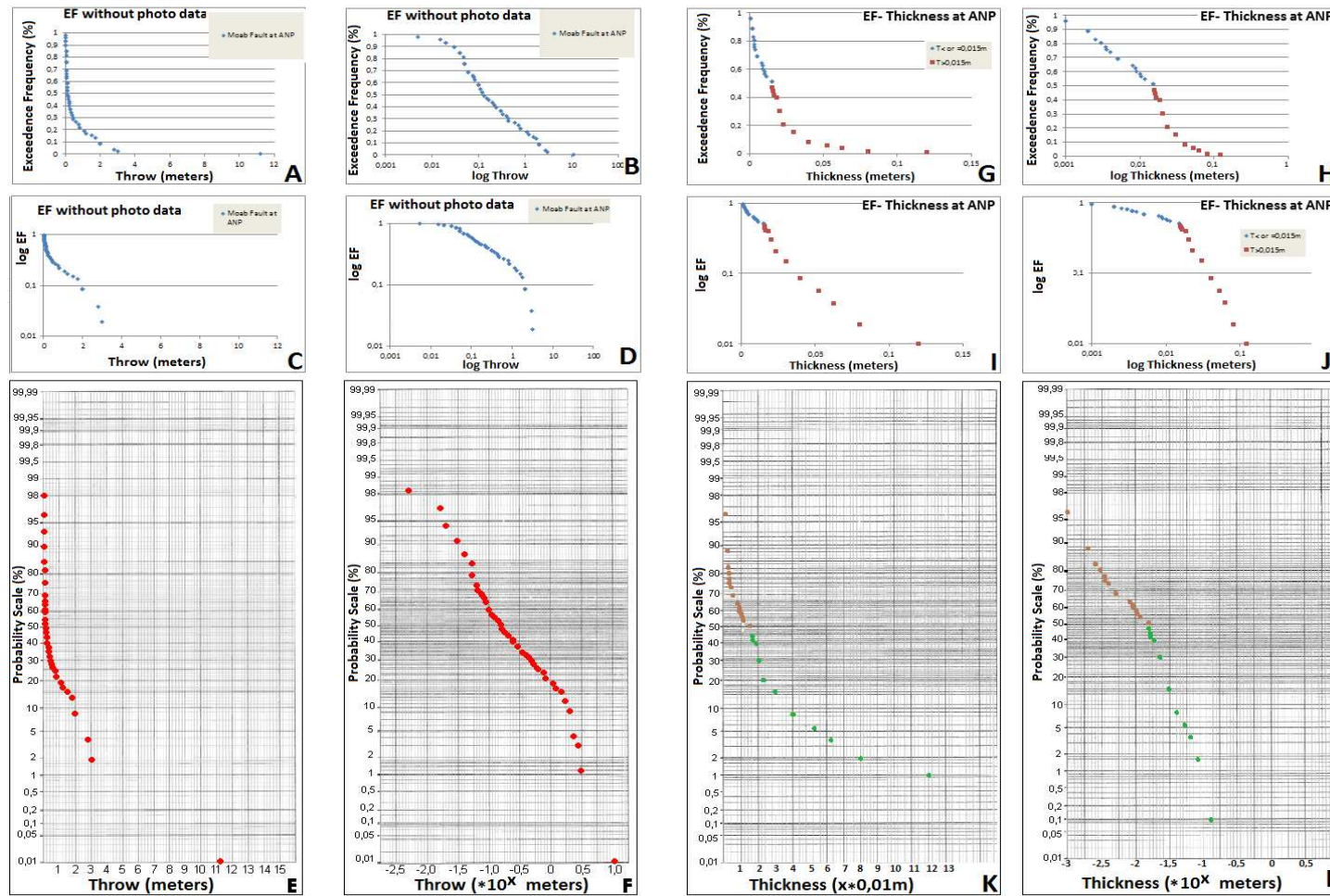


**Figure 3-3: Exceedence frequency (EF) plots for the Moab Fault fault throw (A-F) and thickness (G-L) scan line observations. A** shows the EF in linear scale in relation to throw, which is also in linear scale. **B** shows EF in logarithmic scale in relation to displacement in linear scale. **C** shows EF I linear scale in relation to the logarithmic value of displacement. **D** displays both axes in logarithmic scale. **E** shows EF in probability scale in relation to displacement in linear scale. **F** displays the EF value in probability scale in relation to the logarithmic value of displacement. G-L follow the same order as A-F, using fault core thickness data. Data for A-F is from Appendix 3.

Faults with thicknesses less than 0,015m tend to have a lesser change in EF for a given shift in thickness than for the faults that have a thickness greater than 0,015m. Plots of thickness that include the data acquired from photographs can be seen in Figure 3-3G-L. The plots that include the photographic estimations appear to maintain the characteristics of the plots that contain only scan line data.

**Table 3-2** Calculations and analysis for various data sets represented in this project. These calculations are for linear regression of either linear values (columns 1, 3, 5, and 7) or logarithmic values (columns 2, 4, 6, and 8) of displacement (D) and thickness (T) for faults represented at the locations indicated. Formulas used for these calculations are discussed in chapter 2.  $S^2$  is variance for the respective D or T data, S is standard deviation, Dm is mean throw, Di is an individual throw datum for a given rank, Tm is mean thickness, t is a test value for the Fisher test,  $t_r$  is the Fisher test value for correlation,  $t_b$  is the Fisher test value calculated for regression, and  $t^*$  is the critical value, which is found in Table D of Moore & McCabe, 2006. All  $t^*$  values are for a significance level of 0,005 except for the correlation value for linear calculations of San Rafael swell data, which uses a significance level of 0,01.  $R^2$  is the regression goodness of fit, b is the slope of the regression line, c is the expected value of thickness from the regression when D (or log D) is zero.

	ANP w/o photos-linear	ANP w/o photos log values	ANP with photos linear	ANP with photos log values	San Rafael linear	San Rafael log values	Published data linear scale	Published data log scale
sum D	38,366	-38,305	42,911	-43,14	6,06	-19,859	191391	-8,7354
mean D	0,71974	-0,72274	0,69212	-0,69581	0,31895	-1,0452	157,14	-0,007172
sum D <sup>2</sup>	169,84	53,96	175,85	58,81	8,027	28,334	2,7304*10 <sup>-9</sup>	2367,3
S <sub>D</sub> <sup>2</sup>	2,676	0,50543	2,396	0,47201	0,33856	0,42098	2218894	1,9451
S <sub>D</sub>	1,6359	0,712094	1,5479	0,68703	0,58186	0,64883	1489,6	1,3947
Σ(Di-Dm)	4,0*10 <sup>-5</sup>	0,41601	-0,19531	0,4012	0,03801	7,79*10 <sup>5</sup>	-263,05	0,001223
Σ(Di-Dm) <sup>2</sup>	141,83	26,791	146,15	28,795	6,0942	7,5777	7,701*10 <sup>-9</sup>	2367,2
Σ(Di*Ti)	2,348	87,549	2,5594	99,926	0,21403	50,374	4998194	1736,4
ΣTi	1,166	-105,74	1,3278	-122,62	0,263	-43,244	1240,2	-1933,2
mean T	0,021593	-1,9951	0,021415	-1,9777	0,013842	-2,276	1,4287	-1,5872
ΣTi <sup>2</sup>	0,074	222,11	0,082928	260,91	0,012499	105,22	194917	4757,5
S <sub>T</sub> <sup>2</sup>	9,21*10 <sup>-4</sup>	0,28407	8,93*10 <sup>-4</sup>	0,31066	4,92*10 <sup>-4</sup>	0,37772	158,12	1,3879
S <sub>T</sub>	0,03035	0,53299	0,02989	0,54924	0,022184	0,61459	12,575	1,1781
Σ(Ti-Tm)	0,142	1,2363	0,16116	1,2529	2,0*10 <sup>-6</sup>	5,77*10 <sup>5</sup>	0,001077	-0,01265
Σ(Ti-Tm) <sup>2</sup>	0,4969	15,084	0,0549	18,428	0,008859	6,799	192431	1689,1
Σ(Ti-Tm)(Di-Dm)	1,508	12,551	1,64	14,614	0,13014	5,1752	4724746	1722,6
S <sub>xy</sub>	0,2879	0,20993	0,027136	0,2356	0,0072301	0,28751	3882,3	1,4154
r <sub>xy</sub>	0,568	0,62434	0,5789	0,63444	0,56012	0,72099	0,20727	0,86146
t <sub>r</sub>	6,23	5,7635	5,5	8,2491	2,788	4,29	7,388	59,153
t*	2,669	2,669	2,669	2,660	2,539	2,861	2,576	2,576
b	0,0105	0,46806	0,0112	0,50719	0,021355	0,68294	0,00175	0,7277
c	0,014	-1,584	0,0137	-1,6248	0,007031	-1,5622	1,1538	-1,586
t <sub>b</sub>	5,025	5,695	5,544	6,4641	2,8686	4,4144	7,39	59,18
t*	2,669	2,669	2,669	2,660	2,861	2,861	2,576	2,576
R <sup>2</sup> (%)	32,3	39,00	33,5	40,2	31,4	52	4,3	74,2



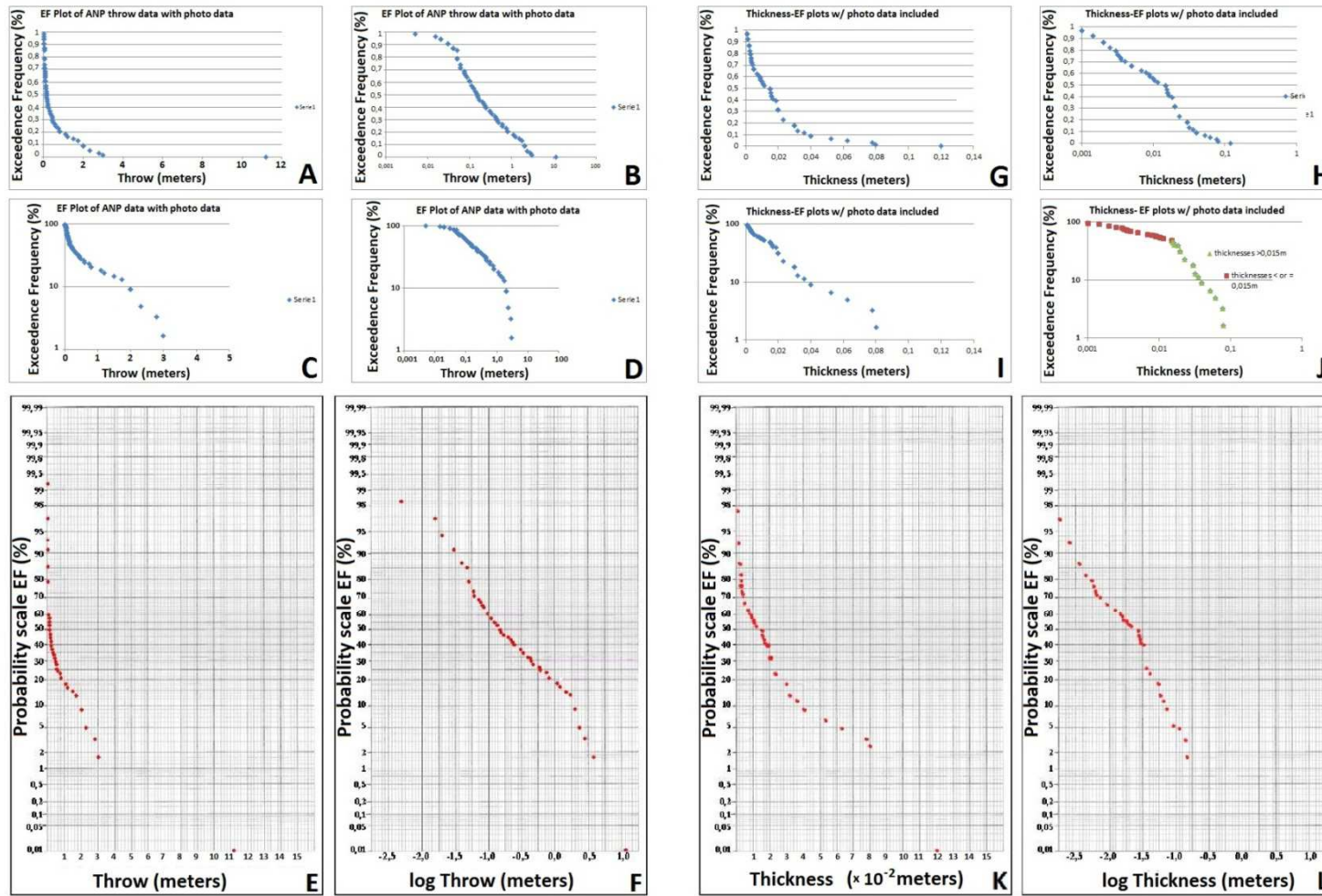
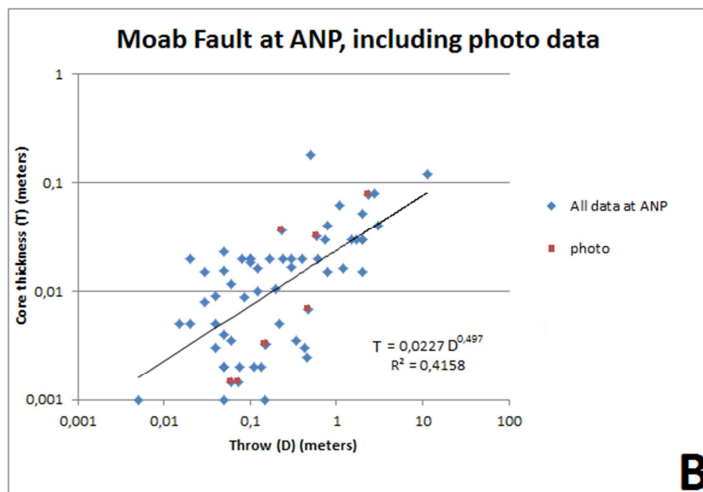
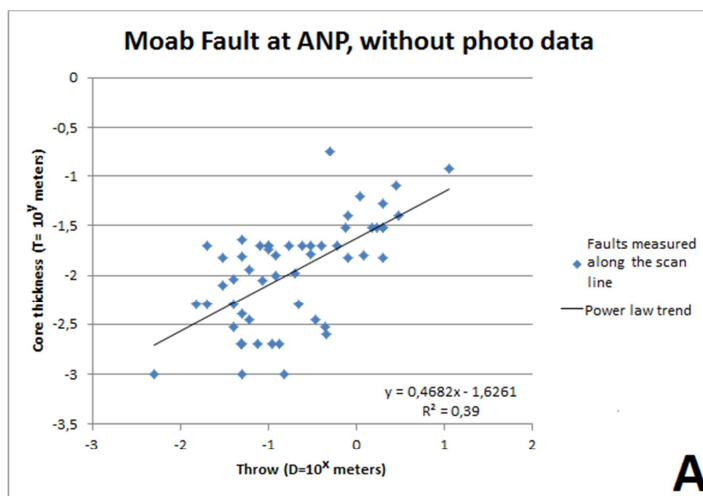


Figure 3-4: EF plots for throw (A-F) and thickness (G-L) of the data for the Moab Fault site at ANP, which includes photographic estimations (see table 2-5). See figures 2-2 or figure 2-3 for an explanation of the plots for throw or thickness, respectively. Overall analysis shows strong arguments for logarithmic distributions of throw and thickness, and distributions following a power law pattern (see text for details). Data for the EF-throw plots comes from Table A2-2, columns 3 and 5. Data for EF-thickness comes from Table A2-2 columns 6 and 8.

### Plot of thickness (T) to throw (D)

The plot of thickness to throw for the scan line data of the Moab Fault at ANP is shown in Figure 3-5A, based on the data observed in table 3-1A and the calculations in the second column of Table 3-2. The plot has axes with logarithmic scales. Plots showing fault thickness and displacement have previously been plotted with thickness on the X axis (e.g. Torabi & Berg, 2011; Knott et al., 1996; Di Toro & Pennacchioni, 2005; Van der Zee et al., 2008). Fault thickness is likely affected by displacement (Childs et al, 2009; Wibberley et al., 2008), and displacement is easier to measure in the field than thickness of the fault core. For these reasons, throw is represented on the x axis, and thickness is represented on the Y-axis in this project. The throw range covers 4 orders of magnitude, from 0,005m to 11,2m. Despite this range, there is no throw value between 2,8m and 11,2m, a



**Figure 3-5: Plots of thickness versus displacement for the faults at ANP.** Figure 3-4A shows the data obtained from the scan line. Figure 3-4B shows all data, including data estimated from photographs (brown squares). While results of the plots are comparable to one another, the trends represent a regression caused by too few data points over a small range covering four orders of magnitude.

distance equal to 75 percent of the total linear range of throw.

Thickness readings are spread over three orders of magnitude, from 0,001m up to 0,18m, but there are only two thickness readings greater than 0,085m. Assuming power law distribution (Bastesen et al., 2012 (in print); Kolyukhin & Torabi, 2012)

gives a relationship for thickness (T) to throw (D) of  $T = 0,0237D^{0,468}$ , and a goodness of fit regression of 39,0% (Table 3-2, second column). The plot shows an overall power-law trend with a weak correlation and scatter spread across the trend line of at least 1,5 orders of magnitude (A linear trend was calculated and the results can be reviewed in table 3-1A).

When the photographically derived fault readings are included with the data (Table 3-1, fourth column), the results form a similar

Likelihood of regression change-points and predicted values, for data from the ANP scan line.

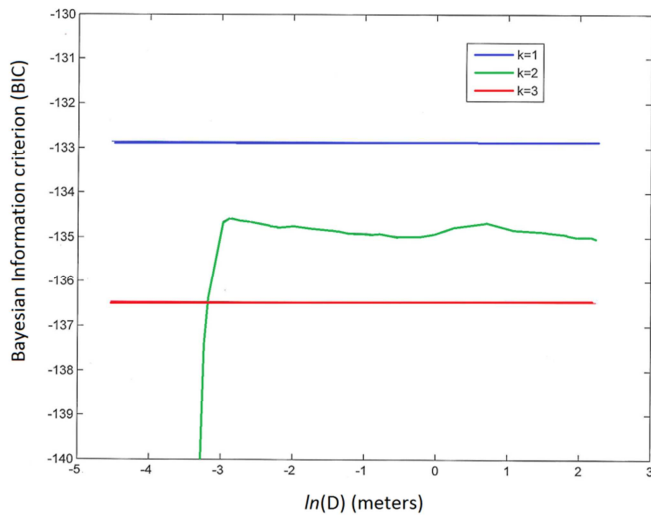


**Figure 3-6: The Bayesian Information Criterion.** The probability of any value representing a change-point for a power law regression, analyzed for three models (K). K=1 represents one slope with no change points. K=2 represents the shows the likelihood (L) of a regression trend having two segments, and the probability of a change point occurring at a given throw value (D). K=3 shows the likelihood of a regression trend having three segments, and the probability of a change point occurring at a given throw.

thickness and displacement. Several articles, (e.g Torabi & Berg, 2011; Shipton et al., 2006) state that the relationship between thickness and displacement cannot be described by a simple power law relationship. A summary of the analysis is described below.

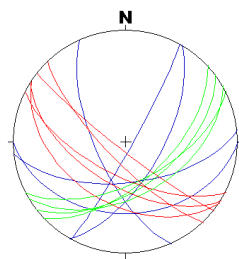
The throw and thickness data are used as inputs and the regression is analyzed using a piecewise linear function in logarithmic scale. The BIC analysis determines change points of the regression trend and the slope of the sections on either side of the change point. The BIC selects the best model from a finite set of models. Regression is performed by maximal likelihood estimation technique (Kolyukhin & Torabi, 2012).

The assumptions that the residuals are independent and normally distributed were tested using the Durbin- Watson, Jarque- Bera and Liliefors tests, at 5% significance level. Regression is tested using an F test (Kolyukhin & Torabi, 2012).

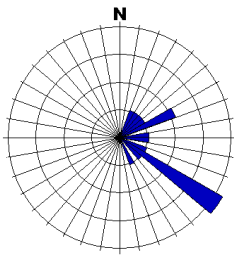
The BIC analysis is designed for analyzing power law trends, such as the expected trend between thickness and displacement. In the analysis, k represents the order number of models used to analyze the data. For the data presented from the ANP site, there were three models: k=1 for one slope regression, k=2 for two slopes, one change point, and k=3 for three slopes, separated by two change points. Figure 3-6 shows a plot with three curves. The X axis represents the natural log of the displacement value in meters. The Y axis represents the likelihood strength of any displacement

scatter plot. The power law exponent increases from 0,47 to approximately 0,50. Regression goodness of fit that is slightly higher (41,6%).

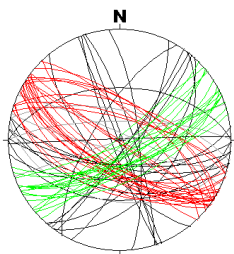
The change in the trend for the thicknesses observed for in the EF plots suggested further investigation into the relationship between thickness and displacement at ANP. The data was tested by the statistical approach used by Kolyukhin & Torabi, 2012. This approach utilizes the Bayesian Information Criterion (BIC), discussed in detail in Kolyukhin & Torabi, 2012. The purpose of the analysis was to determine if there is a change in the power-law relationship between



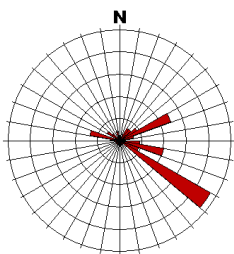
*San Rafael Swell faults, great circles*



*San Rafael Swell faults strike distribution*



*San Rafael Swell fractures great circles*



*San Rafael Swell fractures strike distribution*

**Figure 3-7: The Schmidt Net and Rose diagram for Tidwell Draw faults and fractures.** While there is a generally NW-SE trend, there are also weaker trends NE-SW. All faults observed had a strike on the eastern half of the diagram, as did most of the fractures. In the rose diagrams, each ring represents 5% of the total population, each wedge represents 10 degrees.

value to be a change-point for the power law regression. Each curve represents one of the models tested for the data at ANP without photographic data. The blue line represents the constant BIC value related to the model with one slope without any change point. The green line representing the model with two slopes, one (change-point) rises up at  $\ln(-3)$  on the x axis, then trails to the right of the graph. This line shows the dependence of the BIC value on change-point position. The red line presents the maximal BIC value for the model with three slopes (two change-points).  $K=1$  (blue curve) has the highest BIC value, indicating that the most suitable statistical approximation is with only one slope, and no change point in this range of this data from ANP. Although the green curve shows some indication, there is neither, a clear spike, or any value above -133, the value for one slope. The graph indicates that the program found no statistically significant change in regression, and there is a higher BIC value for one regression line for the data at ANP than that there are piecewise linear function with two or three slopes in logarithmic scale. This result may have been affected by insufficient data, inaccurate logging of data, characteristics of the Moab Fault, or a range of data that was too narrow to detect a change in the trend.

### 3.2. San Rafael Swell at Tidwell Draw

#### 3.2.1. Structural Characteristics at Tidwell Draw

At Tidwell Draw, 23 faults and 85 fractures were logged along the scan lines and are plotted in their respective stereo-plots (Figure 3-7). The faults and fractures, arranged into their respective rose diagrams indicate a more scattered pattern of strike distribution. Whereas the overall pattern at ANP showed a dominating SE-NW pattern, the pattern at Tidwell Draw shows a more easterly shift in overall strike. The majority of structures trend SE-NW, but a larger percent of fractures and faults strike NE, indicating a more scattered, easterly mean strike than for the discontinuity structures at ANP. If the thrust that formed the San Rafael Swell during the Laramide tectonic event was in a northerly direction, the stretching and extension of the surface to accommodate the increased surface area created by the swell

may have resulted in oblique faulting, trending approximately 60 degrees from the stresses of the orogeny (Agosta & Aydin, 2006). The more pronounced SE trend may have been influenced by stresses occurring in the adjacent Paradox Basin, though research is needed to confirm this hypothesis.

### 3.2.2 Results of statistical analysis of Tidwell Draw data

#### *Univariate analysis and EF plots*

EF plots were made for throw and fault thickness from 21 faults measured along scan lines at Tidwell Draw in San Rafael Swell, central Utah (Table 3-1B) (see Figure 3-8). No attempt was made to estimate any fault throws or thicknesses from photographs of the outcrop at Tidwell Draw. Outcrops in this area were easily reached such that all faults could be reached from near the base of the outcrops. In the EF-throw plot (Figure 3-8A) the plot initially has a steep angle, but between EF=30% to EF=20%, the plot follows a tight curve radius, then decreases following a shallow angle, forming an approximately hyperbolic shaped, concave-up pattern. In the EF- log throw plot (Figure 3-8B) the curve decreases following a pattern that overall appears concave-up, but with a concave down curve at either end of the plot. Although the plot is not straight, the overall pattern could be interpreted as following a straight pattern. In the plot of log EF- linear scale throw (Figure 3-8C) a concave up curve that begins steep but has a relatively shallow trend from approximately 0,25m throw is formed by all of the points in the plot except the point (0%-1,90m). The log EF- log throw plot (Figure 3-8D) appears to form a sinuous trend that declines at a low but varying angle. The overall trend is nearly linear except for the last point (0,0%, 1,90m). The trend can be compared in shape to the trend in figure 3-8B, except that the trend in Figure 3-8D is less sinuous and more straight than the trend seen in Figure 3-8B. In the probability scale EF-throw plot (Figure 3-8E) the plot appears to form a trend of two curves which meet at 0,0165m, 22%. The curve representing 0-0,165m is steep and concave up, whereas the curve representing throws greater than 0,0165m appears concave down, with a relatively shallow trend that increases in slope as the throw increases. The slope does not become as steep at throw>0,165m as it is in the plot of throw<0,165m. In the probability scale EF- log throw plot (Figure 3-8F), the overall trend appears to be over all slightly concave up, although a linear trend could also be seen in the plot. As with figure 3-8E, when dividing the plot at 0,165m, the portion of the plot <0,165m appears to make a slightly concave up profile, whereas the portion greater than 0,165m tends to form a concave down trend.

The EF- thickness plots also displayed a somewhat discontinuous pattern, where the trend of the lower thickness values ( $\leq 0,02m$ ) do not continue through the higher thickness values. Another observation of these graphs is that the EF- thickness points tend to be scattered relative to EF plots of other data in this report. The plot of EF-thickness, (Figure 3-8G) shows an overall trend forming a



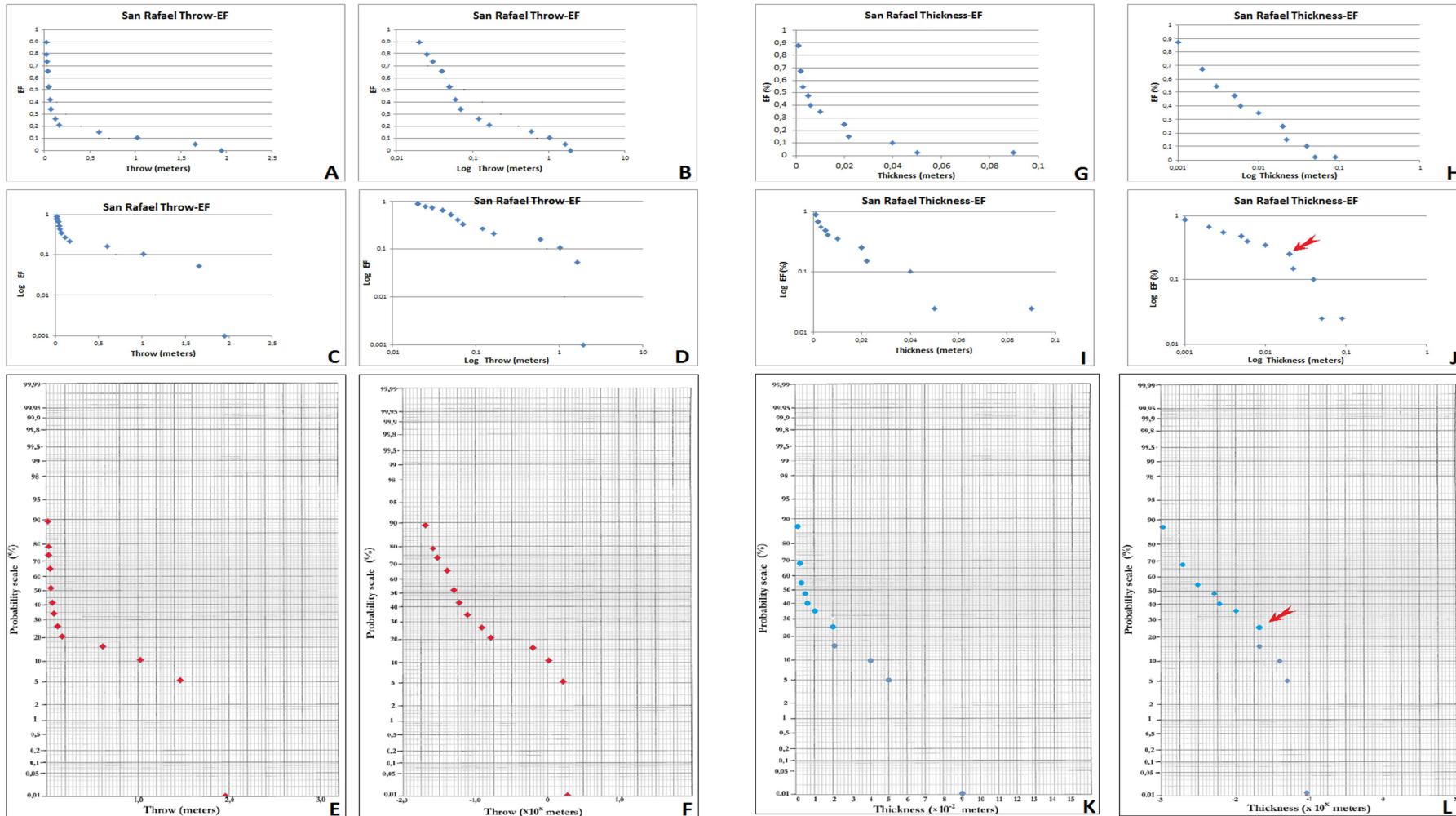


**Figure 3-8** EF plots for throw (A-F) and EF plots for core thickness (G-L) for the Tidwell Draw area at San Rafael Swell. The shapes of the EF-throw plots appear to show two characteristic curves that meet at a common point which forms a discontinuity between two regions. Similarly, there is also an apparent discontinuity in the EF-thickness plots, as indicated by the red arrows. The discontinuity is mentioned, but not investigated due to a lack of data. Data for the EF-throw plots comes from Table A2-3, columns 3 and 5. Data for EF-thickness comes from Table A2-3 columns 6 and 8.

concave up pattern with a wide turn radius. The plot of EF to log thickness (Figure 3-8H) shows a nearly linear overall trend. The plot of log EF to thickness (Figure 3-8I) shows a concave up trend for the points having a thickness less than or equal to 0,02m. Values above 0,02m form a nearly linear pattern slightly steeper than the slope where the plot up to 0,02m thickness ends. For the log EF-log thickness plot (Figure 3-8J), the plot forms two nearly linear trends that intersect at (0,02m, 25%) (Figure 3-8J, red arrow). The overall trend appears to be a concave down trend. In the plot of probability scale EF to linear thickness (Figure 3-8K) the overall plot shows an overall concave up trend, initially declining steeply, then decreasing in slope to approximately 45 degrees. In the plot of probability scale EF to log thickness (Figure 3-8L), the plot is divided into two sections. The data with thicknesses less than or equal to 0,02m forms a slightly concave up trend. Points with thicknesses greater than 0,02m tend to form a trend that is straight or slightly concave down.

#### *Plot of thickness (T) to throw (D)*

The log thickness-log displacement plot (Figure 3-9) appears to show a concave down trend visually. Statistically, the plot best follows a power law curve with the relationship  $T=0,0274D^{0,6829}$ , with a goodness of fit  $R^2$  of 52,0%. Other trendlines have been analyzed as well. A linear trend of  $T=0,0214D+0,007m$  has a goodness of fit  $R^2$  of 31,3%. Although there aren't very many data points on the graph, it is possible to see that scatter of at least a full magnitude for lower values as well as higher values of displacement along the plot. One point (0,165m, 0,02m) is marked in red in figure 2-8. This fault represented both, the observed discontinuity in the EF- throw plots, and the observed discontinuity in the EF-thickness plots. Faults with displacements less than 0,135m show a relatively steep trend with scatter covering approximately 1,5 orders of magnitude. Scatter in thickness. Faults with thicknesses greater than 0,02m show a trend that is not as steep as the overall trend, but also show much scatter (up to one order of magnitude). This gives the pattern formed by the points on the plot the appearance of a concave down crescent that rotates around the fault data with 0,165mD and 0,02mT. The low number of faults plotted from the Tidwell Draw site may not be enough to draw a conclusion regarding trends in EF plots or the plot of thickness to displacement. The low number of faults within a range of three orders of magnitude for throw produced a goodness of fit  $R^2$  value that was higher than one might expect from graphical analysis of the curve. The other results in this project and results from previously published results (i.e. [Shipton et al., 2006](#); [Evans, 1990](#); [Foxford et al., 1998](#)) have shown that thickness has a weak correlation with displacement in log-log plots. Although an  $R^2$  value of 51% does not represent a strong correlation, it is stronger than correlations found in the other analyses included in this chapter. The twelve faults with the lowest thickness values are more closely spaced than are the other faults. Numerical leverage from the four faults with the greatest displacement values strongly influence the over-all regression of the trend ([Torabi & Berg, 2011](#); [Moore and McCabe, 2006](#)), which may artificially affect

the overall goodness of fit. Better results and a clearer understanding of the relationship between fault throw and fault core thickness would likely result from more plotted data (Moore & McCabe, 2006).

### **3.3. Combined results for thickness to throw relationships**

The data from the faults at Tidwell Draw are combined with the fault in this section data from ANP. Figure 3-10 is a plot of the combined data. The range of the data covers four orders of magnitude for displacement, and three orders of magnitude for thickness. For a power law relationship of  $T=0,0231 * D^{0,545}$ , the goodness of fit regression is 45,5%

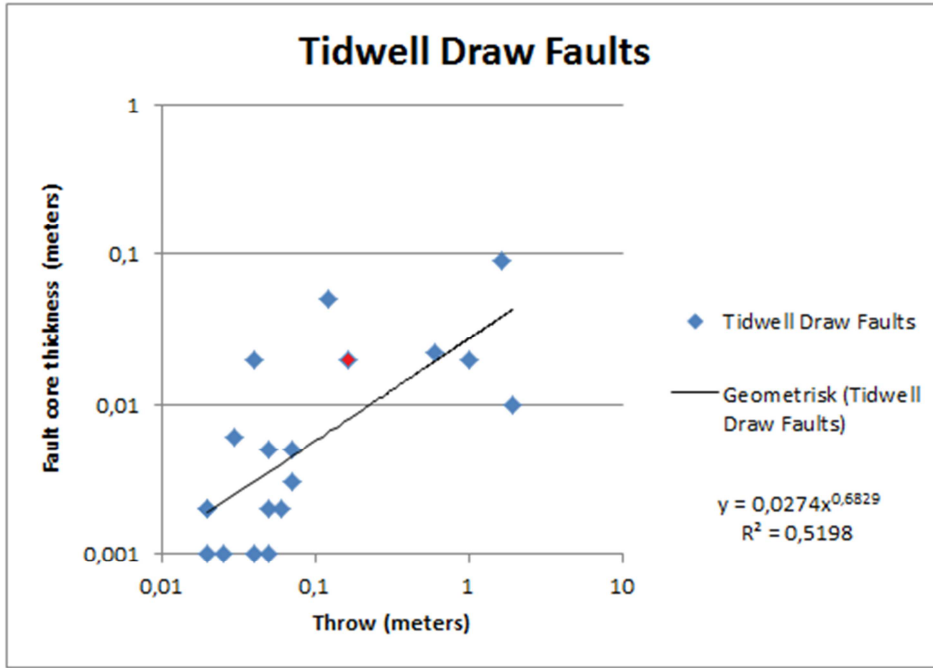


Figure 3-9: The plot of thickness to throw for faults at Tidwell Draw in San Rafael Swell. The red mark represents the fault with 0,165m throw and 0,02m thickness. These values are the locations on the EF plots where a possible change in slope occurs for the respective EF plots. The low regression is likely the result of low data count covering a small range of three orders of magnitude for displacement.

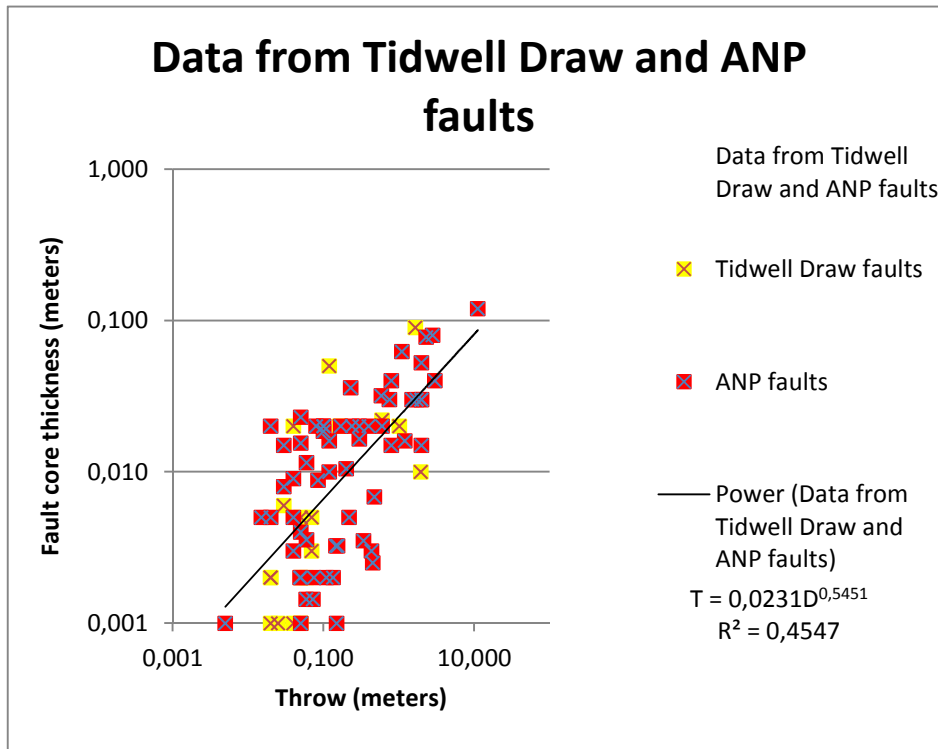


Figure 3-10: A plot of the data combined from the site at ANP and the site at Tidwell Draw.

# 4 Discussion

---

## 4.1 Interpretation of the results

Since faults tend to form in groups and influence the behavior of the rock masses in which these faults form, studying the distribution of faults in a region may improve our understanding of those rock properties (Clark et al., 1999). By understanding the distribution of faults and fractures, reservoir modellers can predict subseismic fault and fracture characteristics around a seismically resolved structure, aiding in understanding of a caprock and reservoir quality (Bonnet et al., 2001).

Power law distributions in univariate plots can be difficult to determine with certainty (Sornette, 2007; Clauset et al., 2007). It may be easier to prove that a power law distribution is plausible, and then rule out competing hypotheses (Clauset et al., 2007). One of the more common ways to determine the distribution of a variable is by creating a cumulative density plot, then observing the plot in log-x, log-y scale. A straight line is generally seen as an indication of a power law trend in the distribution curve. However, there are several problems with this approach. Insufficient sampling or finite-size effects may cause the data at one or both ends of a trend to deviate from the power law trend, forming a “tail” (Sornette, 2007). Errors are hard to estimate because they are not well supported by standard regression formulas. Large variances in the data are covered up by the log-log scale, which can lead to a higher, misleading goodness of fit  $R^2$  value (Clauset et al., 2007).

At ANP, the EF plots for both, the throw and thickness appear to have characteristics similar to log-normal distributions and power law distributions. Upon closer visual inspection, the throw data follows a power law trend, with the last few data forming a tail due to insufficient data or truncation (Torabi & Berg, 2011; Sornette, 2007). Fault core thickness forms an over-all logarithmic distribution pattern that is the result of two segments that appear to follow different power-law trends. A description of this type of distribution is found in Fellitti & Bersezio, 2009, in which turbidite beds are observed to follow one power law distribution until at a threshold bed thickness, the larger beds are distributed according to a power law trend with a steeper (greater) exponent. A similar shift in distribution trend may signal a change in the behavior of the faults that affects the distribution of the greater thicknesses, occurring at approximately 0,015m (Torabi & Berg, 2011). According to Bastesen et al., 2012 (in print), the relationship of throw to thickness for faults under 10m is approximately 30 to 60/1. This suggests that 0,015m thickness could correspond to approximately 1,0 meters displacement. Torabi & Berg, 2011 suggests that the power law relationship is higher for medium faults than for smaller faults, with the change-point of this increase occurring at approximately 1m displacement.



The fault throw and core thickness data from ANP was analyzed following the procedures described by [Kolyukhin & Torabi \(2012\)](#) to try to confirm the hypothesis of a change in power law relationship at one meter of displacement, as suggested by [Torabi & Berg \(2011\)](#) and demonstrated by [Kolyukhin & Torabi \(2012\)](#). Unfortunately, the analysis using the BIC method came up inconclusive for the data from ANP, likely owing to a lack of sufficient data for proper analysis.

The plot of thickness to throw at ANP (Figure 3-5) shows a weak power law relationship between fault core thickness and fault throw, based on the analysis summarized in column 4 of Table 3-3. The linear relationship, found in column 3 of the same table, shows a weaker correlation. Figure 3-5 and the results in column 4 of table 3-3 seem to verify the statement by [Evans \(1990\)](#) and echoed by others (e.g. [Foxford et al., 1998](#); [Shipton et al., 2006](#)) that there may not be any meaningful or useful correlation between fault core thickness and displacement. However, the likely reason for the poor goodness of fit regression at ANP is that the data is insufficient and covers too little a range to display a true regression or goodness of fit. More data, spread across a wider range would likely produce a more precise result.

The data from Tidwell Draw also shows a weak power law correlation. The data for the Tidwell Draw site is sparse, therefore it is difficult to say with accuracy whether the thicknesses of the faults at Tidwell Draw are dependent on the amount of displacement. It is likely that the regression would improve with more data and faults covering a broader range of magnitudes for both, thickness and throw.

Combining the data from Tidwell Draw and ANP did not extend the range for displacement. When the two data sets were combined (Figure 3-10) the trend on the plot appears to follow the trend line, but the low range of displacement and the fact that scatter covers at least one full magnitude causes the regression to appear low.

## **4.2 Comparison with previously published results.**

### **4.2.1 Univariate statistics**

Different findings on the relationship between fault core thickness and displacement have been reported. Linear relationships were reported in several articles (e.g. [Hull, 1988](#); [Evans, 1990](#); and [Sperrevik et al., 2002](#)). Power law relationships are reported by [Bastesen et al, 2012 \(in print\)](#), [Knott et al., 1996](#)) and are assumed in the analysis conducted by [Kolyukhin & Torabi, 2012](#).

A collection of data related to published articles is compiled to compare the results of Moab Fault with other siliciclastic fault core thickness to displacement data. This data is included in Table A2-1 through A2-9 of the appendix. In the set of published data, faults from siliciclastic rocks, crystalline rocks, and carbonates are represented. Crystalline rocks are typically represented by solid colored dashes, whereas siliciclastic rocks may be represented with diamonds, stars, X's, squares, or

triangles. The source of each data set is represented by a color, so that it is easier to keep track of the data on the plots. Furthermore, the same symbols and color schemes are used on all data sets containing published material, easing comparisons of data from one plot to the next. One exception is that the data obtained from [Foxford et al, \(1998\)](#), represented by green squares in the published data sets, will be represented by blue diamonds when compared with data from ANP. Another exception is all data will be categorically the same color for various comparisons, such as comparison of data from this project with global results, or comparison of crystalline rocks with siliciclastic rocks. Because calculations on table 3-2 differed from automated calculations on Microsoft Excel data processing program by less than two percent, calculations of data in the discussion will be automated by Microsoft Excel, unless otherwise stated.

Much of the fault displacement data at first appears to be distributed following a power law trend (Figure 4-1). The upper image in Figure 4-1 displays the cumulative density plot of the displacement data on a log-log plot. The tails of many of the samples show the straight trend indicative of a power law relationship. The form of the trends tend to take an over-all concave down shape, similar to trends for log-normal, exponential and normal trends (See Figure 1-9, fourth row illustrations). The distributions were therefore redrawn in two log scale exceedence frequency plots showing displacement in linear scale (Figure 4-1, the two lower images). In a linear scale-x/ log scale-y plot a exponential distribution will form a straight trend overall, while the normal trend will form a concave down curve. Log-normal and power law distributions will form concave up trends, but the power law curve will remain closer to the y axis until a lower percentage is reached. At this lower percentage, the power law trend will form a tight concave up curve as subsequent data attains greater displacement (see Figure 1-9).

A more definitive result could be obtained from analyzing a probability scale exceedence frequency to log-scale displacement. A straight line in this plot could reveal log-normal distributions, whereas concave-up trends could be used to separate the data which follows a power law distribution. The probability scale EF plot of log displacement for the published data (Figure 4-2) shows that much of the data tends to form an overall straight trend. This result was unexpected and suggests that perhaps what is often referred to as a power law distribution of fault displacements may more closely follow a log-normal distribution model.

The findings in this report do not support a power law distribution of thicknesses for previously published data sets. Figure 4-3 is a scatterplot in log-log scale, displaying generally concave down trends. An argument can be made that the tails of these trends are relatively straight, indicating potential power law trend. Figure 4-4, is a pair of scatterplots showing EF in log scale, while thickness is represented in different ranges of linear scale. On the upper scatter-plot the scale ranges from 0 to 20 meters and shows the trends with a higher log-normal range departing from the

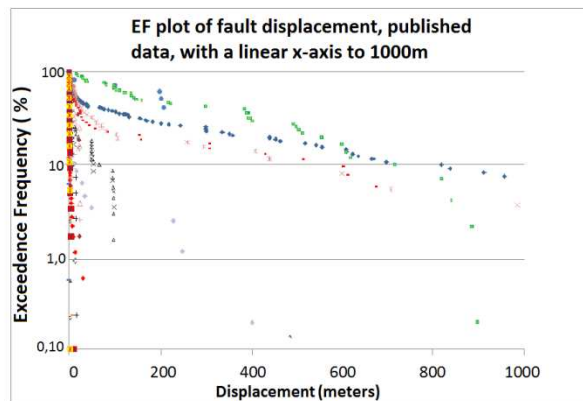
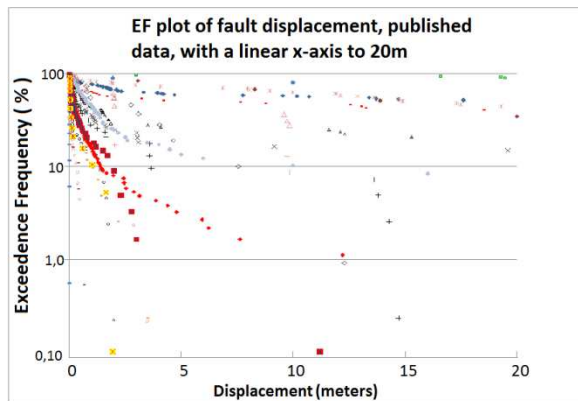
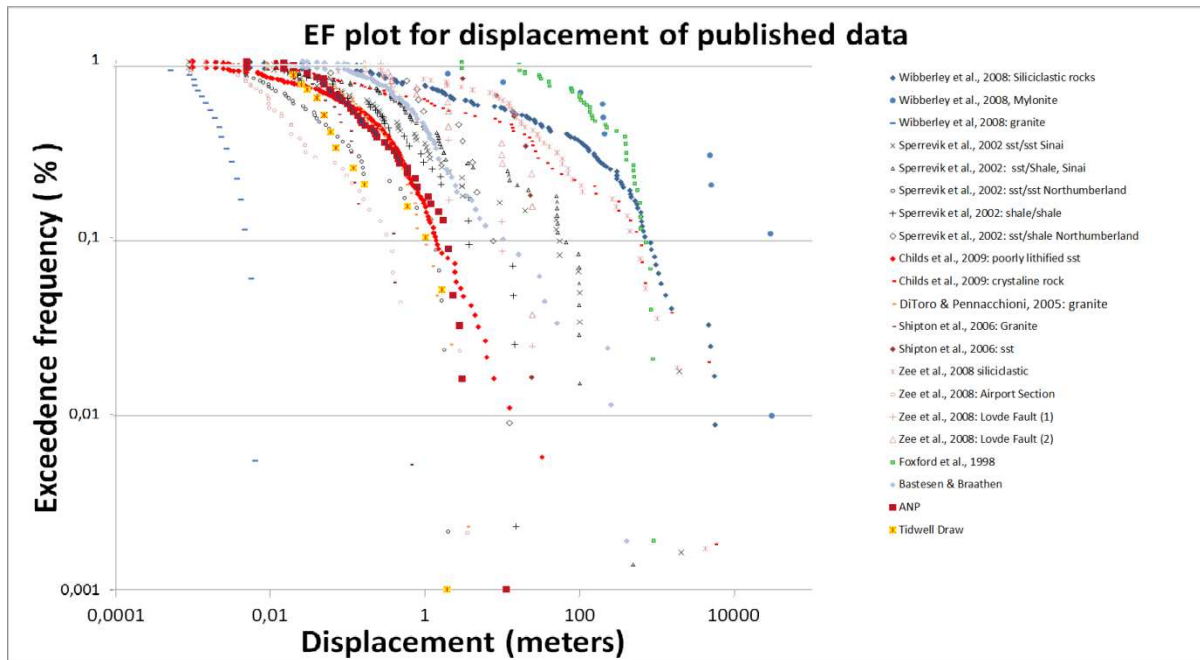


**Figure 4-1 (\*): Top- Log displacement, log EF plot of faults from previously published articles.** Although many of the trends display a convex up curve, the right side of the curves appear straight, leading to interpretations of power law distributions. From this image, it is difficult to conclude power law. The over-all trends of these curves also could be interpreted as normally distributed, log-normally distributed, or exponentially distributed. To make a more accurate assessment, it is necessary to look at other EF plots. In the lower left image, the cumulative frequency axis remains in log scale, while the displacement axis is in linear scale. This image shows that many of the trends depart from the cumulative frequency axis with a concave up trend, ruling out normal distribution and log-normal distribution. The image on the lower right displays the displacement axis in linear scale up to 1000m. In this plot, the trends having more gently sloping trends show a concave up curve at this scale. See text for details.

y axis at high EF values. Although there are trends which do not depart from the y-axis, they do not display the tight concave up curve in the trend, which could suggest a power law relationship. In the lower scatterplot in Figure 4-4, the linear thickness scale is reduced to 0,40m to investigate those trends that have low displacements in the entire data set. These trends tend to exhibit log-normal distribution characteristics, though these graphs are not considered conclusive. Figure 4-5 shows a probability scale EF plot for log scale thickness of the published data. The majority of the data plots

## Probability scale EF / logarithmic scale fault displacement for published data

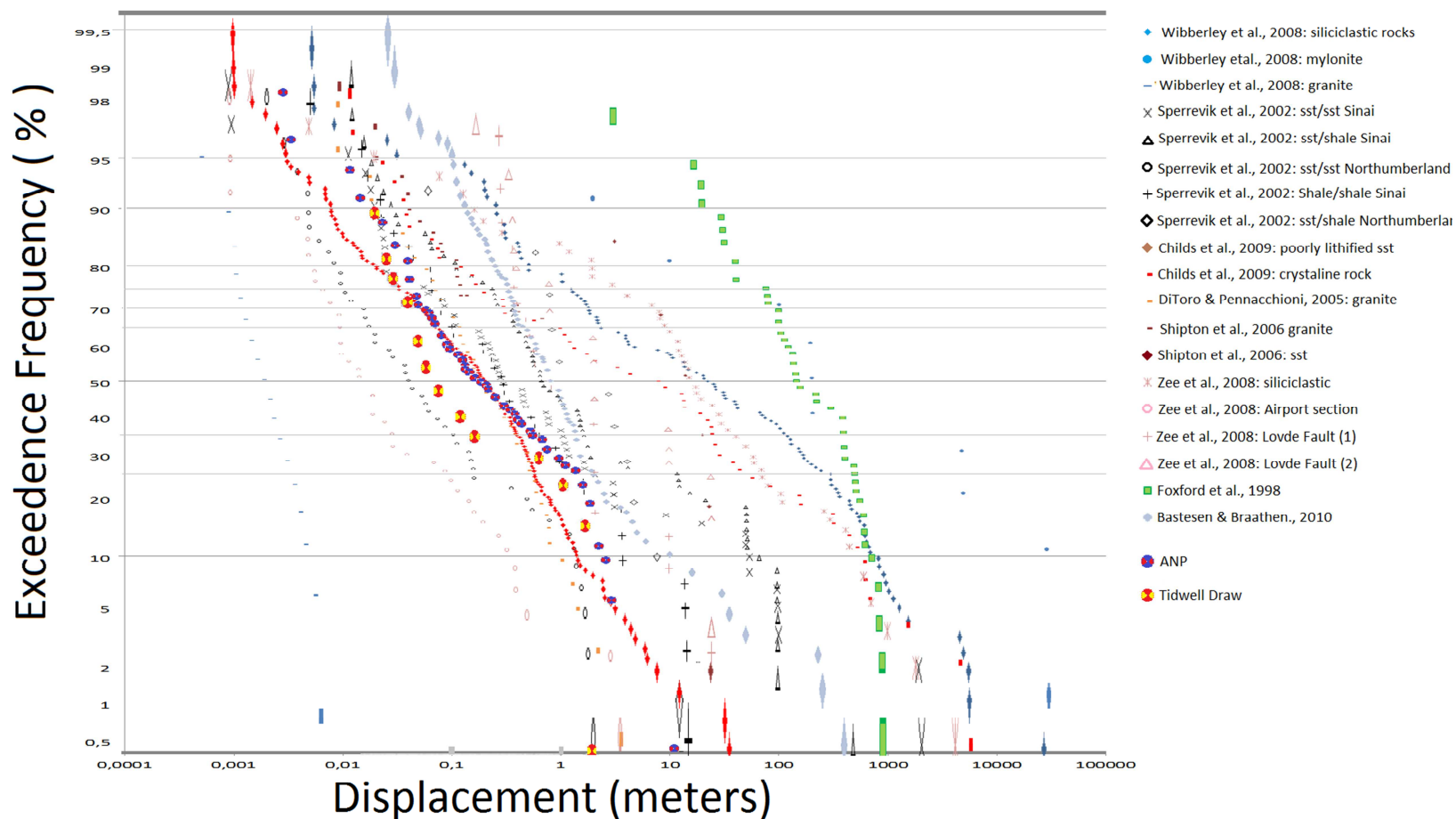
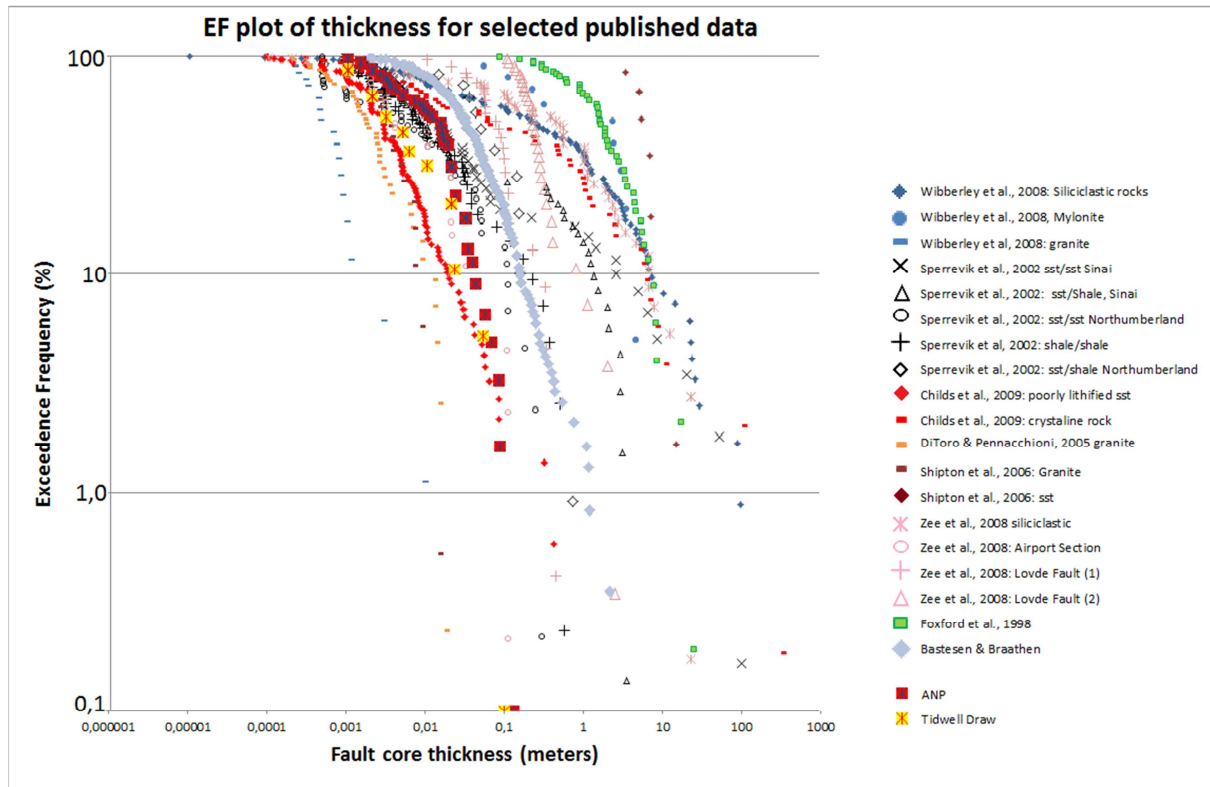


Figure 4-2 : Probability scale EF/ log scale displacement plot for published data. Many of the trends are straight overall. Some trends exhibiting slight concave up curvature, such as Wibberley et al., 2008: siliciclastic rocks (darker blue diamonds) tend to follow it trend with a convex curvature for at least half of the data.

in overall straight lines indicating a log-normal distribution. Published thickness data used in this study tends to follow a lognormal distribution. Power law distribution, though widely used in analyses, especially for fault length distribution, is not always applicable, and other distributions, such as exponential and logarithmic models have been used to describe fault attributes (Bonnet et al., 2001; Soliva & Schultz, 2008; Ackermann et al., 2001). In addition, complex, hybrid distributions also exist which combine the effects of power law and exponential distributions, as well as log-normal and power law distributions (Bonnet et al., 2001; Sornette 2007). Power laws do not have length scales, but in nature, there are upper and lower limits of applicability for power laws (Clauset et al., 2007; Bonnet et al., 2001). These limits can cause distributions to resemble exponential or logarithmic models. Truncation, the under-sampling of data near the limits of the range measured, may also lead to distribution models that don't appear to be power law distribution (Bonnet, 2001). Measurement procedures and sampling bias play an important role in masking power law distribution (Torabi & Berg, 2011; Bonnet et al., 2001), as do geological factors such as competent layering (Gross et al., 1997; Berg & Skar, 2005). Fault linkage may also influence the distribution of fault attributes (Ackermann et al., 2001; Soliva & Schultz, 2008). Such factors may cause a power law distribution to veer from a characteristic straight line in log-log scale exceedence frequency plots.

A straight line in another scale EF plot is difficult to ignore. The probability that censoring,



**Figure 4-3:** Exceedence frequency plot of fault core thickness, with both axes in log scale. As with displacement, these trends display convex up curves. Steep, relatively straight right sides of these trends could suggest a possible power law distribution.



truncation, or a shift in the power law exponent could cause a trend to be perfectly straight in another graphical format cannot be high. A straight line indicates a distribution type, and more often, nature will stray from a straight line, rather than into one. Therefore when a straight line representing a log-normal distribution occurs in a probability scale EF to log scale attribute, it is difficult to reason that frequency distribution can follow power law trends. Power law distributions do occur in nature, and they may even occur in fault attributes. They may even occur on small scales within a larger framework. The trends in this study do not follow a power law model on a larger scale. Within some of the trends (i.e. Figure 4-2: Zee et al., 2008- Airport road; Sperrevik et al., 2002- Northumberland; Foxford et al., 1998), there are small sections that could indicate power law trends within certain ranges, but the overall trend supports a log-normal distribution.

Do the fault thicknesses and displacements at ANP and at Tidwell Draw follow any distribution model other than power law, or can they be interpreted otherwise? There is a strong case that the throw data from ANP could be represented by a lognormal distribution, and it really cannot be ruled out conclusively from graphic interpretation. The interpretation of the log-log plot (Figure 3-3D) and the probability EF- log throw plot (figure 3-3F) are not easily made. These two plots suggest that the distribution could either follow a log-normal model, a power law model or a hybrid distribution combining the effects of these two distribution patterns, as described by Sornette, 2007. For thickness at ANP, the overall trend appears to follow a log-normal distribution model, although the tail section of the trend is straight in the log-log EF plot, involving nearly half of the data. Data following a log-normal distribution with a large variance can mimic a power law distribution in a log-log plot over several orders of magnitude (Felletti & Bersezio, 2010; Sornette, 2007).

There is not as much data at Tidwell Draw. The data seems to indicate a break in the trend, but the two segments formed would have too few data to draw an accurate conclusion in either thickness or displacement distribution. The throw data at Tidwell Draw, when interpreted as a set, appears not to follow other distribution patterns and is interpreted as following a power law distribution pattern. Thickness tends to follow a logarithmic distribution pattern when taken as an entire set. This interpretation is seen most clearly in the relatively straight trend formed from the probability scale EF-log scale thickness plot (Figure 3-7L and Figure 4-5, red and yellow balls).

Fault displacement does not appear to follow either power law, logarithmic, or exponential distribution models universally, as reports by Ackermann et al., 2001; Soliva & Schultz, 2008; Bonnet et al., 2001 can attest. Because fault displacement distribution behaves differently in different regions, having the knowledge about what influences the distribution pattern of displacement and fault core thickness could have profound impact on prediction these distributions in areas where such conditions are known to exist. Mechanical layer thickness, degree of extension, and fault

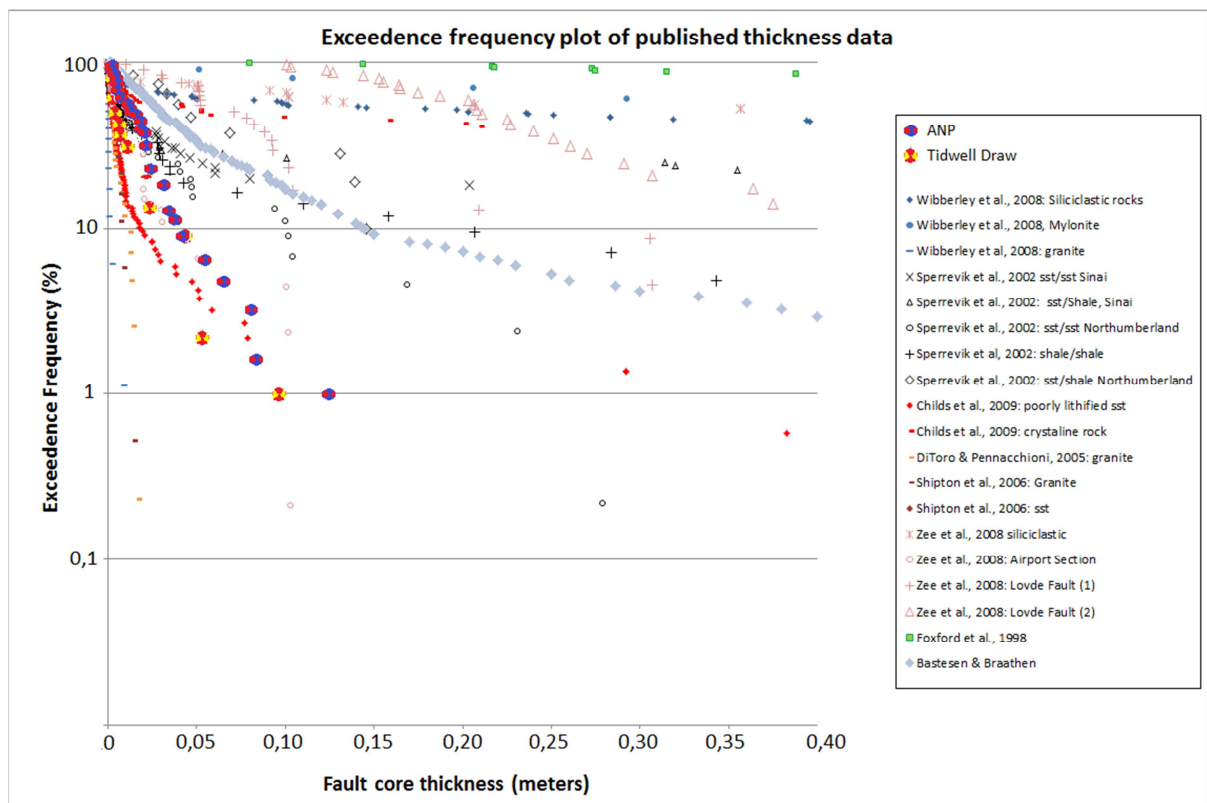
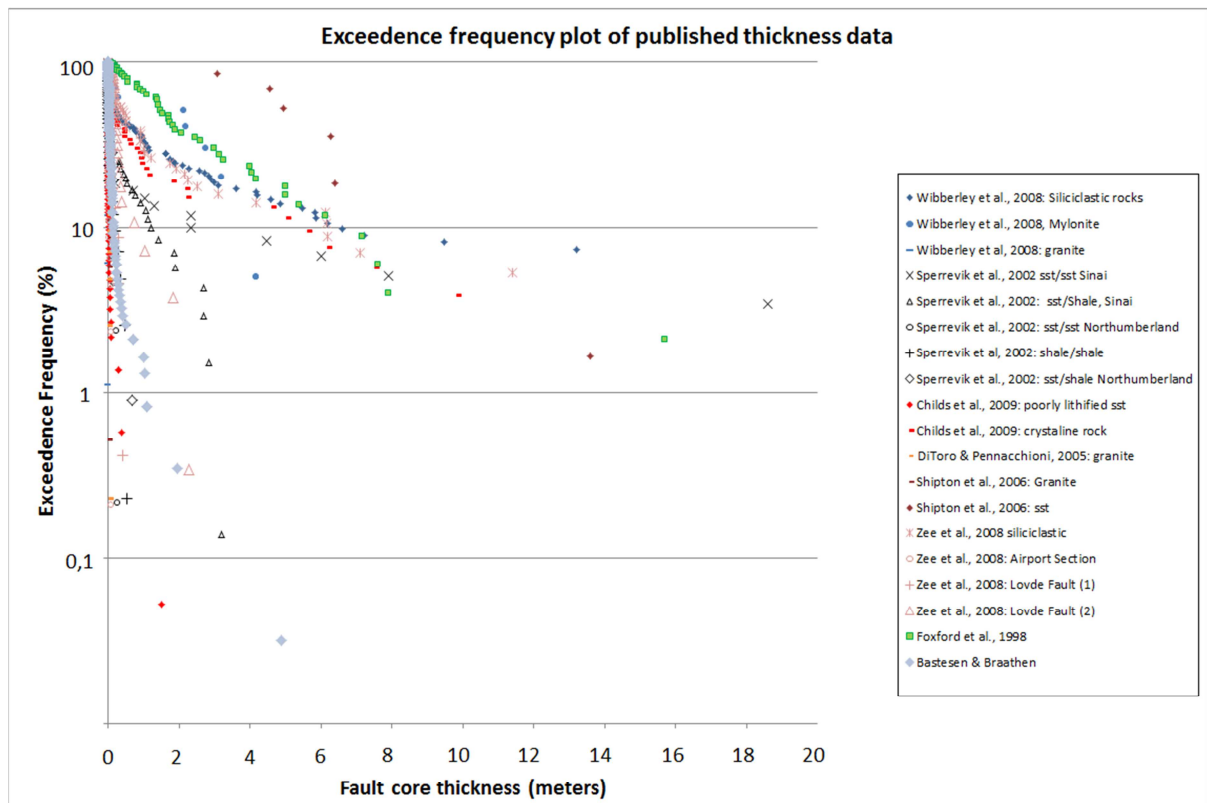


**Figure 4-4: log scale EF to linear scale fault core thickness for some of the previously published data.** The upper image displays thickness to 20 meters and shows trends for the data sets covering thicknesses at the greater magnitude orders covered by the global data set. Data for ANP and Tidwell Draw are not shown in the upper image to avoid overcrowding of data along the 'Y' axis. The thickness axis for the EF plot in the lower image displays a range of 40cm, and shows trends in the lower orders of the range. These two images reveal the trends tend to have gently concaved up characteristics typical of exponential distribution models, and perhaps power law distribution models.

linkage play an important part in the distribution of fault attributes ([Ackermann et al., 2001](#), [Soliva & Schultz, 2008](#) and references therein).

Even a distance as little as 100km apart in the Colorado Plateau, where similar lithostratigraphic sequences exist, fault attribute distribution within damage zones behave differently. Tidwell Draw normal faults probably occurred subsequent the thrusting events that led to the formation of San Rafael Swell ([Johansen & Fossen, 2008](#)). Literature reporting structural geology of the area (faulting, folding or tilting) prior to the formation of the San Rafael Swell has been difficult to find, leading to the assumption that from the time of deposition of the sedimentary layers until the formation of the San Rafael Swell there was little structural activity. This contrasts sharply with the Moab Fault, which formed over pre-existing structures that may have stemmed from the formation of the Uncompahgre uplift and the Paradox Basin. The Moab Fault runs along the northeast side of the Paradox Basin, where orientation of each subsequent structure was influence by the pre-existing structures in a chain of events that led to the formation of the Moab Fault. The chain of events, starting with the Uncompahgre Uplift, which led to deep salt deposits of the Paradox Formation ([Trudgill, 2010](#); [Barbeau, 2003](#)) influenced the alignment an orientation of succeeding structures. Differential loading from the Uncompahgre sediments, followed by salt migration to form the salt anticlines along preexisting faults in the Triassic ([Baars & Doelling, 1987](#)), and finally normal faulting, all trend NW-SE. This may help to explain why the orientations of the faults and fractures at ANP tend be less scattered than those structures at ANP, as can be seen by comparing Figures 3-1 and 3-6. The differences in structural histories may be worth investigating to see if a reason may be established for the log-normal distribution of fault displacement frequencies at ANP and the power-law distribution pattern observed in the displacements of the faults at Tidwell Draw.

More recently, the concept of several power law trends may exist at differing scales along a distribution ([Torabi & berg, 2011](#), [Kolyukhin & Torabi, 2012](#)). Fault growth is affected by grain size and thickness of sedimentary rock layers in such a way that changes in the power law distribution of fault throw, thickness and spacing may occur ([Knott et al., 1996](#)). [Shipton et al., 2006](#) suggested that with so many factors causing changes to the scaling relationship between fault displacement and fault core thickness, a single displacement thickness relationship probably isn't enough to properly describe fault zone characteristics. [Torabi and Berg \(2011\)](#) have suggested that the changes in the power law at various points may cause a power law distribution to resemble an exponential or a log-normal distribution.

## Probability scale EF to log thickness values for published fault core thickness data

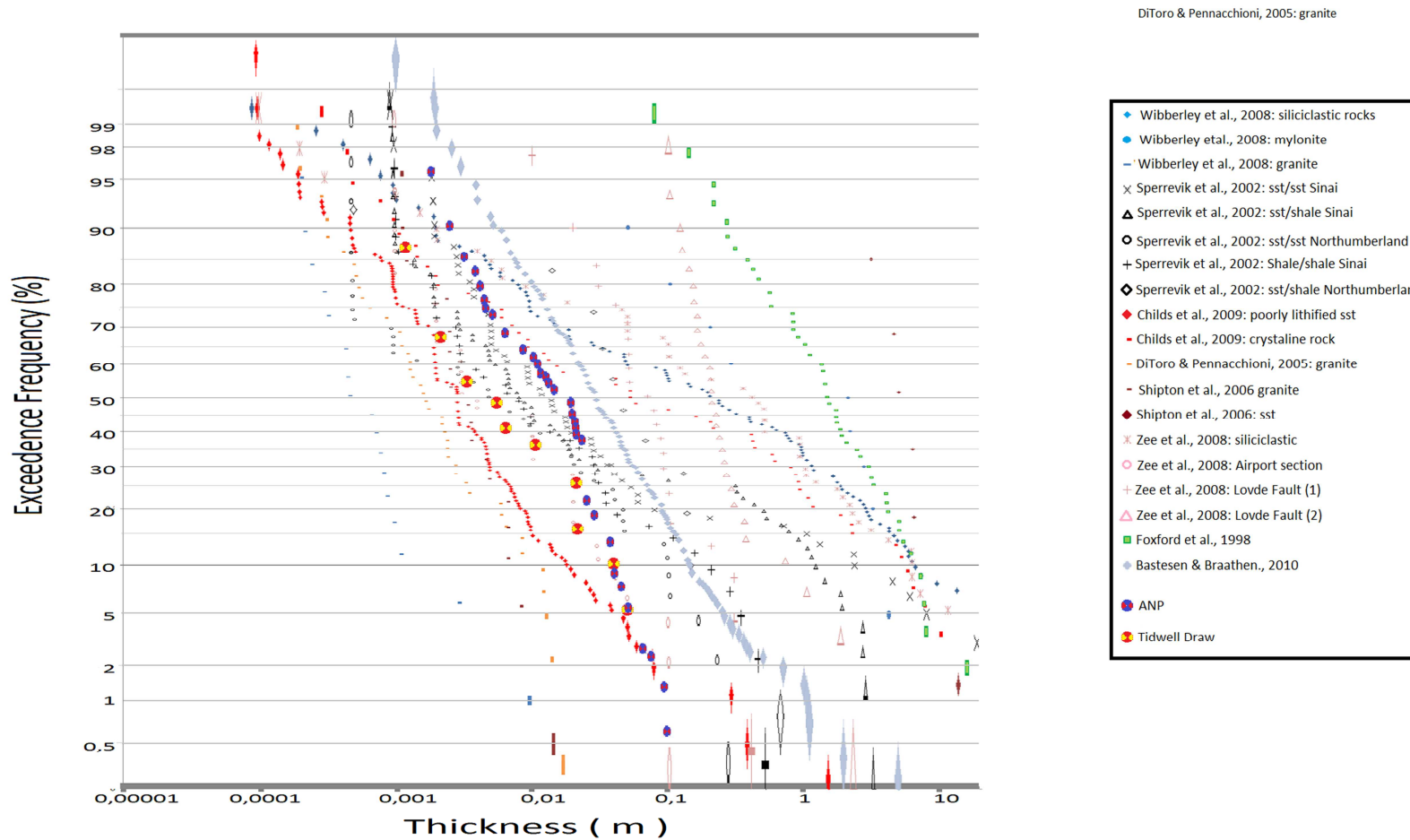


**Figure 4-5:** The probability scale EF/ log scale thickness tends to show overall straight patterns for thickness distribution, suggesting that thickness may follow log-normal distribution distributed.

#### 4.2.2 Fault core thickness versus fault displacement

A global data composite involving many data sets would have several advantages and disadvantages over individual data sets. A composite data set may contain data from different tectonic regimes; different lithospheric components arranged differently, different fault geometries and different measurement biases (Evans, 1990; Shipton et al., 2006). Different tectonic regimes, asymmetrical damage zones, and lithostratigraphic components may affect how energy is spread throughout the fault during slip events, affecting overall displacement (Wibberley et al., 2008). Measurements can vary from different workers as the definitions of fault core thickness and fault displacement may differ, not only from researcher to researcher, but also from region to region. Not all components of a definition may be present in all locations (Shipton et al., 2006; Torabi & Berg, 2011). Different fault systems may have different regression gradients which would not match with one another or be represented by the composite data set (Evans, 1990). Advantages of combining data sets include increasing the range of data by several orders of magnitude. More data and an increase in the range have the effect of reducing the influence of outliers. Regression gradients are also affected by the size of the sample population and the range, with an increase in both of these parameters improving the correlation and regression values (Moore & McCabe, 2006; Torabi & Berg, 2011).

In Figure 4-6 the fault core thicknesses have been plotted for the fault displacements for the selected data sets. The plot displays a best fit regression of 74,2% for a line fitted with the relationship  $T=0,0262D^{0,7277}$ . The global goodness of fit is improved over several of the individual data sets, including data sets from Foxford et al., 1998, Childs et al, 2009 (poorly lithified sandstone), van der Zee et al., 2008 (Airport section; Lovde Fault, sets 1 and 2), and Shipton et al., 2006 (sandstone). Large sets covering many orders of magnitude, such as Wibberley et al., 2008 (siliciclastic rocks) and Sperrevik et al., 2002 (sandstone/sandstone- Sinai) exhibit higher goodness of fit regressions than the global goodness of fit.

Among silica based rocks in the published data the relationship between fault core thickness and displacement is  $T=0,0248D^{0,749}$ , with a goodness of fit regression of 76,4%(red trend line in Figure 4-7A). Figure 4-7A displays the crystalline data with brown squares (gold trend line), with a thickness to displacement relationship of  $T=0,0165D^{0,715}$ , and a goodness of fit regression of 81,9%. Fault data measured in siliciclastic rock is displayed with blue diamonds (black trend line) exhibit a power law relationship of  $T=0,0267D^{0,753}$ , with a goodness of fit regression of 77,3%. No trend was made for faults in carbonate rock, since there was only one set in the published data. The trend was not displayed in Figure 4-7 because the set was already published, and one set does not display a global



### Thickness/ displacement for previously published data

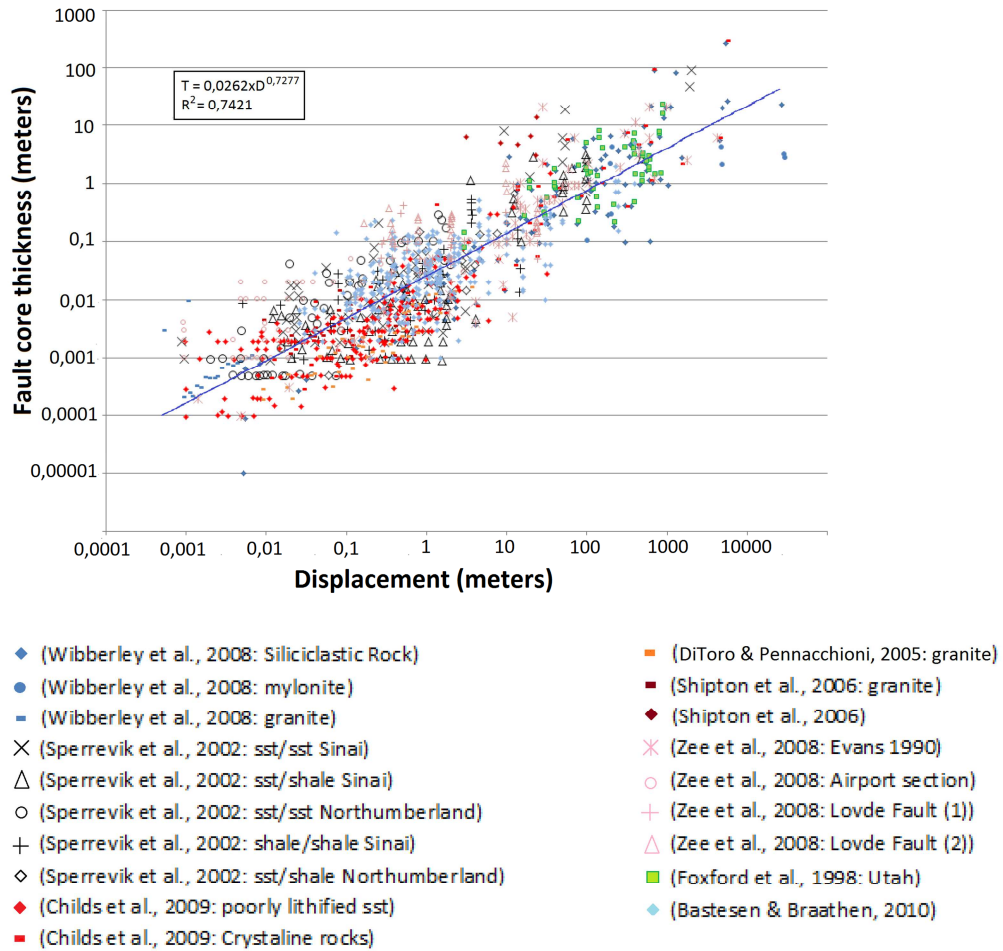


**Figure 4-6:** Plot of fault core thickness to fault displacement for selected previously published articles. A good correlation appears in a log-log plot,

trend. All of the faults in carbonates were recorded by the same authors from the same region, providing no diversity from which a truly global data set could benefit.

Data for ANP and Tidwell draw were compared with the published data used in this report (Figure 4-7B). Although the results from these areas showed a weak correlation between fault core thickness and throw (displacement), the results fit within the confines of the plotted data. The exponent and the goodness of fit regression for all faults in silica based rocks changes very little with the addition of these two data sets, suggesting that, given a larger data set covering a larger range of magnitudes, the correlation between fault core thickness and throw (displacement) for ANP and Tidwell draw might improve, and that the statistical analysis performed thus far in this study might not reflect the true nature of the relationship between fault core thickness and throw at ANP.

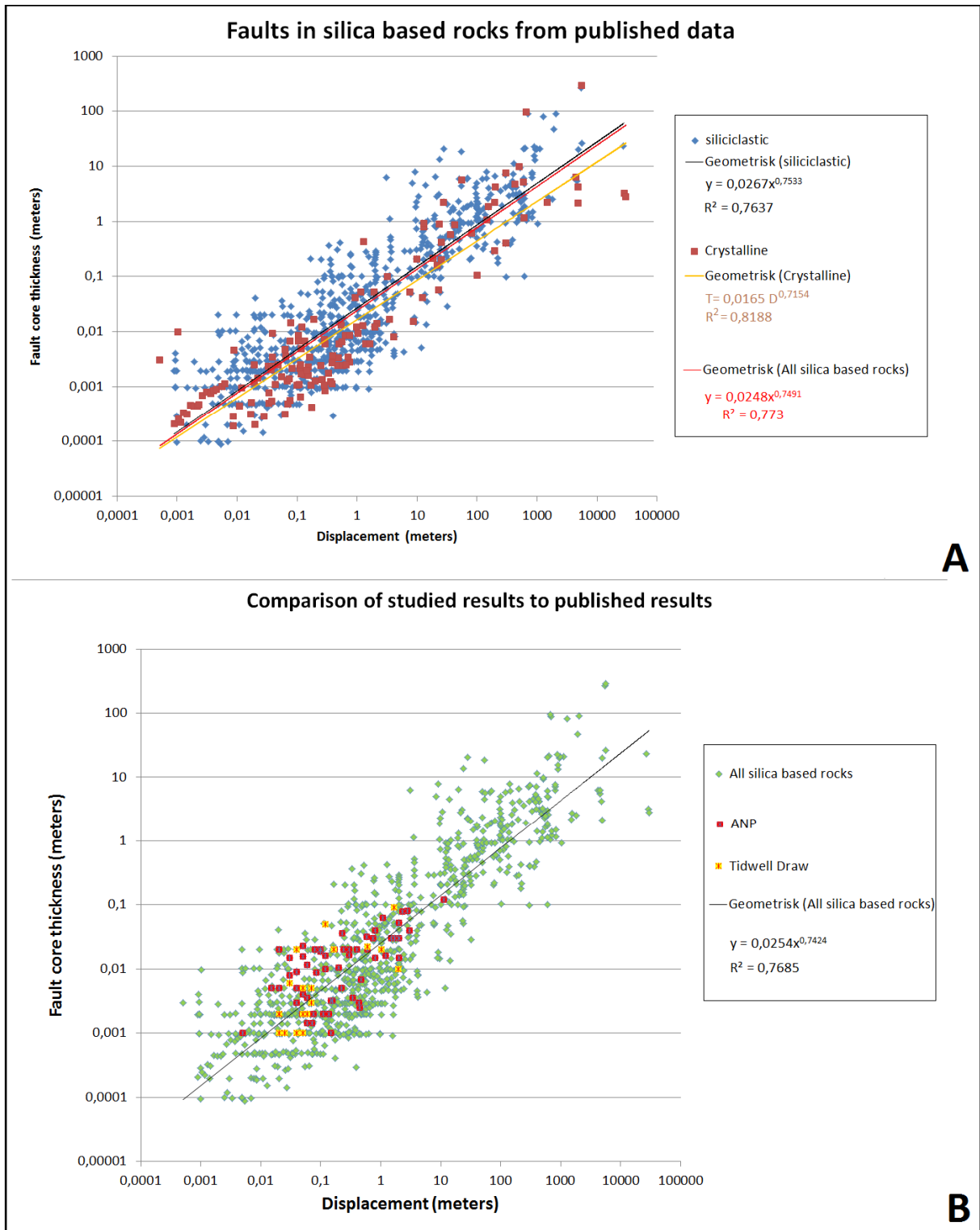


**Figure 4-7:** A) Comparison of faults in siliciclastic rocks and faults in crystalline rocks show that they have a similar scaling relationship between fault core thickness and fault displacement. The trend suggests a consistent power law relationship between the two attributes. B) When ANP data and Tidwell Draw data are inserted into the published data base for faults in siliciclastic and crystalline rock, the slope and regression each are reduced by approximately 1 percent. The data from ANP and Tidwell draw fit within the global data base, despite having weak power law correlation between fault core thickness and throw.

### 4.2.3 Comparison of ANP results with Foxford et al., 1998

In this study it was found one other report of the relationship between fault thickness and displacement using data from the Moab Fault. Foxford et al., 1998 measured the fault in several locations including at ANP, observing the relationships between thickness and displacement of major slip surfaces within the Moab Fault. In contrast to the research done on large fault data at Moab Fault by Foxford et al., 1998, the research done in this project has been focused on small faults (displacement less than 12 meters). Therefore, there is very little overlap between the measurements of Foxford et al., 1998, and the work done here (Figure 4-8A)

The observations made by Foxford et al., 1998 resulted in measurements that could best be described as a power law trend of  $T=0,0806D^{0,5812}$ , with a goodness of fit  $R^2$  of 45,5% (Figure 4-8B). When combining the ANP data with Foxford et al., 1998 data, a power law relationship (represented by the straight line in the graph, and by the equation  $y=0,0359x^{0,7149}$ ) becomes apparent.

Some factors should be considered when reviewing these results. An apparent paucity of data shows up between the data at ANP and the data recorded by Foxford et al., 1998. Figure 4-8C shows 3 fault readings between 3 meters and 16 meters of displacement. This is in fact not a larger gap in displacement than the average gap between Foxford et al., 1998 displacement readings. If the 900 meter span in their displacement readings is divided by 53 displacement measurements taken by them, then the average distance between displacement readings is 17,3 meters, greater than the gap shown in the graph. In the same manner that scatter is hidden by the logarithmic scale as one moves up the scale, moving down the scale can exaggerate a given linear dimension. Whereas 17m might

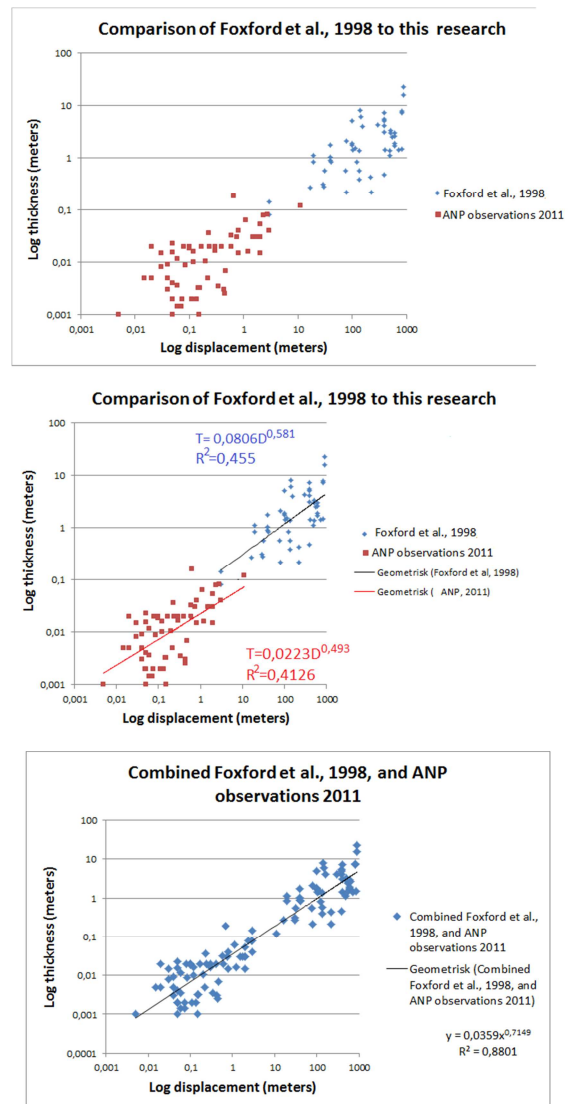


**Figure 4-8:** plots showing throw to displacement for faults from Foxford et al., 1998 (blue diamonds) and the observations from ANP that have been described in this paper (brown squares). A) The data is shown without trend lines for a visual comparison. Note that faults from Foxford et al., 1998 do not overlap with the ANP observations from 2011 with regard to thickness, and tend to have larger displacements than the faults from ANP. B) Power law trend lines for each set of data (straight lines), and the linear trend line for fault readings from ANP. C) When the two data sets are combined, a power law relationship (represented by the straight line in the graph, and by the equation  $y=0,0359x^{0,7149}$ ) becomes apparent. Note that all axes are logarithmic.

barely be seen on a log plot between 900 and 1000m, the distance will fill an entire order of magnitude between 1 and 20 m of the log scale. This is what occurs in Figure 4-8C.

Another consideration is the data for the smaller faults represent one location along the Moab Fault and do not necessarily represent small faults in other outcrops along the 45km length of the fault. More Ideally, the readings from the small faults should have been spread over the entire length of the Moab Fault. This would reduce biases that may have occurred due to one or another factor that might have affected only the southern-most section of the fault. In geological research, however, outcrops and measurements must be taken where they can be found (Davis, 2002). Expenses and availability dictate the data that is gathered.

The thickness of the faults at ANP show a weak correlation to displacement following a power law trend (Figure 4-8B). Although both data sets show a weak correlation in log-log scale, when the faults from Foxford et al., 1998 research are plotted with the faults from ANP, the log thickness to log displacement plot shows data ranging over six orders of displacement with scatter that covers two orders of thickness (Figure 4-8C). The relationship of the faults observed in the combined plot shows a power law trend of  $T=0,0359D^{0,715}$  with a goodness of fit ratio of 88,0%. The exponent in the plot of the combined data with Foxford et al., 1998 compares well with the expected result published in Kolyukhin & Torabi, 2012. In Table 5 of their article, it was suggested that a change-point for the thickness- displacement relationship occurs in faults at approximately 0,09m displacement. For faults with displacements greater than 0,09m the power law exponent should be  $0,78\pm 0,03$  (Kolyukhin & Torabi, 2011). The exponent found for the combined plot with Foxford et al., (1998) (Figure 4-8C) is 0,71 and includes faults with displacements less than 0,09m.

The reason for the higher goodness of fit  $R^2$  for Moab fault, when compared with the global plot of fault core thickness is likely that stratigraphy and tectonic setting is consistent along the Moab Fault, allowing for common attributes through the fault. The values have similar ratios, variances and covariances which would allow the correlation, and therefore the goodness of fit  $R^2$  to remain high. In contrast, global data shares data from different systems with different regression slopes. This could spread the variance of the global data set and reduce the correlation, which in turn can lower the regression.

### 4.3 Implications for fault architecture

In recent literature regarding faults in reservoir modeling, faults are increasingly viewed not as two dimensional planes, but as three dimensional structures (Faerseth et al., 2007; Fredman et al., 2007; Braathen et al., 2009; Wibberley et al., 2008). New methods to incorporate faults into models for simulation, research into flow properties and permeability of fault structures emphasize the need to understand fault architecture. Fault gouge and clay smear in faults tend to reduce cross fault

permeability (Wibberley et al., 2008; Faerseth et al., 2007). It is necessary to be able to estimate the width of the fault in order to run a fluid flow simulation of a model (Sperrevik et al., 2002).

The thickness of a fault may vary by a factor of 12 laterally in a run less than half of the displacement (Foxford et al., 1998). With this in mind, and understanding the power law relationship shown in this report, it should be possible to develop a method to predict a minimum and a maximum thickness of a fault for a given displacement. In finding the minimum thickness, it may then be possible to predict leak off pressure for a reservoir and calculate the capacity of CO<sub>2</sub> that can be injected into the reservoir. Using the findings in this report as a basis, it may be possible to develop an experiment to test and refine these concepts.

Observations reported by Childs et al., 2009 indicate that faults in poorly lithified sedimentary rock and those in crystalline rock exhibited similar thickness/ displacement ratios. However, In Figure 4.7, the trend line for crystalline rocks is slightly less steep in this study than the trend for siliciclastic rocks, suggesting that for a given displacement, faults affecting crystalline rocks may have slightly less thickness readings than for faults in siliciclastic rocks. The lower thickness values for a given displacement exhibited by crystalline rocks may reflect the fact that crystalline rocks are more durable and wear resistant than siliciclastic rocks. Crystalline rocks are made up of crystals which are fused together and interlocking. Siliciclastic rocks are porous and made up of loose grains which are cemented together. The friction and grinding action of two blocks against one another may cause sedimentary rocks to wear quicker than for the same stresses against more durable crystalline rock, leading to thicker fault cores for sedimentary rocks than for crystalline rocks, for a given amount of displacement, with all other variables being equal..



# 5 Conclusion and further research

---

## 5.1 Conclusion

Fifty-four measurements of fault core thickness and fault throw were taken of minor faults along a scanline from the Moab Fault at Arches National Park, Utah, USA. Eight additional faults were measured from photographs of this locality. Displacement and fault core thickness from twenty-one faults in Tidwell Draw in San Rafael Swell, Utah were measured. These measurements were statistically analyzed for frequency distribution, and for correlation between fault core thickness and displacement. The results were then compared with data from previously published articles.

Photographic estimations of fault throw and thicknesses, when following the procedures outlined in this paper, have produced satisfactory results. Data from the ANP scan line have been augmented with eight faults estimated from photographs. Statistical results of the data augmented with photo estimates are comparable to the statistical results from data that comes from the scan line only.

1. EF plots of displacement at ANP exhibited a trend interpreted as power law for frequency distribution of fault throw values. For thicknesses, the distribution is interpreted as a log-normal distribution formed from a change in the power law exponent that occurs at approximately 0,015m of fault core thickness.
2. The plot of thickness to throw for ANP data displays inconclusive poor results when analyzed alone. When the ANP data set is augmented with more data from Moab Fault, from Foxford et al., 1998, the result of the combined plot shows a power law trend of  $T=0,0359D^{0,715}$  with a goodness of fit  $R^2$  of 88,0%
3. The EF plots for the throw data from Tidwell Draw exhibit a trend that is best described with a power law frequency distribution model. The fault core thickness data when taken whole, is best described by a log-normal frequency distribution model.

The plot comparing fault core thickness to fault throw for Tidwell Draw shows a low correlation for a power law relationship. No comparable data set was found to augment the data at Tidwell Draw.

4. Graphical analysis of published data EF plots have revealed straight trends in Probability scale EF to log scale displacement. These straight trends provide a stronger argument for a log-normal distribution of many of the published data sets than any trends used to support power law trends. Although several arguments for why power law trends stray from a straight line in log EF/ log displacement plots, none of these arguments provide a

satisfactory explanation for random formations of straight trends in the probability scale EF/ log scale displacement plots.

5. Similar observations were found for Probability scale EF/ thickness plots, leading to the conclusion that a power law frequency distribution is not the only type of distribution that exists for fault attributes in nature. Examples can be produced for log-normal distribution. Examples by Sperrevik et al., 2002, and Foxford et al., 1998 were provided to demonstrate how an overall trend of one frequency distribution model can plausibly be made up of smaller trends of another (secondary) type of distribution, with changes in slope demarcating the secondary model's attributes.
6. When a global plot of the published data is produced, a goodness- of- fit regression of 74,2% supports a power law relationship between fault core thickness and fault displacement of  $T=0,262 * D^{0,728}$ . Similar trends are exhibited for faults in crystalline rock, and faults in siliciclastic rock. The data from Tidwell Draw and from ANP integrates successfully with the data for all silica based rocks in the published data set, with a goodness of fit  $R^2$  of 76,9% for a power law relationship of  $T=0,0254 * D^{0,742}$ .

## 5.2 Further research

Research should be conducted to understand the relationship between fault displacement and minimum core thickness. The IMPACT project focuses on the feasibility of potential reservoirs to trap and store injected CO<sub>2</sub>. Although faults may act as barriers to cross-fault fluid flow (Wibberley et al., 2008; Færseth et al., 2007; among others), this barrier is only as impermeable as its thinnest point, where permeability could be expected to be greatest. It has been reported by Shipton et al., 2006, Foxford et al., 1998, and Evans, 1990, among others, that thicknesses of faults have a tendency to vary by a full order of magnitude along a fault plane in the space of approximately half of the displacement of the fault. Therefore, it should be in the interest of reservoir research to understand minimum fault thicknesses and how this scaling dimension correlates with displacement. In such a project, focus should be given to the scatter on the plot of minimum thickness to displacement. If the scatter is reduced, then minimum thickness may be a better indicator of fault scaling relationships.

Research into what influences the type of fault attribute frequency distribution could include: investigating size, lithology, geomorphology, influence of previously imprinted structures, layer competency, or contrasts of these attributes/ ratios of these attributes. Further work could be to investigate the presence of changepoint in the datasets and the possible factors that cause these changes.

Moab fault is just one example of a fault represented with several data sets. An investigation into other faults or regions may be important for verifying or disproving the concepts initially laid down by Evans, 1990 that faults of similar lithology, geological history, or within a given history might be compared.

Lab research using clay or stiff sand should be carried out to find out the effects folding has on the normal faulting and fracture pattern. Would this pattern match the pattern found at San Rafael Swell or other folded foreland regions/ uplifts? Davatzes et al., 2002 and Cello et al., 2000 would provide a starting point for the development of the laboratory exercise.

# References

---

- Ackermann, R.V., Schlische, R.W., Withjack, M.O., 2001. The geometric and statistical evolution of normal fault systems: an experimental study of the effects of mechanical layer thickness on scaling laws. *Journal of Structural Geology*, volume 23, pages 1803- 1819.
- Agosta & Aydin, A., 2006. Architecture and deformation mechanism of a basin-bounding normal fault in Mesozoic platform carbonates, central Italy. *Journal of Structural Geology*, volume 28, pages 1445-1467
- Aydin, A., & Johnson, A., 1983. Analysis of faulting in porous sandstone. *Journal of Structural Geology*; volume 5, pages 19-31.
- Baars, D.L., & Doelling, H.H., 1987. Moab salt-intruded anticline, east central Utah. *Geological Society of America Centennial Field Guide-Rocky Mountain Section*.
- Barbeau, D.L., 2003. A flexural model for the Paradox Basin: Implications for the tectonics of the Ancestral Rocky Mountains. *Basin Research*, Volume 15, pp. 97-115.
- Bastesen, E. & Braathen, A, 2010. Extensional faults in fine grained carbonates- analysis of fault core lithology and thickness- displacement relationships. *Journal of Structural Geology*; volume 32, pages 1609- 1628.
- Bastesen,E., Braathen, A., Skar, T., (in press). Comparison of scaling relationships of extensional fault cores in tight carbonate and porous sandstone reserves.
- Beach, A., Welbon, A.I., Brockbank, P.J., McCallum, J.E., 1999. Reservoir damage around faults: outcrop examples from the Suez rift. *Petroleum Geoscience*, volume 5, pages 109- 116.
- Berg, Silje S. & Skar, Tore, 2005. Controls on damage zone asymmetry of a normal fault zone: outcrop analyses of a segment of the Moab Fault, SE Utah. *Journal of Structural Geology*, volume 27, pages 1803-1822.
- Bonnet, E., Bour, O., Odling, N.E., Davy, P., Main, I., Cowie, P., Berkowitz, B., 2001. Scaling of fracture systems in geological media. *Reviews of Geophysics*, volume 39, number 3, pages347-383.
- Braathen, A., Tveranger, J., Fossen, H., Skar, T., Cardozo, N., Semshaug, S.E., Bastesen, E., Sverdrup, E., 2009, Fault facies and its application to sandstone reservoirs. *AAPG Bulletin* volume 93, number 7, pages 891- 917.
- Bump, Alexander p., and Davis, George H., 2002. Late Cretaceous- early Tertiary Larimide deformation of the northern Colorado Plateau, Utah and Colorado. *Journal of Structural Geology*; volume 25 (2003); pages 421-440.

- Byerlee, J., & Summers, R., 1976. A Note on the Effect of Fault Gouge Thickness on Fault Stability. International Journal of Rock Mechanics and Mining Science, and Geomechanics Abstracts, number 13, pages 35-36.
- Caine, Jonathan Saul, Evans, James P., Forster, Craig B, 1996. Fault zone architecture and permeability structure. *Geology*; Volume 24, nr 11; pages 1025-1028
- Childs, C.C., Manzocchi, T., Walsh, J.J., Bonson, C.J., Nicol, A., Schöpfer, M.P.J., 2009. A geometric model of fault zone and fault rock thickness variations. *Journal of Structural Geology* volume 31 (2009); pp. 117- 127.
- Clark, R.M. & Cox, S.J.D., 1996. A modern regression approach to determining fault displacement-length scaling relationships. *Journal of Structural Geology*, volume 18, pages 147-152.
- Clark, R.M., Cox, S.D.J., Laslett, G.M., 1999. Generalizations of power-law distributions applicable to sampled fault trace lengths: model choice, parameter estimates and caveats. *Geophysical Journal International*; volume 136, issue 2, pages 357-372.
- Clauset, A., Shalizi, C.R., Newman, M.E.J., 2007. Power Law Distributions in Empirical Data. <http://arxiv.org/abs/0706.1062>. 43 pages.
- Cowie, P. A. & Scholz, C. H., 1992. Physical explanation for the displacement-length relationship of faults using a post-yield fracture mechanics model. *Journal of Structural Geology*; volume 14; No. 10; pages 1133- 1148.
- Davatzes, N.C., & Aydin, A., 2005. Distribution and Nature of Fault architecture of Fault Architecture in Layered Sandstone and Shale Sequence: An Example from the Moab Fault, Utah. In Sorkhabi, R., & Tsuji, Y (Eds) *Faults, Fluid Flow and Petroleum Traps: AAPG Memoir 85*, pages 153-180.
- Davis, G.H., & Reynolds, S.J., 1996. *Structural Geology of Rocks and Regions*, second edition. John Wiley and Sons Inc., New York. 776 pages.
- Di Toro, G., Pennacchioni, G., 2005. Fault plane processes and mesoscopic structure of a strong type seismogenic fault in tonalites (Adamello Batholith, Southern Alps. *Tectonophysics*; volume 402, pages 55-80.
- Doelling, H.H., 1988. Geology of the Salt Valley Anticline and Arches National Park, Grand County, Utah. In Hellmut H. Doelling, Charles G. Oviatt & Peter W Huntoon, *Salt Deformations in the Paradox Region, Utah*. Utah Geological and Mineral Survey Bulletin 122.
- Evans, J.P., 1990; Thickness displacement relationships for fault zones. *Journal of Structural Geology*; volume 12; pages 1061-1067.
- Felletti, F., & Bersezio, R., 2010. Quantification of the degree of confinement of a turbidite filled basin: A statistical approach based on bed thickness distribution. *Marine and Petroleum Geology*; volume 27, pages 515-532.

- Ferrill, D.A., Smart, K.J., Necsoiu, M., 2008. Displacement-length scaling for single event fault ruptures: insights from the Newberry Springs Fault Zone and implications for fault zone structure. Geological Society, London, Special Publications; volume 299, pages 113- 122.
- Foos, Annebelle, 1999. Geology of the Colorado Plateau. Copyright by author; 6 pages
- Fossen, Haakon, 2010. Structural Geology. Cambridge University Press. 463 pages
- Fossen, H., Schultz, R.A., Shipton, Z.K., Mair, K., 2007. Deformation bands in sandstone: a review. Geological Society, London, volume 164, pages 755- 769
- Foxford, K.A., Garden, I.R., Guscott, S.C., Burley, S.D., Lewis, J.J.M., Walsh, J.J., Watterson, J., 1996. The Field Geology of the Moab Fault. in Huffman, A.C. Jr, Lund, W.R., Godwin, L.H. (Eds), Geology and Resources of the Paradox Basin: Utah Geological Association Guide Book 25. Utah Geological Association; pages 265-283.
- Foxford, K.A., Walsh, J.J., Watterson, J., Garden, I.R., Guscott, S.C., Burley, S.D., 1998. Structure and content of the Moab Fault Zone, Utah, USA, and its implications for fault seal prediction. Geological Society, London, Special Publications, volume 147, pages 87-103.
- Fredman, Niclas, Tveranger, Jan, Semshaug, Siv, Braathen, Alvar & Sverdrup, Einar; 2007. Sensitivity of fluid flow to fault core architecture and petrophysical properties of rocks in siliciclastic reservoirs: a synthetic fault model study. Petroleum Geoscience; volume 13; pages 305-320
- Færseth, Roald B., Johnsen, Eivind & Sperrevik, Susanne, 2007. Methodology for risking fault seal capacity: Implications of fault zone architecture. AAPG Bulletin; volume 91, number 9; pages 1231-1246
- Gross, M.R., Gutierrez-Alonso, G., Bai, T, Wacker, M.A., Collinsworth, K.B., 1997. Influence of mechanical stratigraphy and mechanics on fault scaling relations. Journal of Structural Geology Volume 19; No 2; pp. 171- 183.
- Johansen, T., & Fossen, H., 2008., Internal geometry of fault damage zones in interbedded siliciclastic sediments. Geological Society, London, Special Publications 2008; volume 299, pages 35-56.
- Johnson, K.J. & Johnson, A.M., 2000. Localization of layer-parallel faults in San Rafael Swell, Utah, and other monoclinial folds. Journal of Structural Geology, volume 22, pages 1455- 1468.
- Knott, . S.D., Beach, A., Brockbank, P.J., Brown, J.L., McCallum, J.E., & Welbon, A., 1996. Spatial and mechanical controls on normal fault populations. Journal of Structural Geology, volume 18, numbers 2/3, pages 359-372.
- Kolyukhin, D., & Torabi, T., 2012. Statistical analysis of the relationships between fault attributes. Journal of Geophysical Research, volume 117, B05406, doi: 10.1029/2011JB008880. 14 pages.



- Kreisa, R.D., & Moiola, R.J., 1986. Sigmoidal tidal bundles and other tide generated sedimentary structures of the Curtis Formation, Utah. *Geological Society of America Bulletin*; volume 97, pages 381- 387.
- Maerten, L., Pollard, D.D., Maerten, F., 2001. Digital Mapping of the three-dimensional structures of the Chimney Rock fault system, central Utah. *Journal of Structural Geology*; Volume 23; pages 585-592.
- Marshak, Stephen, 2005. *Earth: Portrait of a Planet* (2<sup>nd</sup> ed.) W.W. Norton & Co., New York, N.Y. USA. 748 pages
- McQuarrie, Nadine, & Chase, Clement G., 2000. Raising the Colorado Plateau. *Geology*, volume 28, nr 1, pages 91-94.
- Moore, D.S. & McCabe, G.P., 2006. *Introduction To The Practice Of Statistics.*, Fifth Edition. W.H. Freeman and Company, New York, USA. 882 pages
- Nuccio, Vitoi F.; Condon, Steven M., 1996. Burial and Thermal History of the Paradox Basin, Utah and Colorado, and Petroleum Potential of the Middle Pennsylvanian Paradox Formation. *US Geological Survey Bulletin* 2000-O.
- Olig, Susan S., Fenton, Clark H., McCleary, Jeff, & Wong, Ivan G., 1996. The Earthquake Potential of the Moab Fault and its Relation to Salt Tectonics in the Paradox Basin, Utah. In Huffman, A.C. Jr, Lund, W.R., Godwin, L.H. (Eds), *Geology and Resources of the Paradox Basin: Utah Geological Association Guide Book 25*. Utah Geological Association; pages 265-283.
- Oviatt, C.G., 1988. Evidence for Quaternary deformation in the Salt Valley Anticline, Southeastern Utah. *Utah Geological Survey Bulletin*, volume 122, pages 61-76
- Peacock, D.C.P., Knipe, R.J., Sanderson, D.J., 2000. Glossary of normal faults. *Journal of Structural Geology*, volume 22, pages 291- 305
- Pedersen, Joel L.; Mackley, Rob D.; Edleman, James L., 2002. Colorado Plateau uplift and erosion evaluated using GIS. *GSA Today*; August 2002.
- Rawling, G.C., Goodwin, L.B., Wilson, J.L., 2001. Internal architecture, permeability structure, and hydrologic significance of contrasting fault zone types. *Geology*, January 2001, volume 29, number 1, pages 43-46.
- Shipton, Z.K., Evans, J.P., Thompson, L.B., 2005. The Geometry and Thickness of Deformation Band Fault Core and its Influence on Sealing Characteristics of Deformation Band Fault Zones. In R. Sorkhabi & Y. Tsuji, eds., *Faults, Fluid Flow, and Petroleum Traps: AAPG Memoir 85*. Pages 181-195.
- Shipton, Z.K., Sodem, A.M., Kirkpatrick, J.D., Bright, A.M., Lunn, R.J.; 2006. How thick is a fault? Fault displacement-thickness scaling revisited. in Ambercrombie R., McGarr, A., Di Toro, G. &

- Kanamori, H. (Eds) Earthquakes: Radiated Energy and the Physics of Faulting, American Geophysical Union Monograph Series, pages 193-198.
- Sibson, R.H., 1977. Fault rocks and fault mechanisms. Geological Society, London, Special Publication, volume 133, pages 191-213
- Soliva, R. & Schultz, R.A., 2008. Distributed and localized faulting in extensional settings: Insight from the North Ethiopian Rift- Afar transition area. *Tectonics*, volume 27, TC2003
- Solum, John G., Davetzes, Nicholas c., & Lockner, David A., 2010. Fault-related Clay authigenesis along the Moab Fault: Implications for calculations of fault rock composition and mechanical and hydrologic fault properties. *Journal of Structural Geology*, volume 32, pages 1899-1911
- Sorkhabi, R., & Hasegawa, S., 2005. Fault Zone Architecture and Permeability Distribution in the Neogene Clastics of Northern Sarawak (Miri Airport Road Outcrop), Malaysia. In R. Sorkhabi & Y. Tsuji, eds., *Faults, Fluid Flow, and Petroleum Traps: AAPG Memoir 85*. Pages 139- 151.
- Sornette, D., 2007. Probability Distributions in Complex Systems. <http://arxiv.org:0707.2194>. 27 pages
- Sperrevik, S., Gillespie, P.A., Fisher, Q.J., Halverson, T., Knipe, R.J., 2002. Empirical estimation of fault rock properties. In Koestler, A.G., Hunsdale, R. (Eds), *Hydrocarbon Seal Quantification*. NPF Special Publication Volume 11. Elsevier, Amsterdam. Pages 109-125.
- Stokes, William Lee, 1986. *Geology of Utah*. Utah Museum of Natural History, and Utah Geology and Mineral Survey; 280 pages.
- Torabi, A., & Berg, S., 2011. Scaling of fault attributes, a review. *Marine and Petroleum Geology*, volume 28, pages 1444-1460.
- Trudgill, B.D., 2011. Evolution of salt structures in the northern Paradox Basin: Controls on evaporate deposition, salt wall growth and supra-salt- stratigraphic architecture. *Basin Research*, volume 23, pp 208-238.
- Van der Pluijm, Ben A., & Marshak, Stephen, 2004. *Earth Structure* (2<sup>nd</sup> ed.). W.W. Norton and Company, Inc., New York, New York; 656 pages
- Wibberley, Christopher A.J., Yielding, Graham, Di Toro, Giulio, 2008. Recent advances in the understanding of fault zone internal structure: a review. Geological Society, London, Special Publications 2008; volume 299; pages 5-33.
- Witkind, Irving J., 1988. *Geological Map of the Huntington 30'x60' Quadrangle, Carbon, Emery, Grand and Uintah Counties, Utah*. US Geological Survey, Denver, Co., USA.
- Zee, W. van der, Wibberley, C.A.J., Urai, J.L., 2008. The influence of layering and preexisting joints on the development of internal structure in normal fault zones: the Lovde Basin, France. In Wibberley, C.A.J., Kurz, W., Imber, J., Holdsworth, R.E., Colletini, C. (Eds), *The Internal Structure*

of Fault Zones: Implications For Mechanical and Fluid- Flow Properties. The Geological Society, London, Special Publications, Volume 299, pages 57- 74.

## Appendix 1: Readings from the scan line at ANP

Scan line readings at ANP						
Location	Strike	Dip	Displacement	avg	Comments	
0	303	13			Bedding	
210	220	70			Fracture	
270	92	90			Fracture	
450	287	87		0,002	cc = cataclastic band	
600	237	70			Fracture	
630	138	80		0,002	cc	
750	90	55		0,003	Fracture	
760	90	55		0,001	cc	
795	90	55		0,001	cc	
835	74	78			Fracture	
920	150	72			Fracture	
940	135	78			Fracture	
1000	157	70			Fracture	
1065	138	80		0,002	cc	
1100	138	80		0,002	cc	
1130	90	55		0,002	cc	
1180	138	80			Fracture	
1190	138	80			Fracture	
1193	80	62			Fracture	
1200	138	80			Fracture	
1225	80	62			Fracture	
1260	80	62			Fracture	
1730	143	72	0,04	0,1	Fault	
1750	138	80			cc	
2150	116	75	0,6	0,6	Fault	
2240					Fracture	
2340	132	82			Fracture	
2500	288	68			Fracture	
2580	154	85			Fracture	
2600					Fracture	
2650					Fracture	
2760					Fracture	
2880					Fracture	
3030	132	82			Fracture	
3110	120	68			Fracture	
3130	132	82			Fracture	
3240	120	68			Fracture	
???	146	84			Fracture	
3460	126	68			Fracture	
3500	126	68			Fracture	
3580	126	68			Fracture	
3640	126	68			Fracture	
3670	126	68			Fracture	
3700	126	68			Fracture	
3720	176	85			Fracture	
3830	106	84			Fracture	
4000	96	74	2	0,0015	Fault	
4190	189	81			Fracture	
4350	132	86	0,05	0,003	cc	
4370	132	86	0,03	0,003	cc	
4500	122	66	0,05	0,002	Fault	
4510	111	72			cc	
4640	111	72			cc	
4670	168	65			Fracture	
4740	296	76	0,22	0,005	Fault	
4800			0,05	0,004	Fault	
5040	135	82	0,748	0,2015	Fault	
			0,434	0,0925	Fault	
			0,135	0,0005	Fault	
			0,049	0,0005	Fault	
			0,075	0,0005	Fault	
5550	307	66	0,3	0,355	Fault	
5900	?	64	0,05	0,001	Fault	
6020	?	64	0,15	0,001	Fault	
6060	?	78	0,005	0,001	Fault	
6100	30	84			Fracture	
6340	276	48			Fracture	

Table A1-1	Location	Strike	Dip	Displacement	avg	Comments
	6460	283	52	11,2	1,92	Fault
				NEW LITHOLOGY: Blue conglomerate, friable, crossbedding		
	6620	302	65			Fault
	6530	330	42			cc
	6590	104	76	0,05	0,003	Fracture
	6710	270	72	0,34	0,0035	Fault
	6750			NEW LITHOLOGY: Dark silty sandstone (friable)		
	6780	132	80			Fracture
	1860	283	68			Fracture
	6930	137	71			Fracture
	7070	251	88			Fracture
	7120	123	82			Fracture
	7150	120	70	0,03	0,015	Fault
	7150	304	20			
				NEW LITHOLOGY: Conglomerate (again)		
	7230	140	77	1,5	0,05	Fault
	7280	312	82			Fracture
	7890	111	70	0,45	0,0025	Fault
	7340	97	84			Fracture
	7440	168	82			Fracture
	7500	133	54	0,3	0,0165	Fault
	7600	60	13			Fracture
	7700	137	75			Fracture
	7830	127	65	0,04	0,005	Fault
	7880	127	65			Fracture
	7890			0,17	0,085	Fault
	7930	80	82	0,17	0,05	Fault
	8070	119	72	0,03		cc
	8120	119	72	0,03	0,002	cc
	8290	80	82	10	0,0105	Fault
	a			0,085	0,0088	Fault
	b			0,11	0,002	Fault
	c			0,015	0,005	Fault
	8335	278	70			Fracture
	8355	278	70			Fracture
	8385	278	70			Fracture
	8400	140	51	2,8	0,215	Fault
	8470	110	77			Fault
	8415-8500	278	70			Fracture
	8590	100	44	HORIZONTAL		Fault
	8640	100	44	HORIZONTAL		Fault
	8640	100	58	0,04	0,003	Fault
	8820	100	44	0,06	0,0115	Fault
	8850	140	80	0,12	0,04	Fault
	8870	140	80	0,04	0,009	Fault
	8960	140	80	0,8	0,3	Fault
	9040	296	64	HORIZONTAL		Fault
	9130	296	64	HORIZONTAL		Fault
	9200	140	66	1,2	0,016	
	9440	294	76			Fracture
	9470	120	76		0,15	Fault
	10000	118	80		0,0355	
	10600	135	70	8,1	1,35	Fault
	11000	170	36	2	0,015	Fault
	11050	132	80	HORIZONTAL		Fault
	11200	126	90	HORIZONTAL		Fault
	11300	190	68	HORIZONTAL		Fault
	11400	204	66	HORIZONTAL		Fault
	11800	128	78	1,1	0,0625	Fault
				NEW LITHOLOGY: pink and green limestone		
	11900	160	34			Fracture
	11920	106	84			Fracture
	11970					Fracture
	12020					Fracture
	12070	116	90	0,12	0,03	Fault
	12180	183	60			Fracture
	12180	106	70			Fracture
	12210	183	60			Fracture
	12230	183	60			Fracture

Table A1-1	Location	Strike	Dip	Displacement	avg	Comments
	12230	122	84			Fracture
	12280	122	84			Fracture
	12315	174	58			Fracture
	12350	122	80			Fracture
	12360	122	80			Fracture
	12370	122	80			Fracture
	12385	122	80			Fracture
	12435	174	58			Fracture
	12440	174	58			Fracture
	12450	174	58			Fracture
	12560	122	80			Fracture
	12580	122	80			Fracture
	12600	122	80			Fracture
	12640	122	80			Fracture
	12665	122	80			Fracture
	12684	174	58			Fracture
	12715	122	80			Fracture
	12790	122	80			Fracture
	12810	122	80			Fracture
	12860	122	82	1,2	0,2	<b>Fault</b>
	12900	122	83			Fracture
	13000	0	50			Fracture
	13010	344	47			Fracture
	13020	110	73			Fracture
	13070	26	70			Fracture
	13100	123	90			Fracture
	13140	140	90			Fracture
	13180	280	70			Fracture
	13200	290	77			Fracture
	13280	6	50			Fracture
	13285	296	70			Fracture
	13300	310	82			Fracture
	13310	133	78			Fracture
	13380	145	43			Fracture
	13420	112	79			Fracture
	13470	350	50			Fracture
	13490	0	64			Fracture
	13500	116	90			Fracture
	13510	122	78			Fracture
	13515	304	68			Fracture
	13610	0	44			Fracture
	13650	121	80			Fracture
	13700	140	86			Fracture
	13790	126	79			Fracture
	13960	310	60			Fracture
	13910	5	128			Fracture
	13960	128	80	3	0,2	<b>Fault</b>
	14040	305	83	0,1	0,02	<b>Fault</b>
	14040	25	40			Fracture
	14060	305	83	0,1	0,02	<b>Fault</b>
	14120	315	82	0,05	0,023	<b>Fault</b>
	14200	313	82	0,02	0,005	<b>Fault</b>
	14200	323	85	0,03	0,008	<b>Fault</b>
	14240	325	77	0,05	0,0155	<b>Fault</b>
	14300	20	65			Fracture
	14400	102	80			Fracture
	14430	40	85			Fracture
	14470	288	78			Fracture
	14480	298	76			Fracture
	14590	10	34			Fracture
	14610	136	80			Fracture
	14630	316	70			Fracture
	14710	325	50			Fracture
	14760	321	69			Fracture
	14780	314	70			Fracture
	14820	302	76			Fracture
	14840	302	76			Fracture
	14840	306	64	0,08	0,02	<b>Fault</b>
	14880	345	76	0,02	0,02	<b>Fault</b>



Table A1-1	Location	Strike	Dip	Displacement	avg	Comments	
	14920	188	42			Fracture	
	14945	188	42			Fracture	
	14950	132	88			Fracture	
	14980	188	42			Fracture	
	15045	188	42			Fracture	
	15070	188	42	0,01	0,0185	<b>Fault</b>	
	15080			1,73	0,03	<b>Fault</b>	
	15130	180	59	2	0,03	<b>Fault</b>	
	15300	320	80			Fracture	
	15400	117	75			Fracture	
	15530	120	78			Fracture	
	15580	136	78			Fracture	
	15670	136	80			Fracture	
	15780	146	76			Fracture	
	15810	140	80			Fracture	
	15920	130	81			Fracture	
	16030	101	82			Fracture	
	16090	154	70			Fracture	
	16500	82	62		4,6	<b>Fault</b>	
	17250	NEW LITHOLOGY: red friable shale					
	17690	293	80			Fracture	
	18070	NEW LITHOLOGY: pink and green limestone					
	19900	306	44	2	0,03	<b>Fault</b>	

**Appendix 2:** Readings from scan lines at Tidwell Draw. Gray indicates incomplete and unused information

Scanline readings at Tidwell Draw						
Location	Strike	Dip	Displacement	T-avg	Comments	
Shale (base of outcrop)						
0	306	14			bedding strike and dip	
80	268	54			fracture	
220	270	76			fracture	
450	30	64	1,02	0,02	Fault.	
					fracture	
500	288	63			fracture	
590	30	64	0,06	0,002	fault	
590	30	64	0,05	0,002	fault	
700	294	85			fracture	
860	281	68			fracture	
930	104	82			fracture	
1000	211	70			fracture	
1300	288	72			fracture	
1850	29	85	0,6	0,022	fault	
1900	16	63			fracture	
1950	342	80			fracture	
1990	70	86			fracture	
2060	354	76			fracture	
2240	229	88			fracture	
2270	42	60			fracture	
2450	304	68			fracture	
3200	136	76	0,165	0,02	fault	
3300	122	62			fracture	
3370	158	89			fracture	
3810	63	60	0,12	0,05	fault.	
3970	136	78			fracture	
4000	126	75			fracture	
4000	285	74			Fracture	
4050	315	72			fracture	
4110	52	86			fracture	
4430	60	50	0,57	scree	fault	
Sandstone layer						
200	330	18			fault	
					Bedding	
270	66	70			fracture	
310	66	70			fracture	
370	122	58	0,04	0,02	fault	
370	122	58	0,04	0,001	fault	
375	127	88			fracture	
383	127	88			fracture	
388	122	88			fracture	
395	122	58	0,05	0,001	fault	
395	122	58	0,05	0,005	fault	
410	127	65			fracture	
417	65	78			fracture	
490	66	70			fracture	
520	57	71			fracture	
700	123	90			fracture	
700	37	48			fracture	
720	63	60			fracture	
760	45	82			fracture	
790	63	77			fracture	
800	116	70			fracture	
840	160	84			fracture	
880	141	70			fracture	
940	341	88			fracture	
1070	128	84	0,025	0,001	fault	
1100	106	64			fracture	
1115	102	52			fracture	
1129	102	52			fracture	
1138	102	52			fracture	
1143	102	52			fracture	
1160	156	68	0,07	0,003	fault	
1160	156	68	0,07	0,005	fault	
1180	117	65	0,02	0,002	fault	
1180	117	65		scree	fault	

Table A1-2	Location	Strike	Dip	Displacement	T-avg	Comments
	1240	84	60	0,02	0,002	fault
	1300	90	45			fracture
	1340	96	60			fracture
	1355	120	55			fracture
	1360	120	55			fracture
	1365	120	55			fracture
	1370	120	55			fracture
	1375	120	55			fracture
	1380	120	55			fracture
	1385	120	55			fracture
	1390	120	55			fracture
	1400	302	62			fracture
	1410	123	44	1,66	0,09	Fault
	1720	38	84			fracture
	1850	122	68			fracture
	1930	125	68			fracture
	1940	125	68			fracture
	1990	66	72			fracture
	2140	66	68			fracture
	2180	66	68			fracture
	2170	102	70			fracture
	2195	96	72			fracture
	2230	123	68			fracture
	2245	109	54			fracture
	2390	123	72			fracture
	2380	26	76			fracture
	2500	91	72			fracture
	2520	51	80			fracture
	2560	118	70			fracture
	2610	50	74			fracture
	2700	50	64	1,7	scree	fault
	2950	53	56	1,66	0,09	fault
	3000	47	60	1,66	0,09	fault
	3030	35	84			fracture
	3365	63	80			fracture
	3600	300	62			fracture
	3600	120	64			fracture
	4100	44	84			fracture
	4130	40	80			fracture
	4200	73	72			fracture
	4350	76	72			fracture
	4380	268	89			fracture
	4440	61	67			fracture
	4830	310	64			fracture
	4880	110	50			fracture
	1950	83	62			fracture
	5050	270	51			fracture
	5100	90	36	1,95	0,01	fault
	5100	90	36	1,95	0,04	fault

**Appendix 3:** Fault data from the Moab Fault scan line at ANP. Columns 1 and 2 show the displacement, D, and respective average thickness, T, values in meters (m) for the faults as they occurred on the scan line. This fault data is compiled from Appendix 1. Column 3 displays the displacement values sorted from smallest to largest. Column 4 displays the rank ( $n_i$ ), in order from the least displacement to the greatest displacement. Column 5 displays the fraction of displacement values greater than the displacement value of  $n_i$ . Columns 6, 7 and 8 repeat columns 3, 4 and 5 for thickness data. Data herein was used for exceedence frequency (EF) plots (figure 2-3 and figure 2-4).

D(m)	T(m)	D(sorted)	n(i)	EF(D)	T(sorted)	n(i)	EF(T)
0,4	0,02	0,005	1	0,981132	0,001	2	0,962264
0,6	0,02	0,015	2	0,962264	0,001	2	0,962264
2	0,0525	0,02	3,5	0,933962	0,001	2	0,962264
0,05	0,002	0,02	3,5	0,933962	0,002	6	0,886792
0,22	0,005	0,03	5,5	0,896226	0,002	6	0,886792
0,05	0,004	0,03	5,5	0,896226	0,002	6	0,886792
0,748	0,03	0,04	8	0,849057	0,002	6	0,886792
0,434	0,003	0,04	8	0,849057	0,002	6	0,886792
0,135	0,002	0,04	8	0,849057	0,0025	9	0,830189
0,049	0,002	0,049	10	0,811321	0,003	10,5	0,801887
0,075	0,002	0,05	13	0,754717	0,003	10,5	0,801887
0,3	0,02	0,05	13	0,754717	0,0035	12	0,773585
0,05	0,001	0,05	13	0,754717	0,00355	13	0,754717
0,15	0,001	0,05	13	0,754717	0,004	14	0,735849
0,005	0,001	0,05	13	0,754717	0,005	16,5	0,688679
11,2	0,12	0,06	16,5	0,688679	0,005	16,5	0,688679
0,34	0,0035	0,06	16,5	0,688679	0,005	16,5	0,688679
0,03	0,015	0,075	18	0,660377	0,005	16,5	0,688679
1,5	0,03	0,08	19	0,641509	0,008	19	0,641509
0,45	0,0025	0,085	20	0,622642	0,0088	20	0,622642
0,3	0,0165	0,1	22	0,584906	0,009	21	0,603774
0,04	0,005	0,1	22	0,584906	0,01	22	0,584906
0,24	0,02	0,1	22	0,584906	0,0105	23	0,566038
0,17	0,02	0,11	24	0,54717	0,0115	24	0,54717
0,2	0,0105	0,12	25,5	0,518868	0,015	26	0,509434
0,085	0,0088	0,12	25,5	0,518868	0,015	26	0,509434
0,11	0,002	0,135	27	0,490566	0,015	26	0,509434
0,015	0,005	0,15	28	0,471698	0,0155	28	0,471698
2,8	0,08	0,17	29	0,45283	0,016	29,5	0,443396
0,04	0,003	0,2	30	0,433962	0,016	29,5	0,443396
0,06	0,0115	0,22	31	0,415094	0,0165	31	0,415094
0,12	0,016	0,24	32	0,396226	0,0185	32	0,396226
0,04	0,009	0,3	33,5	0,367925	0,02	37	0,301887
0,8	0,015	0,3	33,5	0,367925	0,02	37	0,301887
1,2	0,016	0,34	35	0,339623	0,02	37	0,301887
0,06	0,00355	0,4	36	0,320755	0,02	37	0,301887
2	0,015	0,434	37	0,301887	0,02	37	0,301887
1,1	0,0625	0,45	38	0,283019	0,02	37	0,301887
0,12	0,01	0,6	39	0,264151	0,02	37	0,301887
0,8	0,04	0,748	40	0,245283	0,02	37	0,301887
3	0,04	0,8	41,5	0,216981	0,02	37	0,301887
0,1	0,02	0,8	41,5	0,216981	0,023	42	0,207547
0,1	0,02	1,1	43	0,188679	0,03	45	0,150943
0,05	0,023	1,2	44	0,169811	0,03	45	0,150943
0,02	0,005	1,5	45	0,150943	0,03	45	0,150943
0,03	0,008	1,73	46	0,132075	0,03	45	0,150943
0,05	0,0155	2	48,5	0,084906	0,03	45	0,150943
0,08	0,02	2	48,5	0,084906	0,04	48,5	0,084906
0,02	0,02	2	48,5	0,084906	0,04	48,5	0,084906
0,1	0,0185	2	48,5	0,084906	0,0525	50	0,056604
1,73	0,03	2,8	51	0,037736	0,0625	51	0,037736
2	0,03	3	52	0,018868	0,08	52	0,018868
2	0,03	11,2	53	0	0,12	53	0,01

**Appendix 4:** Thickness and displacement data from Moab Fault, including photo estimations. Italized data was estimated using photographs. Columns 1 and 2 are thickness and displacement data from respective faults in sequence along the scan line. Columns 3-5 are for throw data sorted from least to greatest throw values (column 3), ranked (column 4) for determining the exceedence frequency (column 5). The process was repeated for thickness and presented in columns 6-8. EF plots from this data are shown in figure 2-5. Data from columns 1 and 2 are plotted in figure 2-6

D(m)	T(m)	D(sorted)	n(i)	EF(D)	T(sorted)	n(i)	EF(T)
0,400	0,020	0,005	1	0,983607	0,001	2	0,967213
0,600	0,020	0,015	2	0,967213	0,001	2	0,967213
2,000	0,053	0,02	3,5	0,942623	0,001	2	0,967213
0,050	0,002	0,02	3,5	0,942623	<b>0,0014388</b>	4,5	0,92623
0,220	0,005	0,03	5,5	0,909836	<b>0,0014388</b>	4,5	0,92623
0,050	0,004	0,03	5,5	0,909836	0,002	8	0,868852
0,748	0,030	0,04	8	0,868852	0,002	8	0,868852
0,434	0,003	0,04	8	0,868852	0,002	8	0,868852
0,135	0,002	0,04	8	0,868852	0,002	8	0,868852
0,049	0,002	0,049	9	0,852459	0,002	8	0,868852
0,075	0,002	0,05	13	0,786885	0,0025	11	0,819672
0,300	0,020	0,05	13	0,786885	0,003	12,5	0,795082
0,050	0,001	0,05	13	0,786885	0,003	12,5	0,795082
0,150	0,001	0,05	13	0,786885	<b>0,003237</b>	14,5	0,762295
0,005	0,001	0,05	13	0,786885	<b>0,003237</b>	14,5	0,762295
11,200	0,120	<b>0,05942</b>	16	0,737705	0,0035	16	0,737705
0,340	0,004	0,06	17,5	0,713115	0,00355	17	0,721311
0,030	0,015	0,06	17,5	0,713115	0,004	18	0,704918
1,500	0,030	<b>0,07263</b>	19	0,688525	0,005	20,5	0,663934
0,450	0,003	0,075	20	0,672131	0,005	20,5	0,663934
0,300	0,017	0,08	21	0,655738	0,005	20,5	0,663934
0,040	0,005	0,085	22	0,639344	0,005	20,5	0,663934
0,240	0,020	0,1	24	0,606557	<b>0,0068345</b>	23	0,622951
0,170	0,020	0,1	24	0,606557	0,008	24	0,606557
0,200	0,011	0,1	24	0,606557	0,0088	25	0,590164
0,085	0,009	0,11	26	0,57377	0,009	26	0,57377
0,110	0,002	0,12	27,5	0,54918	0,01	27	0,557377
0,015	0,005	0,12	27,5	0,54918	0,0105	28	0,540984
2,800	0,080	0,135	29	0,52459	0,0115	29	0,52459
0,040	0,003	<b>0,14653</b>	31	0,491803	0,015	31	0,491803
0,060	0,012	0,15	31	0,491803	0,015	31	0,491803
0,120	0,016	<b>0,15453</b>	31	0,47541	0,015	31	0,491803
0,040	0,009	0,17	33	0,459016	0,0155	33	0,459016
0,800	0,015	0,2	34	0,442623	0,016	34,5	0,434426
1,200	0,016	0,22	35	0,42623	0,016	34,5	0,434426
0,060	0,004	<b>0,23062</b>	36	0,409836	0,0165	36	0,409836
2,000	0,015	0,24	37	0,393443	0,0185	37	0,393443
1,100	0,063	0,3	38,5	0,368852	0,02	42	0,311475
0,120	0,010	0,3	38,5	0,368852	0,02	42	0,311475
0,800	0,040	0,34	40	0,344262	0,02	42	0,311475
3,000	0,040	0,4	41	0,327869	0,02	42	0,311475
0,100	0,020	0,434	42	0,311475	0,02	42	0,311475
0,100	0,020	0,45	43	0,295082	0,02	42	0,311475
0,050	0,023	<b>0,47425</b>	44	0,278689	0,02	42	0,311475
0,020	0,005	<b>0,59055</b>	45	0,262295	0,02	42	0,311475
0,030	0,008	0,6	46	0,245902	0,02	42	0,311475
0,050	0,016	0,748	47	0,229508	0,023	47	0,229508
0,080	0,020	0,8	48,5	0,204918	0,03	50	0,180328
0,020	0,020	0,8	48,5	0,204918	0,03	50	0,180328
0,100	0,019	1,1	50	0,180328	0,03	50	0,180328
1,730	0,030	1,2	51	0,163934	0,03	50	0,180328
2,000	0,030	1,5	52	0,147541	0,03	50	0,180328
2,000	0,030	1,73	53	0,131148	<b>0,03189</b>	53	0,131148
<b>0,155</b>	<b>0,003</b>	2	55,5	0,090164	<b>0,036004</b>	54	0,114754
<b>0,059</b>	<b>0,001</b>	2	55,5	0,090164	0,04	55,5	0,090164
<b>2,317</b>	<b>0,078</b>	2	55,5	0,090164	0,04	55,5	0,090164
<b>0,231</b>	<b>0,036</b>	2	55,5	0,090164	0,0525	57	0,065574
<b>0,073</b>	<b>0,001</b>	<b>2,3169</b>	58	0,04918	0,0625	58	0,04918
<b>0,474</b>	<b>0,007</b>	2,8	59	0,032787	<b>0,077823</b>	59	0,032787
<b>0,147</b>	<b>0,003</b>	3	60	0,016393	0,08	60	0,016393
<b>0,591</b>	<b>0,032</b>	11,2	61	0,001	0,12	61	0,001

**Appendix 5:** Data for displacement and thickness of faults observed at Tidwell Draw. Columns 1 and 2 show the displacement and thickness for each fault in the order that each fault appeared along the scan line. Column 3 shows the displacement data arranged from smallest to largest. Column 4 ranks the values of displacement from smallest to largest, with an average rank for displacements that were equal. Column 5 shows the exceedence frequency value of each displacement value. This data was used to develop the exceedence frequency plots for the San Rafael Swell fault throw and fault core thickness data.

D (scan)	T (scan)	D (sorted)	n(i)	EF (D)	T (sorted)	n(i)	EF (T)
1,02	0,02	0,02	1,5	0,928571	0,001	2	0,904762
0,06	0,002	0,02	1,5	0,928571	0,001	2	0,904762
0,05	0,002	0,025	3	0,857143	0,001	2	0,904762
0,6	0,022	0,04	4,5	0,785714	0,002	4,5	0,785714
0,165	0,02	0,04	4,5	0,785714	0,002	4,5	0,785714
0,12	0,05	0,05	7	0,666667	0,002	4,5	0,785714
0,04	0,02	0,05	7	0,666667	0,002	4,5	0,785714
0,04	0,001	0,05	7	0,666667	0,003	8	0,619048
0,05	0,001	0,06	9	0,571429	0,005	9,5	0,547619
0,05	0,005	0,07	10,5	0,5	0,005	9,5	0,547619
0,025	0,001	0,07	10,5	0,5	0,01	11	0,47619
0,07	0,003	0,12	12	0,428571	0,02	13	0,380952
0,07	0,005	0,165	13	0,380952	0,02	13	0,380952
0,02	0,002	0,6	14	0,333333	0,02	13	0,380952
0,02	0,002	1,02	15	0,285714	0,022	15	0,285714
1,66	0,09	1,66	17,5	0,166667	0,04	16	0,238095
1,66	0,09	1,66	17,5	0,166667	0,05	17	0,190476
1,66	0,09	1,66	17,5	0,166667	0,09	19,5	0,071429
1,66	0,09	1,66	17,5	0,166667	0,09	19,5	0,071429
1,95	0,01	1,95	20,5	0,02381	0,09	19,5	0,071429
1,95	0,04	1,95	20,5	0,02381	0,09	19,5	0,071429



